Biomass Characterization and Reduced Order Modeling of Mixed-Feedstock Gasification

by

Alex J. Chapman

B.S. Mechanical Engineering
University of California, Los Angeles, 2009

SUBMITTED TO THE DEPARTMENT OF MECHANICAL ENGINEERING IN PARTIAL FULFILLMENT OF THE REQUIREMENTS FOR THE DEGREE OF

MASTER OF SCIENCE IN MECHANICAL ENGINEERING
AT THE
MASSACHUSETTS INSTITUTE OF TECHNOLOGY

JUNE 2011

Author: _____
Department of Mechanical Engineering
May 6, 2011

Certified by: _____
Ahmed Ghoniem
Ronald C. Crane (1972) Professor of Mechanical Engineering
Department of Mechanical Engineering
Thesis Supervisor

Accepted by: _____
David E. Hardt
Chairman, Department Committee on Graduate Students
Department of Mechanical Engineering

Page intentionally left blank

Biomass Characterization and Reduced Order Modeling of Co-fed Gasification

by

Alex J. Chapman

Submitted to the Department of Mechanical Engineering
on May 6, 2011 in Partial Fulfillment of the
Requirements for the Degree of Master of Science in
Mechanical Engineering

ABSTRACT

There has been much effort to characterize and model coal for use in combustion and gasification. This work seeks to delineate the differences and similarities between biomass and coal, with emphasis on the state of the art in biomass pyrolysis/devolatilization modeling.

An existing coal Entrained Flow Gasification (EFG) Reduced Order Model (ROM) was expanded to more accurately simulate the gasification of a mixed feedstock of biomass and coal. The GE 2700tpd gasifier was used because it is a widely used technology. The characteristics and state of the art in biomass conversion models were applied in the expanded ROM to model coal-biomass mixture gasification.

Biomass has higher oxygen content and lower fixed carbon content than coal. Therefore, as results show, increasing the mass fraction of wood leads to a rise in temperature and drop in syngas heating value and Cold Gas Efficiency (CGE). The oxygen feed stream must be adjusted downward to maintain a constant temperature. Temperature change has the strongest effect on ash slag (lesser viscosity and thickness) while ash composition has a very small effect (greater viscosity and thickness).

Thesis Supervisor: Ahmed Ghoniem
Title: Ronald C. Crane (1972) Professor of Mechanical Engineering

Page intentionally left blank

ACKNOWLEDGEMENT

I would like to thank my advisor, Professor Ahmed Ghoniem, for all of his insight and guidance, in this work and beyond. It has been an honor and a pleasure to work with my many colleagues in the Reacting Gas Dynamics laboratory; I am indebted to them for their support of my research. Randall Field at the MIT Energy Initiative has been an incredible resource for many technical issues. Finally, I have been blessed with family and friends who have consistently offered encouragement and moral support.

TABLE OF CONTENTS

Table of Figures

Table of Tables

1 INTRODUCTION

In recent decades, there has been increasing interest in low-carbon energy supply. Depending on cultivation practices (Manomet Center for Conservation Sciences 2010), biomass is a carbon-neutral source of energy. When combined with Carbon Capture and Sequestration (CCS), it becomes carbon-negative. Co-feeding biomass to displace a fraction of coal is an enticing option for improving the carbon footprint of gasification. However, biomass is less energy dense on mass basis and more voluminous on mass basis.

Biomass is the oldest source of fuel in human history. However, in the 18th century coal mining increased to feed the industrial revolution and it began displacing wood. Coal was the first to be used in gasification to produce town gas. The scientific study of combustion is fairly new and coal was the first to enjoy the benefits of analytical modeling. Serious modeling of biomass thermo-conversion is much more recent, starting in the late 1970s. In many cases, approaches used in modeling coal have been applied to biomass. Indeed, both are solid fuels that contain free and bound moisture, produce volatiles and char upon thermal degradation, and contain small percentages of mineral matter. However, significant differences exist which can and should be reflected in detailed modeling.

1.1 REDUCED ORDER MODELING AND COAL GASIFICATION

A Reduced Order Model was completed by Rory Monaghan in December 2009. It has the ability to represent several different Entrained Flow Gasifiers (EFG's), with configuration options that include oxygen or air blown, up or down fired, slurry or dry fed, one or two stage, and membrane or refractory lined. It represents syngas cooling with a choice of no cooling, radiant cooling only, quench cooling only, or both radiant and quench cooling. Having this configurability makes the ROM very robust and therefore a good base on which to build further modeling.

The basis for order reduction involves representing the internal flow of a gasifier in a reactor network of Well Stirred Reactor (WSR) and Plug Flow Reactor (PFR) control volumes that track gas and particle flow in an Eulerian manner. The simplest ROM example is the one-stage gasifier. Figure 1-1 below shows how the flow is represented in the reactor network. Below that, Figure 1-2 gives some detail about the processes occurring in each reactor.

The geometric parameters of the model include overall length and diameter, the lengths and diameters of the Internal Recirculation Zone (IRZ), the length and jet angle of the Jet Expansion Zone (JEZ), and the fraction of flow that recirculates through the External Recirculation Zone (ERZ). Other inputs include feed composition (proximate, ultimate, ash) and char kinetics, oxygen/air flow rate and steam flow rate. Outputs include syngas composition and Cold Gas Efficiency (CGE), fractions of emissions like H_2S and NO_2, slag flow rate and thickness, and temperature.

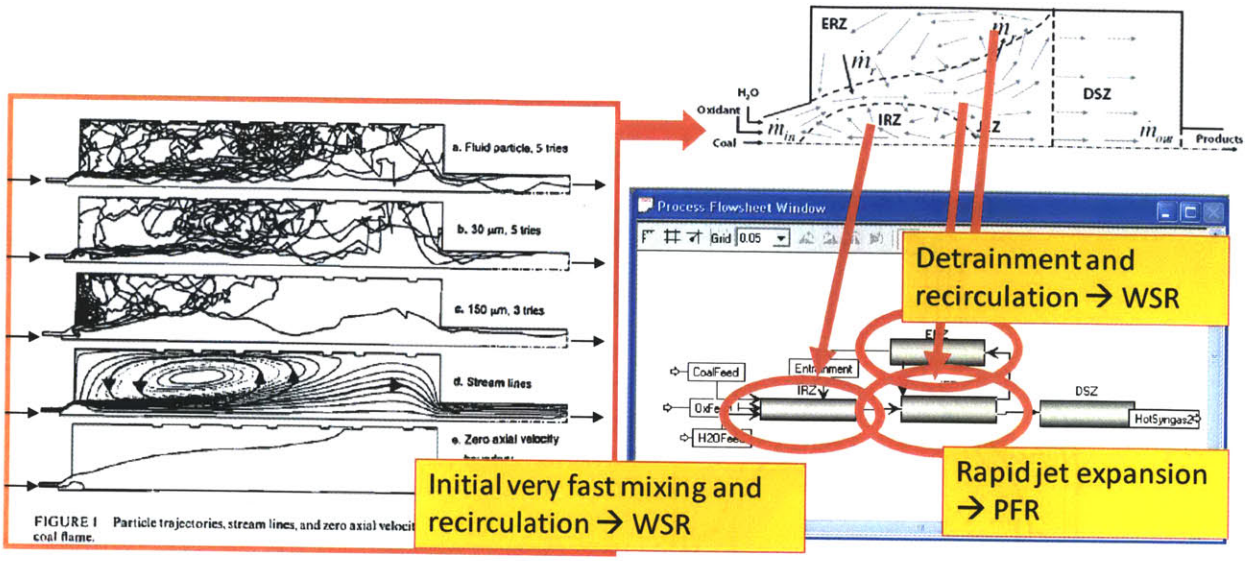

Figure 1-1. Gasifier representation as a Reactor Network. (Monaghan 2010)

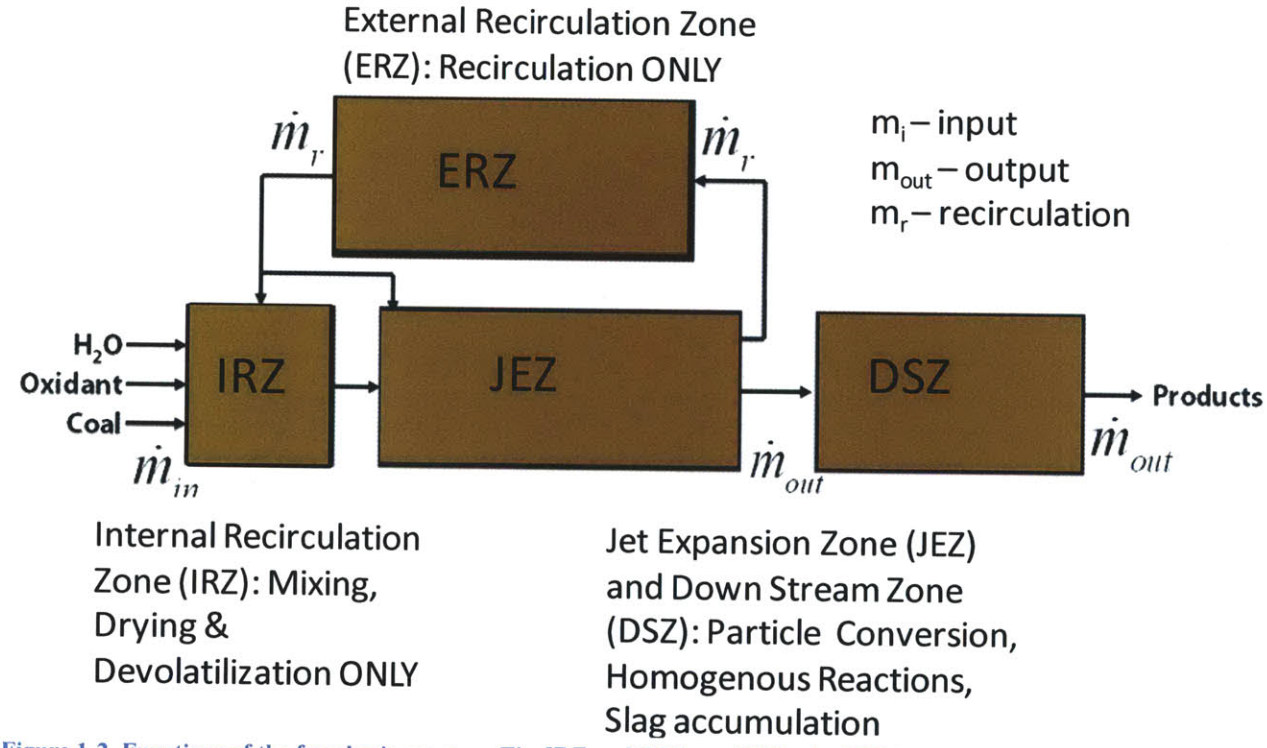

Figure 1-2. Functions of the four basic reactors. The IRZ and ERZ are WSR; the JEZ is a 20 node PFR and the DSZ is a 10 node PFR.

The GE (Texaco) 2700tpd gasifier model was chosen as the basis for the expansion effort because it employs widely-used gasification technology (GE) and is the subject of detailed study by NETL. Further, it was the only commercial scale gasifier simulated by the ROM. The gasifier is down-flow, slurry-fed, oxygen-blown, axially-fired, one-stage, refractory-lined and slagging. It employs radiant syngas cooling followed by quench cooling. A schematic of the GE gasifier is given in Figure 1-3 below.

A list of important conditions and flow are given in Table 1-1. Finally, the reactor network model, characteristics and parameters which the ROM uses to represent the GE 2700tpd gasifier are presented in Figure 1-4.

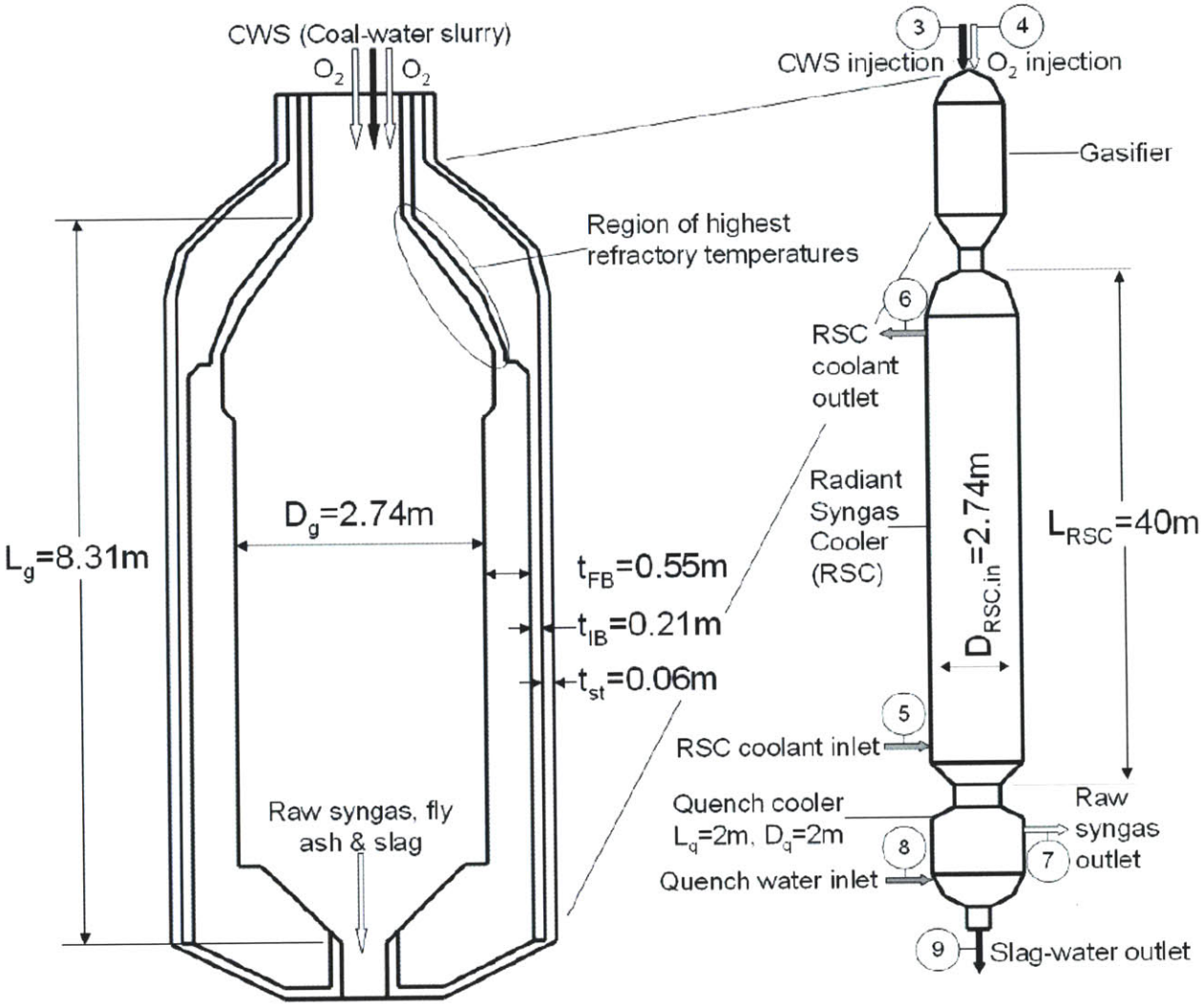

Figure 1-3. GE 2700tpd Gasifier schematic. (Monaghan 2010)

Table 1-1. Flow rates and conditions for GE-2700tpd gasifier and syngas cooler. (Monaghan 2010)

Stream number	Stream name	Solids flow rate (kg/hr)	Liquid & gas flow rate (kg/hr)	Total flow rate (kg/hr)	Temperature (°C)	Pressure (bar)
1	Milled Coal	113586	0	113586	-	-
2	Slurry water	0	46661	46661	-	-
3	Coal-water slurry	113586	46661	160247	608.8	72.3
4	Oxidant	0	95078	95078	96.8	67.5
5	RSC coolant in	0	274301	274301	313.2	137.8
6	RSC coolant out	0	274301	274301	335.9	137.8
7	Quenched gas	0	305065	305065	210.4	55.0
8	Quench water in	0	323059	323059	-	-
9	Slag-water out	12468	260852	273320	-	-

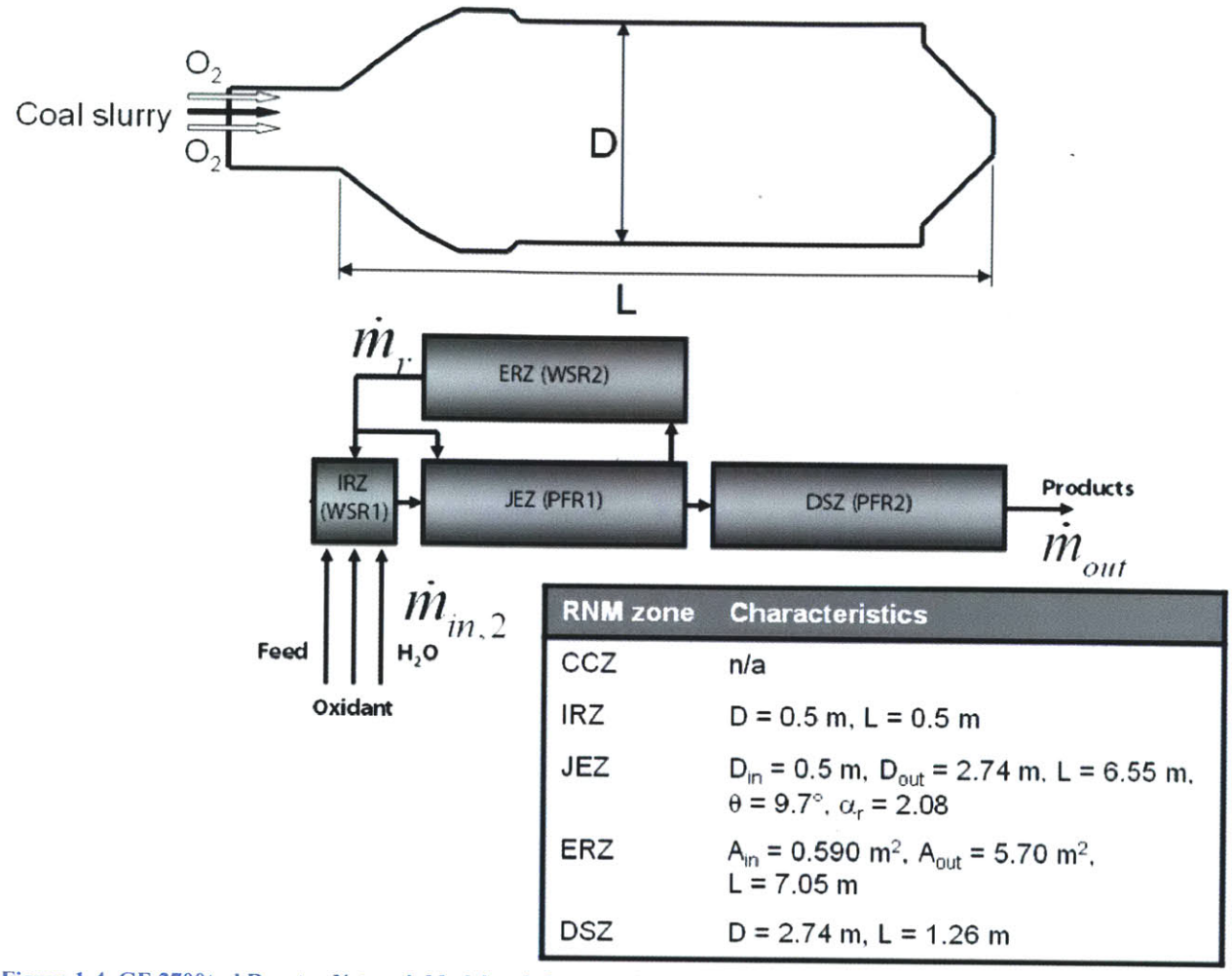

RNM zone	Characteristics
CCZ	n/a
IRZ	D = 0.5 m, L = 0.5 m
JEZ	D_{in} = 0.5 m, D_{out} = 2.74 m, L = 6.55 m, θ = 9.7°, α_r = 2.08
ERZ	A_{in} = 0.590 m^2, A_{out} = 5.70 m^2, L = 7.05 m
DSZ	D = 2.74 m, L = 1.26 m

Figure 1-4. GE 2700tpd Reactor Network Model and characteristics. (Monaghan 2010)

The ROM is built in Aspen Custom Modeler, which is a simultaneous equation solver (Static) with built-in tools like an integrator (for Dynamic mode) and gas property database. The Dynamic mode allows for the analysis of the system response to user-defined input functions, called Tasks. Figure 1-5 below shows the simulation of a cold start, which starts with the combustion of methane in air, then pressurizes, and finally switches to coal-water slurry and oxygen. The Dynamic mode can also be used to study the effects of changing input feedstock properties and, with the expanded ROM, input feedstock ratios.

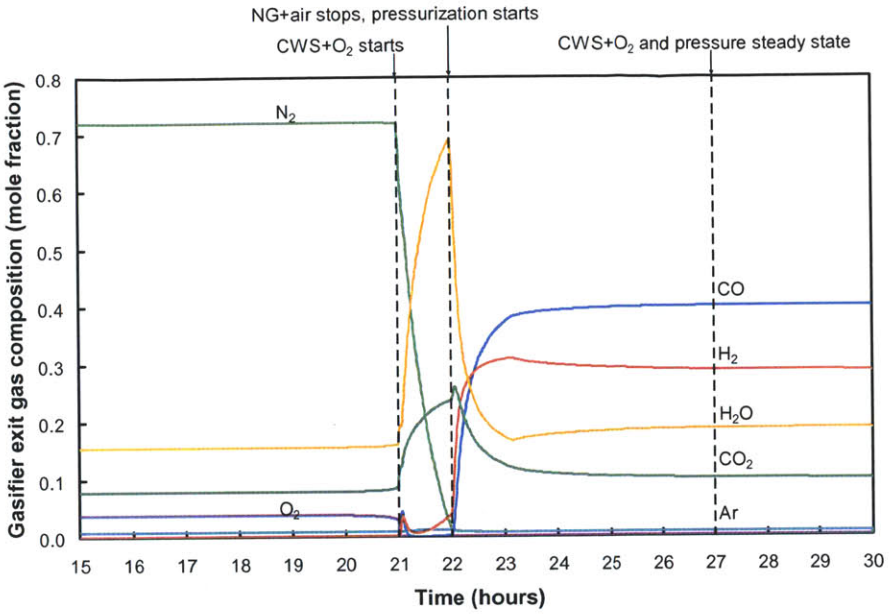

Figure 1-5. Dynamic Mode: Cold start simulation. (Monaghan 2010)

The ROM has been validated with experimental data for the following gasifier designs: 2 tpd Mitsubishi Heavy Industries (MHI) lab-scale gasifier, 0.1 tpd CSIRO lab-scale gasifier, 1 tpd BYU lab-scale gasifier, 1,000 tpd Texaco (GE) pilot-scale gasifier. The ROM results have also been compared to CFD simulations. The MHI experiment/CFD/ROM temperature and syngas validation are presented below in Figure 1-6 and 8 below.

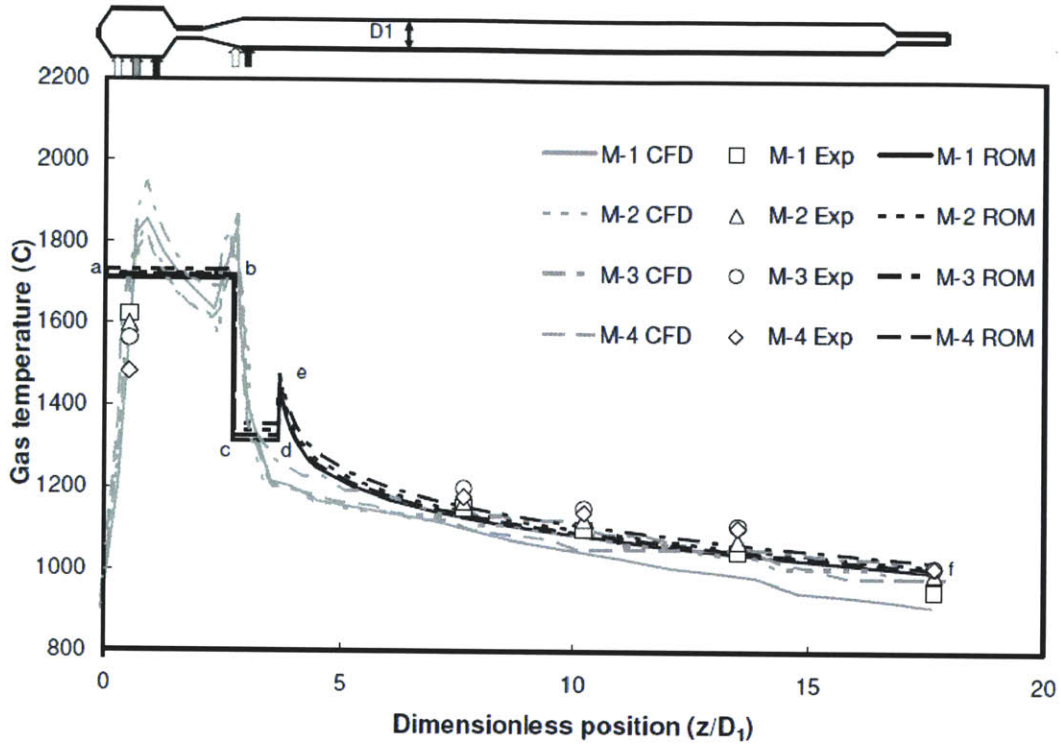

Figure 1-6. Temperature Validation of Coal in MHI Gasifier case with experimental data, CFD and ROM. (Monaghan 2010)

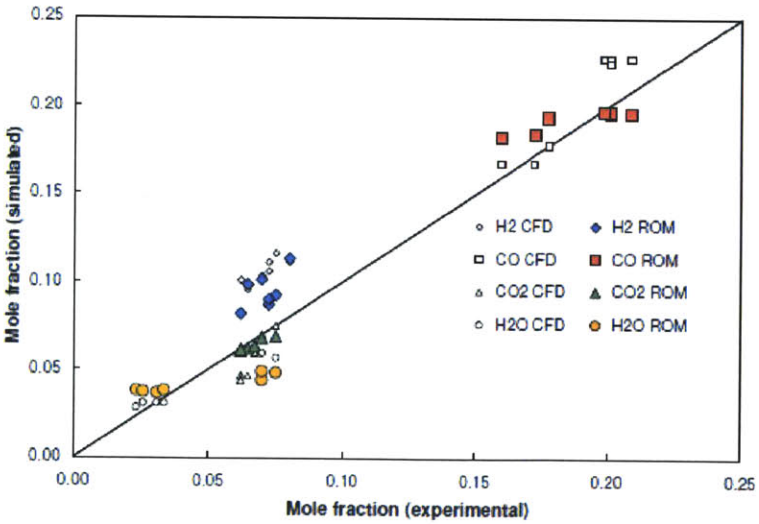

Figure 1-7. Syngas Validation of MHI Gasifier case with experimental data, CFD and ROM. (Monaghan 2010)

1.2 Motivation for Co-Feed Reduced Order Modeling

The differences between biomass and coal are numerous. Because gasification includes many non-linear processes, the output of co-gasification will not be linear. Therefore, a detailed modeling effort of co-gasification should provide non-trivial insight. The ROM for coal provides an excellent basis for this modeling effort, though it must be modified to support multiple feedstocks simultaneously. The

following literature review will characterize biomass and then suggest which biomass characteristics need to be represented and modeled in the ROM. The subsequent section describes the modeling effort and results.

2 LITERATURE REVIEW

2.1 RAW BIOMASS CHARACTERISTICS

Woody and herbaceous biomasses are composed of cellulose, hemicellulose, lignin, extractives and ash. Cellulose makes up the primary cell wall of wood. It is a homopolysaccharide ($C_6H_{10}O_5$) and appears as very long chains, on the order of thousands of monomers long. It composes between 40 and 45% of dry wood. Hemicellulose is a heteropolysacaride with shorter (200 monomers), branched chains. It is weaker than cellulose and composes between 20 and 30% of dry wood. Lignin is a less defined conglomerate of substances which encases and reinforces plant cell walls. It has a greater heating value than cellulose due to its lower oxygenation and composes 25-40% of dry wood (Sjöström 1993). Hemicelluloses, cellulose and lignin decompose in different temperatures ranges to form volatiles and char. Decomposition of hemicellulose (often surrogated by Xylan) occurs at temperatures ranging from 225 to 325 °C; cellulose decomposes between 325 and 375 °C; lignin gradually decomposes between 250 and 500 °C (Fred Shafizadeh & Chin 1977), as seen in Figures 2-1 and 2-2 below (Biagini et al. 2006). Thermogravimetry (TGA) can provide the mass fraction of each component. The polysaccharides provide most of the volatile pyrolysis yields, while char is the main product of lignin (Fred Shafizadeh & Chin 1977).

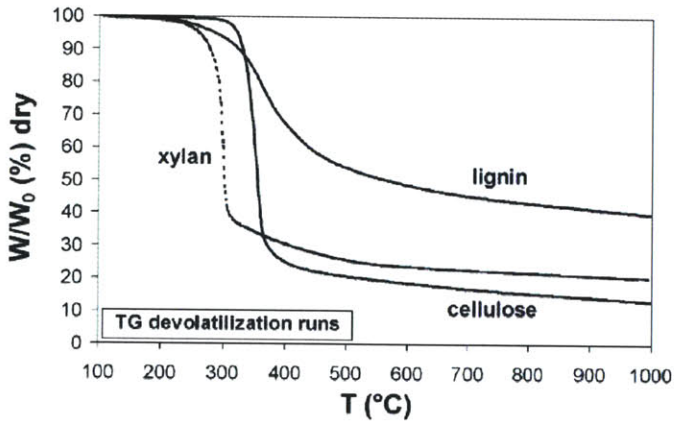

Figure 2-1. TGA weight loss curves for three main components of biomass. (Biagini et al. 2006)

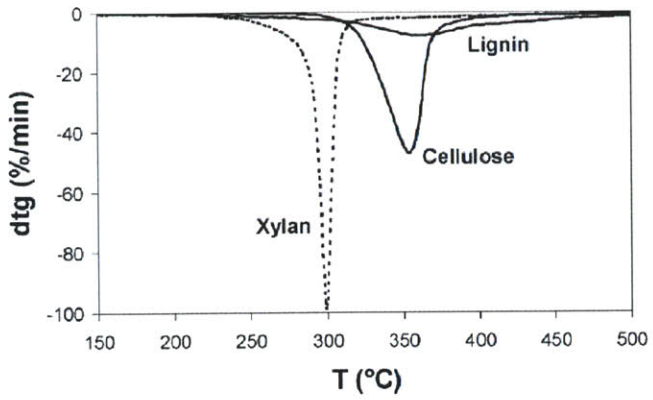

Figure 2-2. TGA weight-loss rate curves for three main components of biomass. (Biagini et al. 2006)

Extractives are oils and other volatiles, which are very unstable and can be removed by pressing or solvent washing or degraded with mild heat. They are often extracted for their high economic value, hence the name "extractive." Ash is defined as inorganic material and usually is comprised of minerals and metal oxides.

The analyses commonly used to describe coal, e.g. proximate, ultimate and ash, can be used to describe biomass using the same standardized tests. However, the volatile matter to fixed carbon ratio is tied to the condition of the test (Ryu et al. 2004) because the pyrolysis volatile yield depends on pyrolysis thermodynamic conditions (Di Blasi 2009) (and many others), which will be discussed later.

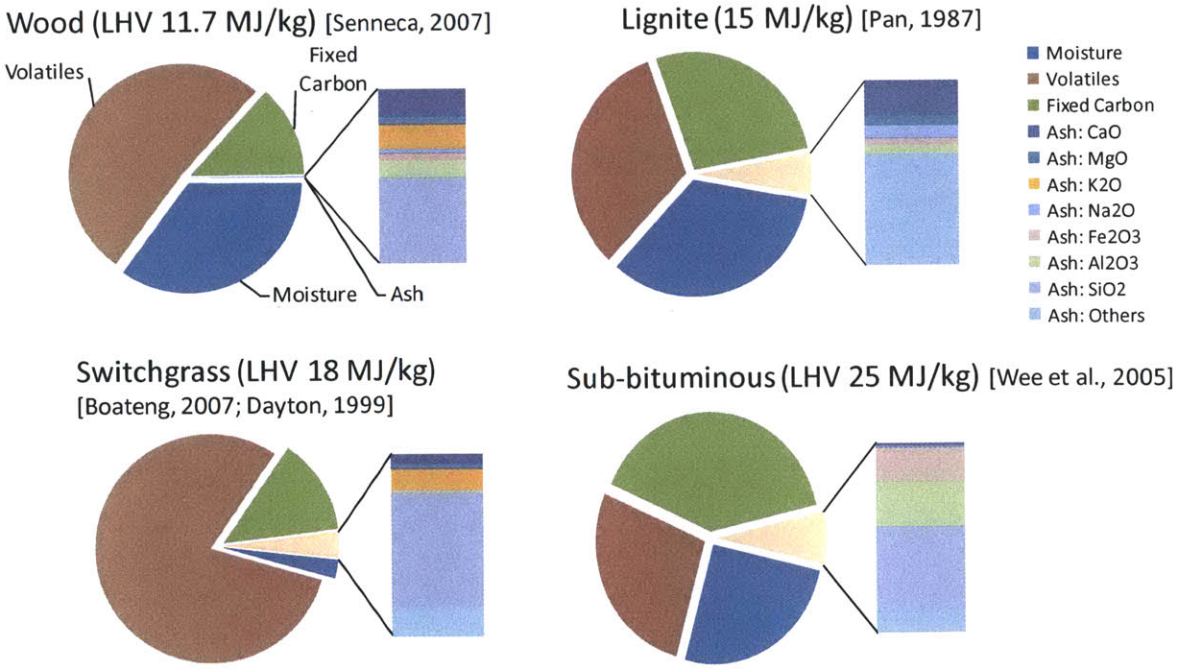

Figure 2-3. Proximate Analyses of Wood, Switchgrass, Lignite and Sub-bituminous coal, As-received basis. (Senneca 2007) (Pan & Serageldin 1987) (Boateng et al. 2007)(Dayton et al. 1999)(Wee et al. 2005)

The side-by-side proximate analyses above (Figure 2-3) show that woody biomass might be thought of as a very low-rank coal with much less ash. In its untreated, green state, it is higher in volatiles and moisture and has a lesser heating value than coal. Switchgrass is similar, though often, as in the sample above, much of the moisture content is field dried, i.e., without forced drying.

Below is a table of analyses with more diverse types of biomass (Higman & van der Burgt 2008, p.76). The variation in energy, moisture and ash content is evident not only among biomass types but even within some of the types, like wood or charcoal.

Table 2-1. Analyses of many biomass types. (Higman & van der Burgt 2008)

Biomass	HHV (MJ/kg)	Moisture (wt%)	Ash (wt%)	Sulfur (wt% dry)	Chlorine (wt% dry)
Charcoal	25-32	1-10	0.5-6		
Wood	10-20	10-60	0.25-1.7	0.01	0.01
Coconut Shell	18-19	8-10	1-4		
Straw	14-16	10	4-5	0.07	0.49
Ground nut shells	17	2-3	10		
Coffee husks	16	10	0.6		
Cotton residues (stalks)	16	10-20	0.1		
Cocoa husks	13-16	7-9	7-14		
Palm oil residues (shells)	15	15	15-20		
Rice husks	13-14	9-15	5-6		
Soya straw	15-16	8-9	12		
Cotton residue (gin trash)	14	9			
Maize (stalk)	13-15	10-20	2(3-7)	0.05	1.48
Palm oil residues (fibers)	11	40			
Sawdust	11	35	2		
Bagasse	8-10	40-60	1-4		
Palm oil residues (fruit stems)		63	5		
Bark				0.07	0.49

The fibrous structure of plant cell gives rise to anisotropic properties. For example, tensile strength is greater and heat conductivity higher in direction of the fibers (Lu et al. 2008). The anisotropic tensile strength causes chipped or ground particles to have a cylindrical shape with length-to-diameter ratios of five on average and which vary between one and ten (Gera et al. 2002). For the purpose of heat transfer, it has been shown (Tye 1969) that for aspect ratios above five, single particles can be approximated as infinitely long cylinders. The cylindrical shape makes grinding raw wood quite energy intensive and practical minimum particle diameters are on the order of hundreds of microns. By breaking

down the polymer chains, mild thermal treatment of wood (torrefaction) has been shown to decrease grinding energy (Svoboda et al. 2009), among other practical improvements, and thus smaller particle sizes may be achieved.

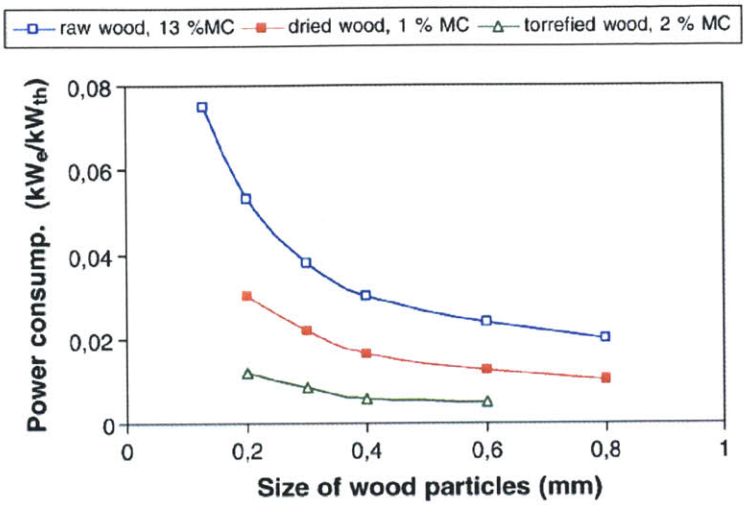

Figure 2-4. Power consumption for grinding of raw, dried and torrefied wood. (Svoboda et al. 2009)

Pulverized coal particles are often modeled as spherical. Coal chars show porosity in the range of 2 to 18% and pore sizes on the nanometer scale. On the other hand, wood chars have porosity values from 40 to 50% and pore sizes between 20 and 30 microns (Di Blasi 2009).

TYPES OF GASIFIERS

There are three main classes of gasifiers. General specifications and advantages are summarized in Table 2-2 below.

Table 2-2. Comparing three main types of gasifiers.

	Fixed	Fluidized	Entrained Flow
Max T (K)	1420	1200	1640-1920
Pressure (atm)	1-27	1-68 (difficult)	1-82
Feed particle size(mm)	5-50	1-5	<0.1
Ash condition	Dry or slagging	Agglomerating	Slagging
Sulfur removal	Downstream	In gasifier	Downstream
General Advantages	Widespread tech	High throughput, low tar	Highest throughput, lowest tar, highest conversion
General Disadvantages	Lowest throughput	Complex recirculation technology, maintenance	Requires high rank fuels, small particles sizes

High temperature is better for maximizing carbon conversion, though more oxygen is required to reach high temperatures. Operating at high pressure is advantageous because pre-reaction compression is less energy intense than post-reaction compression (Higman & van der Burgt 2008). While fluidized beds can be pressurized, this particular combination is not mature technology. Slagging is advantageous for many reasons, including that slag provides thermal insulation for refractory-lined gasifier walls. Fluidized beds allow for in-situ sulfur removal by means of limestone fluidizing material, which removes the need for downstream desulfurization equipment.

2.2 Examples of Co-Feeding Gasifier Plants

There have been a limited number of commercial-scale tests on co-gasification of woody biomass and coal in Entrained Flow gasifiers and a few pilot scale experiments. For example, there were co-feeding tests conducted at the NUON coal IGCC plant in the Netherlands and experiments conducted in the pilot-scale gasifier of Future Energy in Freiberg, Germany (Coda et al. 2007). Commercial, biomass-fed EF gasifiers include Choren (Oxygen blown, 5 bar, 1500 °C) and Kit (Oxygen blown, 80-85 bar, >1400 °C). Both of these incorporate pretreatment of some form; Choren employees a pre-pyrolyzer reactor and Kit feeds bio-oil/bio-char slurry (products of pyrolysis).

There are also examples of pilot scale co-gasification experiments in other types of gasifiers, such as the 2.4tpd MILENA down-draft (fixed) gasifier, used by ECN for co-fed SNG production tests (Vreugdenhil 2009).

2.3 Moisture Vaporizing

Moisture in biomass occurs as free water and bound water. Free water is in liquid form in pores and cells and is defined as the moisture above the fiber saturation point (FSP). Bound water is physically or chemically bound to surface sites or exists as hydrated species and is the moisture present below the FSP. FSP is the weight of water in the sample as a percentage of the weight of an oven-dried sample. The average FSP for wood is 30%. Both forms of moisture are removed by oven-drying. Free moisture vaporizes at a rate determined by the surface saturated vapor pressure. The rate of bound moisture release is better described through a chemical reaction rate (Lu et al. 2008).

2.4 Pyrolysis

Pyrolysis is the thermal decomposition of the main components of biomass: hemicelluloses, cellulose, lignin and extractives. It is often carried out in an inert environment. The yields of this process can be grouped into solids (char), condensable vapors (tar) and permanent gases. Tars are often heavy hydrocarbons and water while gases are mainly light hydrocarbons, carbon monoxide, carbon dioxide, and hydrogen (Di Blasi 2009).

As Koufopanos et al. (1991) point out, the most significant parameters of pyrolysis are temperature, residence times, heating rate, composition and pressure of the surrounding gaseous atmosphere and particle geometry. Temperature exponentially affects the rate of devolatilization, and finite-rate reactions are of course dependent on residence time. Faster heating rate means volatiles escape faster, which means they have less time for secondary reactions with newly formed char and can also change the shape of the char. The surrounding gaseous atmosphere also plays a role in char formation (via pressure) while oxygen content (the composition) accelerates the process. The particle geometry is important for considering heat transfer, which may play a limiting role in pyrolysis.

Organic tars can undergo secondary reactions (polymerization or cracking) with char and gas to produce different yields of the same three lumped groups (Di Blasi 2009). These secondary reactions are sensitive to temperature (Boroson, J. B. Howard, Longwell & Peters 1989b) and pressure (Di Blasi 2009).

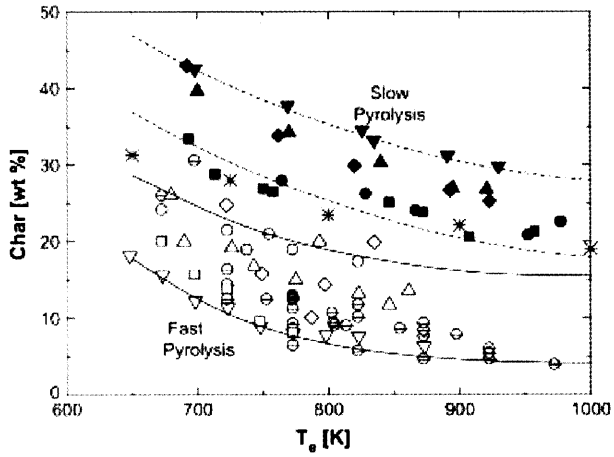

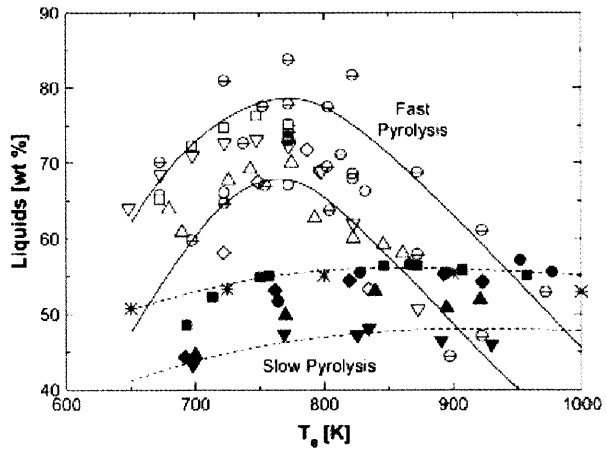

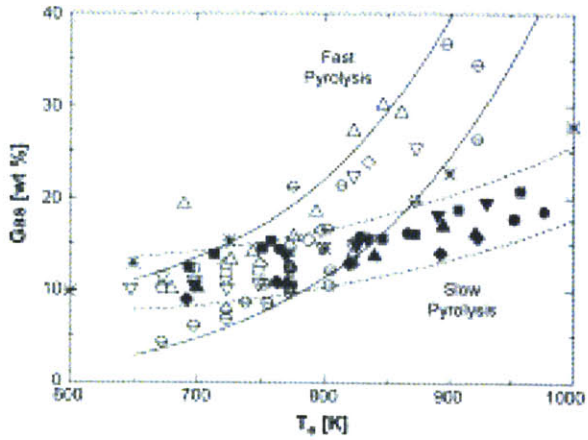

Figure 2-5. Char, Tar and Gas yields of many wood types with varying temperature. (Di Blasi 2009)

The graphs in Figure 2-5 above show an amalgamation of results of many wood pyrolysis TGA studies. Each graph shows one of the three yields varying with pyrolysis temperature. As temperature increases, the yield of char decreases as volatile formation is favored. Tar yield therefore rises as temperature increases until a certain temperature from which point tar cracking into gases becomes very significant.

A noticeable variation in the plotted data is the difference between "Fast Pyrolysis" (open symbols) and "Slow Pyrolysis" (closed symbols). In the case of the char yield, fast pyrolysis (~1000 K/s), which generally implies the pyrolysis of small particles in fluidized beds, experiences higher heat transfer and so is quicker to react to changing temperatures than slow pyrolysis (5-50 K/min), which generally represents large wood chips in fixed-bed reactors, and which requires significant time to reach thermal equilibrium. Therefore, dynamic thermogravimetric yield results seem delayed in temperature. The reason for differences in tar and gas yields between data of fast and slow pyrolysis speeds is the fact that fluidized beds offer free-board space where tars can crack, while fixed beds do not offer this space.

Cracking of woody biomass tar results in the creation of light gases as described above. For example, Boroson et al. (1989b) experimented on cracking primary tars from sweet gum hardwood pyrolysis. This was done by cracking tars, which were formed at 450 °C, in a separate cracking reactor for short residence times (0.9-2.2 s) in the temperature range of 600 to 800 °C. See Table 2-3 below for results. Besides water, they found that carbon monoxide, carbon dioxide and methane were the main yields, and most importantly all the yields varied with cracking temperature.

Table 2-3. Product Yields from Primary Pyrolysis and Different Extents of Homogeneous Secondary Tar Cracking. (Boroson, J. B. Howard, Longwell & Peters 1989b)

	Primary Yields wt.% wood	Yields After Different Extends of Tar Cracking, wt. % wood		
		873 K 1.2 s	973 K 1.0 s	1,073 K 1.0 s
Tar	52.8	36.6	16.6	6.1
Char	18.3	18.1	18.4	17.8
CH_4	0.4	1.7	3.8	5.5
CO	3.2	14.7	25.7	35.7
CO_2	6.8	9.7	11.4	13.2
C_2H_2	0.0	0.1	0.5	0.6
C_2H_4	0.0	1.2	3.6	5.4
C_2H_6	0.0	0.1	0.3	0.4
H_2O	16.3	17.3	17.0	15.2
H_2	0.0	0.1	0.6	1.0
Total	97.8	99.6	97.9	100.9

Tars in the gaseous phase can polymerize when in contact with primary char to produce secondary char, which is of lower reactivity (Di Blasi 2009). One study (Boroson, J. B. Howard, Longwell & Peters 1989a) about the conversion of primary tars induced by contact with char, reports a heterogeneous conversion of about 14 ± 7%. This is also seen in studies on the devolatilization of bio-oil samples subjected to slow heating (5K/min up to 600K) (Branca, Di Blasi, et al. 2005) where char yields are roughly 25-40% of the initial oil mass.

2.5 Pyrolysis Modeling

Pyrolysis yields and rates have been modeled to varying degrees of accuracy and precision. Models in the literature range from single step and semi-global mechanisms to complex chemistry models involving dozens of species. Each has its advantages and limitations.

Depending on particle size, particle heat-up may play an important role in the process, in which case, the following kinetic mechanisms should be couple with heat transfer descriptions.

2.5.1 Single Step Global Models

The simplest way to model pyrolysis is via a one-step reaction (Eq. 1 or 2) with a first-order Arrhenius rate equation (Eq. 3.) The coefficients of the yields must be estimated from experiment data and are either assumed invariant or are discretized and linked with pyrolysis conditions (e.g. temperature).

Eq. 1 $$Solid \xrightarrow{k} a\,Volatiles + b\,Char$$

Eq. 2 $$Solid \xrightarrow{k} a\ Gases + b\ Tars + c\ Char$$

Eq. 3 $$k = Ae^{-E/RT}$$

The rate of mass change of solid usually has a first-order dependence on solid mass as in Eq. 4:

Eq. 4 $$\frac{dM}{dt} = k(M(t) - M_\infty)$$

There is extrinsic kinetic data available for many different types of wood as well as pure components. Some of these have been compiled by Di Blasi (1993) and are shown in Table 2-4 below. The parameters vary considerably due to the complex chemistry of the thermal degradation, the complicated heat, mass and momentum transport occurring during the process, and effects of particle size (Di Blasi 1993). For example, such studies often neglect the temperature variation during sample heat-up and consider only the final temperature as reaction temperature. The variation of the sample temperature has been cited as the main reason for the wide deviations of the activation energy for the weight loss reaction reported in the literature (Thurner & Mann 1981). One-step multi-reaction models also neglect secondary reactions and transport phenomena. Therefore, kinetic parameters are valid only for correlating experimental data under the conditions from which they were derived (Di Blasi 1993).

Table 2-4. Kinetic data for one-step global reactions. (Di Blasi 1993)

Sample	T(K)	E(kJ mol^{-1})	A(s^{-1})
α-cellulose	550–1000	79.4	1.7×10^4
Cellulose	600–850	100.5	1.2×10^6
Fir wood	300–1100	101.7 + 142.7X	2.1×10^8
Cellulose	580–1070	8.8–33.4	0.019–0.14
Beech sawdust	450–700	18 (T < 600)	0.0053
Beech sawdust	450–700	84 (T > 600)	2.3×10^4
Cellulose	450–700	71	6.79×10^3
Cellulose	520–1270	139.6	6.79×10^9
Cellulose	520–1270	166.4	3.9×10^{11}
Lignin	520–1270	141.3	1.2×10^8
Hemicellulose	520–1270	123.7	1.45×10^9
Wood	321–720	125.4	1.0×10^8
Almond shell	730–880	95–121	1.8×10^6

Di Blasi (2004) used a single step reaction, Eq. 5 below, in a multi-physics, fixed bed simulation.

Eq. 5 $$W \xrightarrow{k_1} \nu_C CHAR + \nu_{CO} CO + \nu_{CO2} CO_2 + \nu_{H2} H_2 + \nu_{CH4} CH_4 + \nu_T TAR$$

Gas product coefficients used by Di Blasi (2004): $\nu_{CO} = 0.045$, $\nu_{CO2} = 0.10$, $\nu_{CH4} = 0.003$, $\nu_{H2} = 0.002$, $\nu_{H2O} = 0.115$

The coefficients were determined from prior experiment results and are given above (gases) and in Table 2-5 below (char and tar). The gas yield was assumed invariant while the tar and char yields were coupled to the oxygen-fuel ratio, which affected the temperature.

Table 2-5. Char and Tar coefficients used in single-step reaction by Di Blasi (2004)

Temperature (°C)	ν_c	ν_t
450	0.350	0.385
515	0.315	0.420
560	0.285	0.450
575	0.255	0.480

The study considered the following single-step tar cracking reaction, also with fixed gas yield coefficients.

Eq. 6 $$TAR \xrightarrow{k_2} \nu^*_{CO} CO + \nu^*_{CO2} CO_2 + \nu^*_{CH4} CH_4$$

Tar product coefficients used by Di Blasi (2004): $\nu^*_{CO} = 0.70$, $\nu^*_{CO2} = 0.18$, $\nu^*_{CH4} = 0.12$

These coefficients were derived from the results of Boroson et al. (1989b), the aforementioned study on tar cracking of wood pyrolysis vapors. In that study, wood was pyrolyzed at 450 °C and the volatiles were cracked in a separate reactor at temperatures between 600 and 800 °C. The results, given in Table 2-3 above, reveal the temperature-dependent nature of the yields.

Considering that a large percentage of biomass evolves into volatiles (both gases and condensable vapors), the modeling of pyrolysis should be as accurate as possible. To add the ability to predict yields, multi-reaction models have been explored. Multi-step multi-reaction (competing pathway) models can also help avoid error caused by the lumping of several subsequent reactions into one.

The effect of using a multi-step model is shown in Figure 2-6 below, where one- and two-step model predictions for mass loss rate are compared with dynamic thermogravimetry data (Branca, Albano, et al. 2005). The one-step model shows large deviations, which increase with heating rate while the two-step model proves to be a significant improvement.

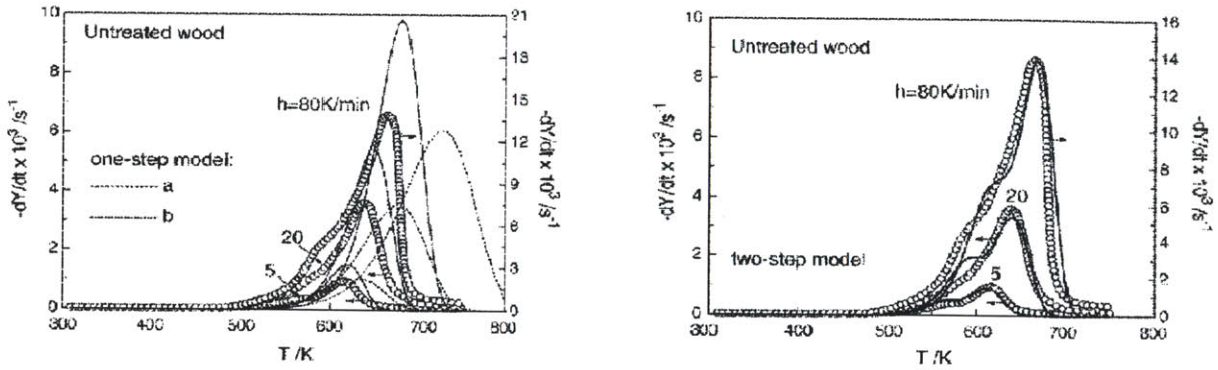

Figure 2-6. Comparisons of One- and Two-step devolatilization models (lines) with experiment data (symbols). (Branca, Albano, et al. 2005)

2.5.2 *MULTI-STEP, MULTI-REACTION MODELS*

The model proposed by Shafizadeh and Chin (1977) is given in Figure 2-7 below.

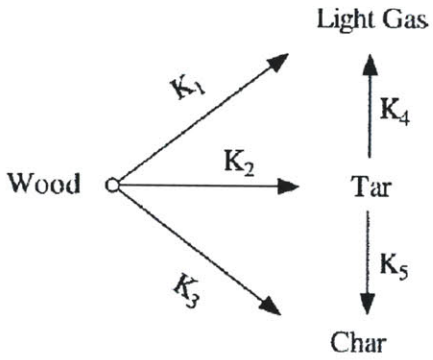

Figure 2-7. Shafizadeh and Chin (1977) two-step pyrolysis model.

One of the first studies to derive kinetic parameters with the model was Thurner and Mann (1981), from experiments on dried oak sawdust with a mean diameter of 840 μm in the temperature range of 300 – 400 °C. Considering the temperature range and particle size, it was assumed that kinetics controlled the reaction rate. The study also ignored reactions 4 and 5, assumed justifiable by quickly quenching the volatiles. The authors analyzed the gas and tar products and found that the gas was mainly carbon monoxide, carbon dioxide, oxygen, and C3 compounds with traces of methane, ethylene and acetylene. Tar was found to consist of seven compounds, with levoglucosan ($C_6H_{10}O_5$) making up more than half. The activation energy parameters derived by Thurner and Mann, displayed in Table 2-6 below, are very close for each of the three reactions, 1, 2 and 3. While this multipath, multistep reaction was meant to predict yields based on heating and temperature conditions, the narrow range of activation energies leads to very small variation in yields as temperature varies. The yields as predicted by activation energies K1-K3 in Table 2-6 and coupled with tar cracking kinetics from Liden et al. (1988) and tar re-polymerization kinetics from Di Blasi (1993) are summarized in Table 2-7 below. The temperature dependence is most evident in the char yields. The variation in gas and tar is due to gas cracking

reactions, which are first appreciable at 300 °C. The lack of variation among the activation energies may be due to the low temperature range from which they were derived and suggests that the parameters would not be representative of pyrolysis at higher temperatures.

Table 2-6. Thurner and Mann (1981) Kinetic Data: Activation energies are relatively similar.

Reaction	Activation Energy (kJ/kmol)
K1	88.6
K2	112.7
K3	106.5

Table 2-7. Results of applying Thurner and Mann (1981) data at different temperatures until equilibrium: Char does not vary significantly, while secondary reactions cause Tar to go to Gas.

Temperature (°C)	Gas/Tar/Char (%)
300	32/38/30
400	69/0.5/30.5
600	72/0/28

Wagenaar et al. (1993) also found kinetic parameters for the primary reactions of the Shafizadeh/Chin mechanism, for pine sawdust screened to diameters of 100 to 215 μm in the temperature range of 300 – 600 °C. The Biot number (ratio of external to internal heat transfer) was assumed low and the external pyrolysis number (kinetic rate compared to external heat transfer) was assumed high, meaning the reactions were assumed kinetically controlled – see Pyle and Zaror (1984). While they attempted to isolate the primary reactions by quenching the products, their product yield results reflected the effect of tar cracking as the reaction temperature increased, revealing that the apparatus was not ideal. The activation energies of reactions 1-3 are given in Table 2-8 below. The parameters are more varied than those of Thurner and Mann and the predicted yields, again coupled with tar cracking kinetics from Liden et al. (1988) and tar re-polymerization kinetics from Di Blasi (1993), vary considerably with varying reaction temperature, as summarized in Table 2-9 below. Figure 2-8 below shows the shape of curves for an isothermal reaction at 600 °C.

Table 2-8. Wagenaar et al. (1993) kinetic data: Relatively varied compare to Thurner and Mann (1981).

Reaction	Activation Energy (kJ/kmol)
K1	177
K2	149
K3	125

Table 2-9. Results of applying Wagenaar et al. (1993) data at different temperatures until equilibrium:

Temperature (°C)	Gas/Tar/Char (%)
400	79.5/1.5/19
500	88.6/0/11.4
600	92.6/0/7.4
700	94.8/0/5.2
800	96.2/0/3.8

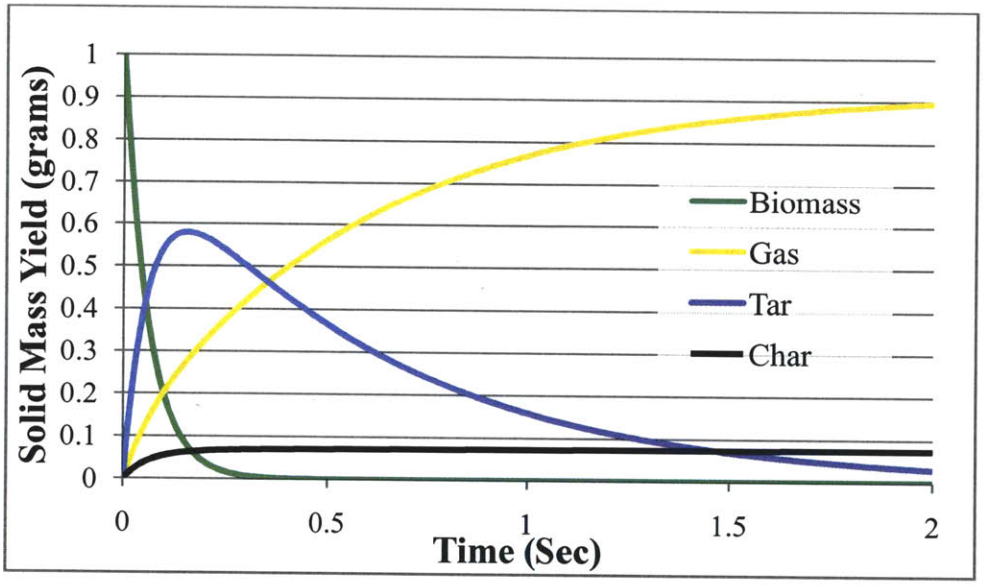

Figure 2-8. Calculated reaction curves using Wagenaar et al. (1993) data for pyrolysis reaction: Isothermal at 600 °C.

In trying to go to higher temperatures, it is necessary to consider external heat transfer. To approximate the effects of heat transfer, the yields were plotted (Figure 2-9) with a temperature profile that matches the heat up of a lumped capacitance. Heat of reaction is ignored. The temperature profile is also displayed, which spans from 100 °C (just after drying) towards 1400 °C (typical co-gasification temperature). The figure reveals that pyrolysis starts and finishes before the particle reaches the target temperature. Compared to the 600 °C case, it exhibits the change in char yield and the reaction time is about ten times shorter.

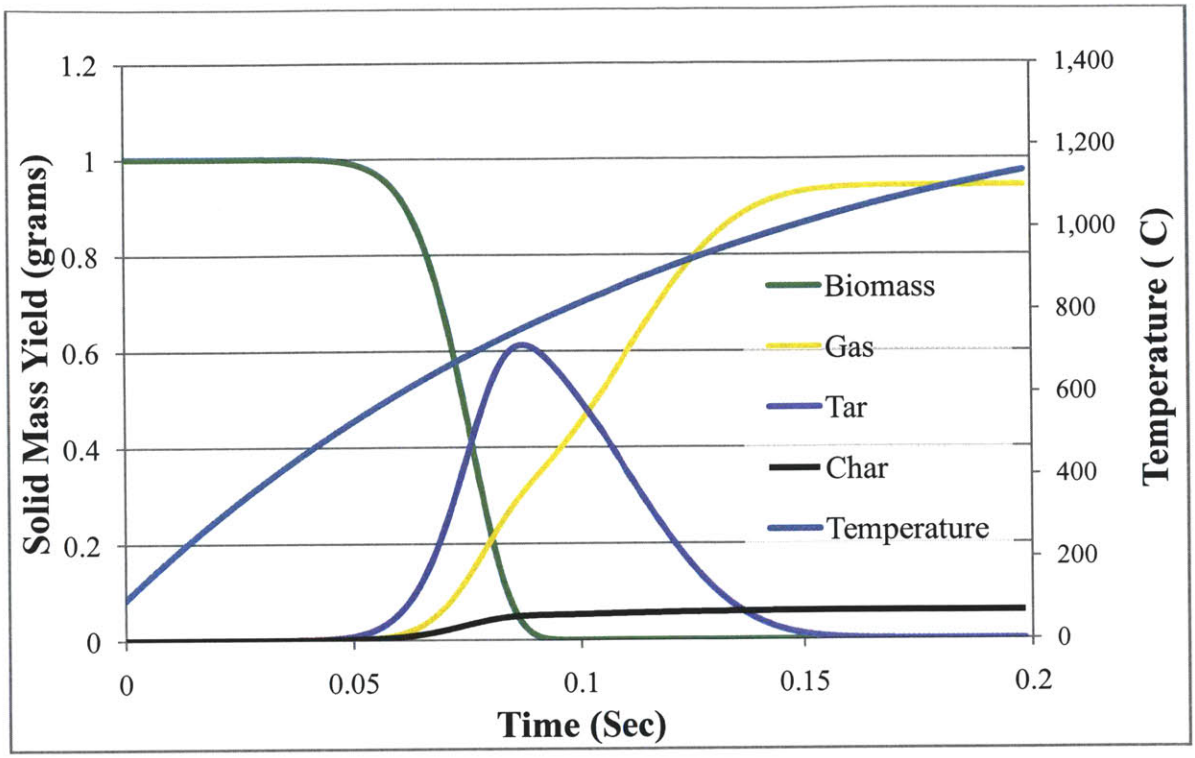

Figure 2-9. Yields using Wagenaar et al. (1993) data for Pyrolysis Reaction: Lumped capacitance approximation (dictated temperature history), with temperature heat-up from 100 to 1400 °C

The aforementioned studies considered whole wood, but another body of research considers devolatilization of three components of biomass. They ignore the interactions between the components, but this gives added flexibility for representing various biomass types. For example, using the same kinetics for each of the three components, one can describe the pyrolysis of high cellulose softwood as well as high hemicellulose switch grass.

An example of a multi-reaction, multi-stage mechanism that considered the sum of components is Koufopanos et al. (1989). The mechanism (Figure 2-10) was adapted from one generally called the Broido – Shafizadeh mechanism for cellulose degradation, detailed in Bradbury et al. (1979)). These mechanisms use an intermediate step to represent the depolymerization of components, which does not result in weight loss, and accounts for a time delay in experimental data. While this step was questioned by Vehgaryi et al. (1994), it is still used to different extents in contemporary models.

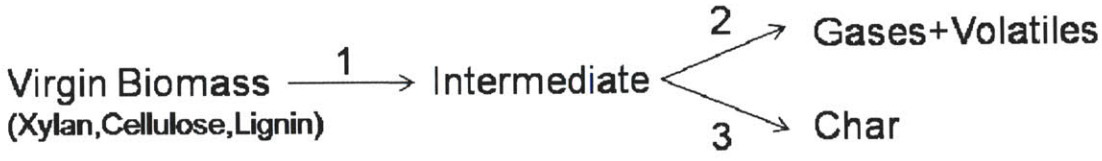

Figure 2-10. Koufopanos et al. (1989) pyrolysis mechanism, adapted from Broido - Shafizadeh mechanism.

The Koufopanos et al. (1989) study applied the above mechanism to fast pyrolysis on sawdust particles with 300 – 850 μm diameters in temperatures up to 700 °C. Koufopanos et al. (1991) concluded that the requirement for achieving fast pyrolysis, where internal heat transfer is not limiting, compared to slow pyrolysis, where internal heat transfer must be considered, is particle size less than 1 mm in characteristic diameter.

The results of applying this mechanism and the derived kinetic parameters are reported for a range of temperatures in Table 2-10 below.

Table 2-10. Results of applying Koufopanos et al. (1989) data at different maximum temperatures (isothermal, very fast heat up) until equilibrium:

Temperature (°C)	Gas+Tar/Char (%wt)
400	76.5/23.5
500	82.0/18.0
600	83.5/14.5
700	85.0/12.5
800	88.0/11.0

The curves for these parameters as the reaction proceeds from 350 °C to 600 °C, with a heating rate of 10^5 °C/min, are given in Figure 2-11 below. This temperature profile was used so that the quick activation reaction (reaction 1) is apparent in the figure. Results of the mechanism and associated kinetic parameters predict much higher char yield compared to the results using the data of Wagenaar et al. (1993) for a similar temperature.

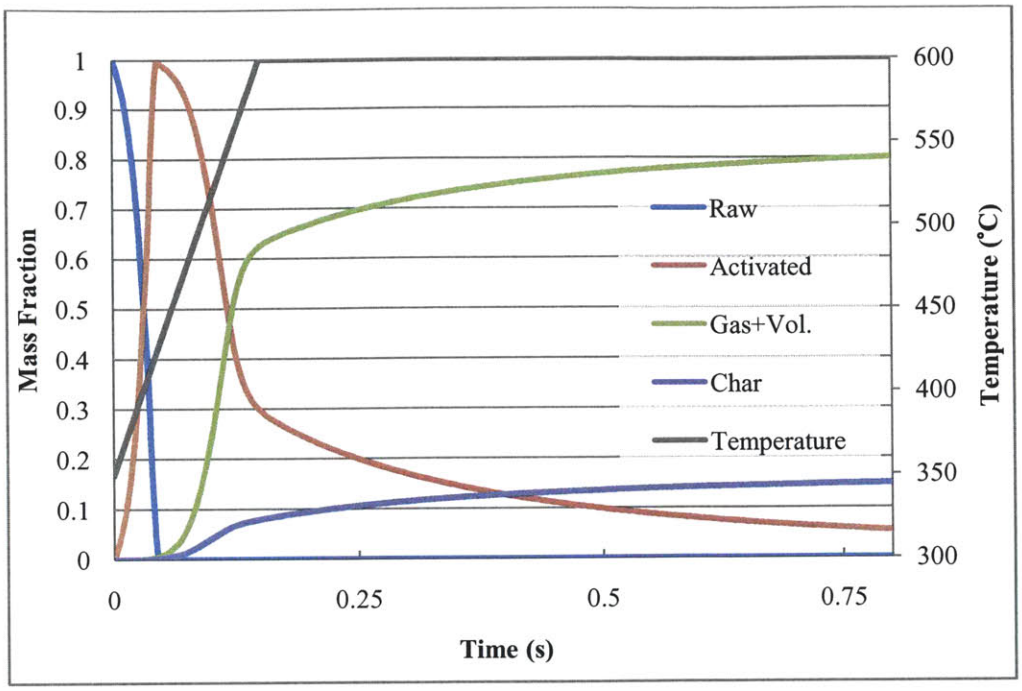

Figure 2-11. Yields as sums of components using Koufopanos et al. (1989) mechanism and data: Quick heat up to 600 °C.

The lumped capacitance described earlier was also applied to the Koufopanos mechanism and the results are in Figure 2-12 below. Again, a temperature profile was dictated that approximates the heat-up history of a lumped capacitance, from 100 °C to the expected co-gasification temperature of 1400 °C. The char and volatile yields are broken down by contributing bio-component, below in Figures 2-13 and 2-14, respectively. Through these breakdowns it is possible to observe that the model properly reflects certain characteristics of biomass components. Firstly, hemicellulose decomposes earliest. Second, cellulose mainly decomposes into gas and volatiles with a small remainder of char. Finally, lignin decomposes over a large span of temperatures and mainly contributes char (Koufopanos et al. 1989).

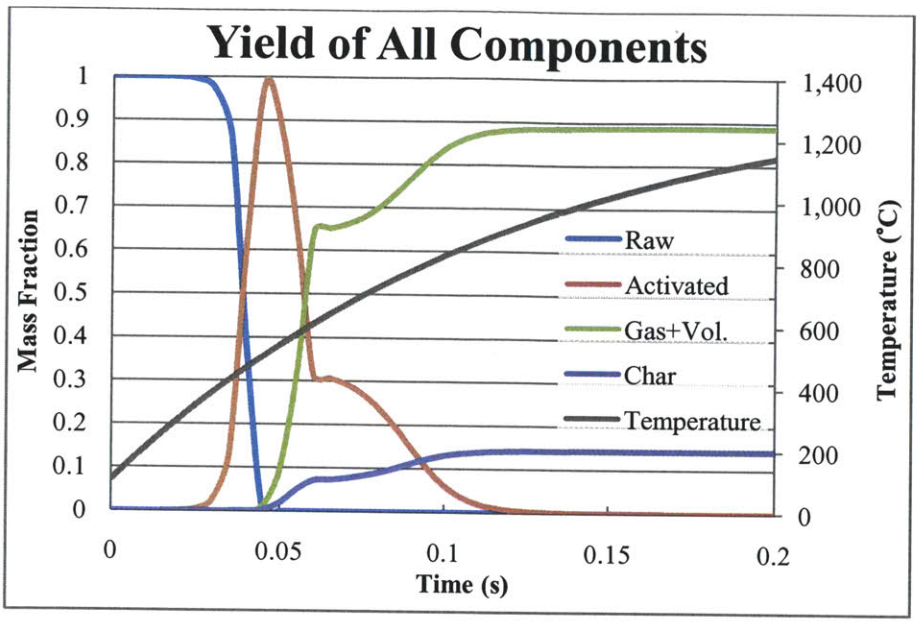

Figure 2-12. Yields as sums of components using Koufopanos et al. (1989) mechanism and data: Lumped Capacitance heat up to 1400 °C.

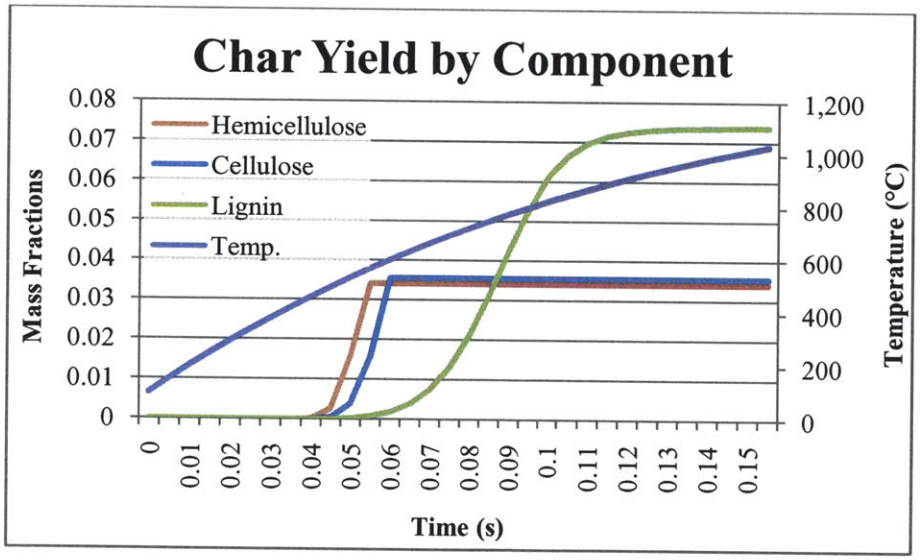

Figure 2-13. Breakdown of Char yields by component using Koufopanos et al. (1989) mechanism and data: Lumped Capacitance heat up to 1400 °C.

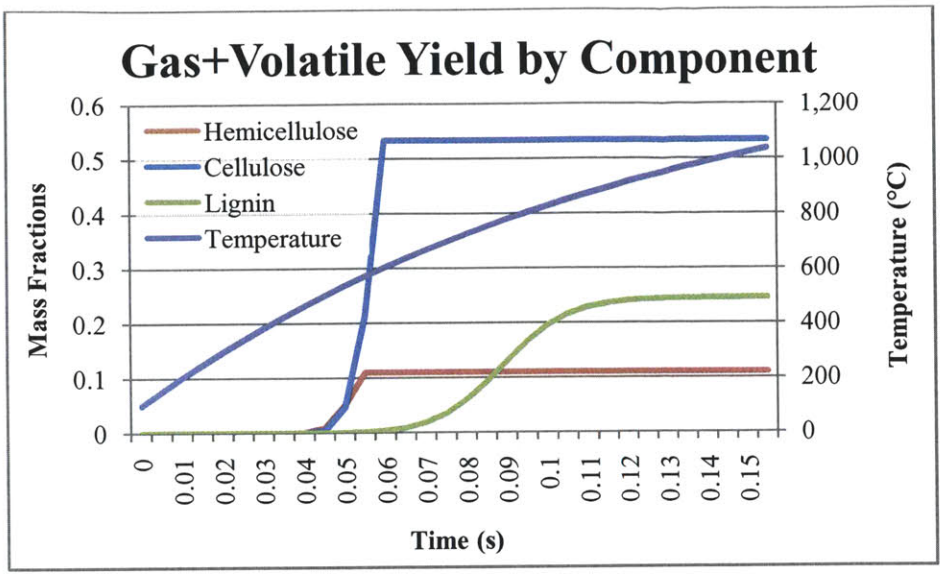

Figure 2-14. Breakdown of Gas and Volatile yields by component using Koufopanos et al. (1989) mechanism and data: Lumped Capacitance heat up to 1400 °C.

The fact that gas and tar yields are lumped is a disadvantage for this mechanism. Coupling the yields of this mechanism to secondary tar reaction mechanisms such as cracking and combustion is impossible. Therefore, it is necessary to use a model that also uses superposition of the main bio components but separates the yields.

One study recognized this need. Miller and Bellan (1997) adopted the cellulose pyrolysis mechanism of Di Blasi (1994) and applied it to hemicellulose and lignin. This mechanism, illustrated in Figure 2-15 below, allows for the separate accounting of char, gas and tar. They adapted kinetic data from other studies including Ward and Braslaw (1985) for hemicellulose and Koufopanos et al. (1991). The computed results using this mechanism are given in Figure 2-16 below. When applying this model with high heating rates and high reactor temperatures and atmospheric pressure, they found good agreement with experimental measurements from the literature. However, it was found that the model does not accurately predict yields of pyrolysis under vacuum. This signals that the effect of pressure, particularly high pressure on the order of that used in commercial EFG, should be considered in future studies.

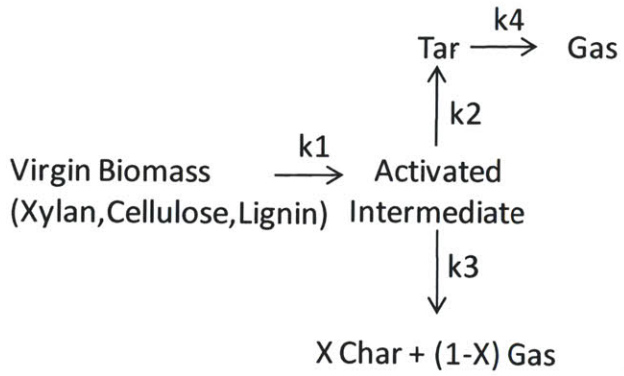

Figure 2-15. Miller and Bellan (1997) Pyrolysis Mechanism, adapted from Di Blasi (1994).

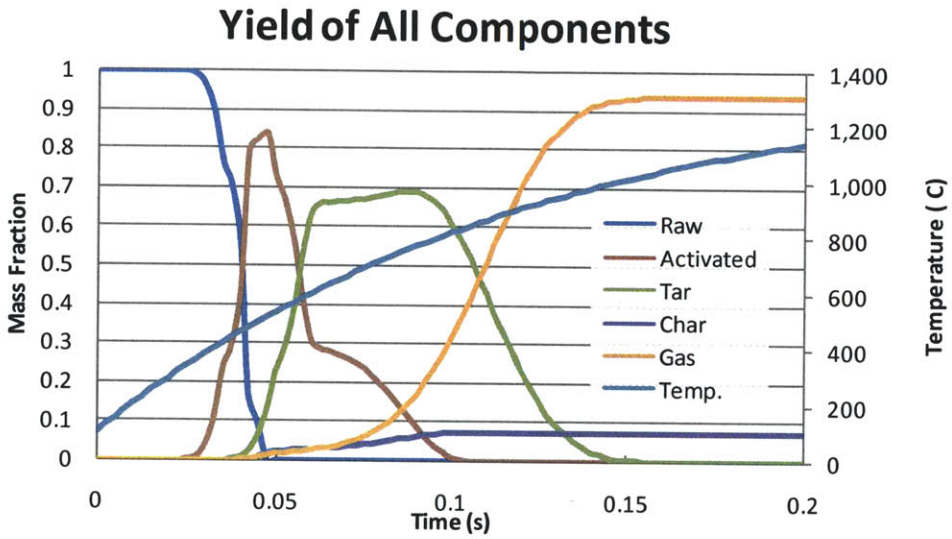

Figure 2-16. Miller and Bellan (1997) simulated Volatile Yields.

The Miller and Bellan study separates the yields three ways but does not describe the composition of the char, tars or gas. The output is helpful for validating more detailed work, but it is not suitable for integration into the ROM. Without chemically defined products, balancing atoms and energy is impossible.

In recent years, molecule and compound identification technology (e.g. micro gas chromatography and Fourier Transform Infrared spectrometers) has become more accessible. This has allowed pyrolysis experiments to get closer to the ideal arrangement of real-time, detailed chemical tracking with the purpose of constructing detailed reaction mechanisms.

Ranzi et al. (2008) combines conventional multistep devolatilization models similar to those described above with relatively detailed, gas and heavy hydrocarbon data acquisition. This yields a primary reaction mechanism of 18 equations and 42 species. It also couples the relatively detailed, primary volatile yields with detailed secondary homogeneous reactions mechanisms, with over 2000 equations and 131 species, which describe the pyrolysis and oxidation of hydrocarbon species.

While the products are described in greater detail, the structures of the primary decomposition reactions used in Ranzi are borrowed from other studies. The cellulose decomposition mechanism, illustrated in Figure 2-17 below, was first suggested by Bradbury et al. (1979). Ranzi delineates the Decomposition Products as certain stoichiometric amounts of hydroxyl-acetaldehyde (HAA), Glyoxal, CH_3CHO, C_3H_6O, 5-hydroxymethyl-furfural (HMFU), CO_2, CO, CH_4, H_2O, and char. In this study, cellulose is modeled as a polymer of $C_6H_{10}O_5$ monomers and char is modeled as graphite. Similarly structured, more complex mechanisms are provided for hemicellulose and lignin.

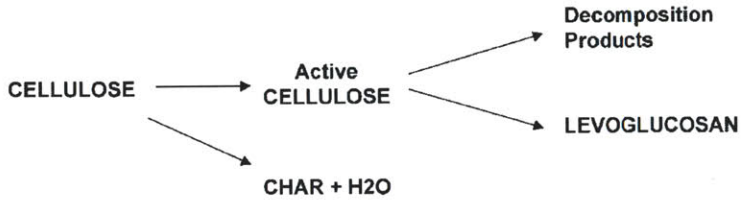

Figure 2-17. Simplified depiction of Cellulose decomposition mechansim used by Ranzi et al. (2008).

The mechanisms and kinetics offered by this study are of sufficient detail and were validated at sufficiently high temperature experiments (up to 800 °C) to be used in Reduced Order Modeling of Entrained Flow Gasification. This decision is partly validated by the use of this mechanism by Du Pont et al. (2008). That study involved pyrolysis at high temperature (800 – 950 °C) of small particles (200-850 microns) in an Entrained Flow Reactor. The adaptation of the Ranzi mechanism to the ROM will be described in a later section.

2.6 Char Conversion

Char conversion by heterogeneous reactions includes oxidation, gasification and methanation. These are given in simple form in Eqs. 7 - 10 below. For coal, the equations include char-bound hydrogen, oxygen, nitrogen and sulfur, and the gaseous products that result from liberating these elements.

Eq. 7 $$C + \frac{1}{\phi} O_2 \xrightarrow{k_1} 2\left(1 - \frac{1}{\phi}\right) CO + \left(\frac{2}{\phi} - 1\right) CO_2$$

Eq. 8 $$C + H_2O \xrightarrow{k_2} CO + H_2$$

Eq. 9 $$C + CO_2 \xrightarrow{k_3} 2CO$$

Eq. 10 $$C + 2H_2 \xrightarrow{k_4} CH_4$$

The reactions are often modeled as intrinsic functions of Arrhenius kinetics, partial pressure of reactant, reactant diffusion and particle surface area. One example of an intrinsic model is the shrinking core model, which accounts for the change in external surface area as conversion proceeds for a particle.

The model is depicted in Figure 2-18 below. As the char at the external surface is consumed, the surface recedes toward the center. A layer of porous ash is left around the char, through which reactants must diffuse to reach the char surface.

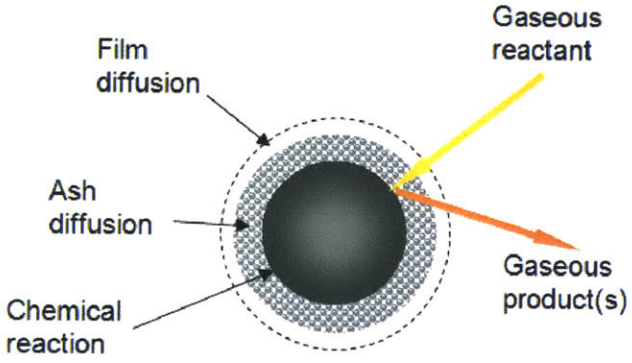

Figure 2-18. Shrinking Core Model for char conversion. (Monaghan 2009)

The rate at which the reaction may proceed thus depends on the rate of diffusion of reactants to the gas film around particle, the rate of diffusion of reactants through the ash layer, and finally the rate of chemical reaction at the surface. The rate of "i-th" heterogeneous reaction is given in Eq. 11 below.

Eq. 11 $$rate_i = \frac{P_i}{\frac{1}{k_{diff,i}} + \frac{1}{k_{reac,i}\left(\frac{r}{R}\right)^2} + \frac{1}{k_{d,ash,i}}\left(\frac{1}{r/R} - 1\right)}$$

The effect of internal surface area in porous char can be appreciable compared to external surface area if diffusion through the particle is faster than the reaction at the surface. The ROM does not use the shrinking core model, but instead accounts for this by using effectiveness factors. These are based on the Thiele Modulus, which is the ratio of intrinsic chemical reaction rate in the absence of mass transfer limitation to the rate of diffusion through the particle. In addition, ROM models the initial surface area as a function of initial proximate analysis by Liu's model. Instead of using the shrinking core model, however, it captures the surface area evolution according to the Random Pore Model.

Eq. 12 $$a_{p,int} = a_{p,int,0}(1 - X)\sqrt{1 - \psi \ln(1 - X)}$$

In the equation above, $a_{p,int}$ is the specific internal surface area of a particle, X is the particle conversion on mass basis, and ψ is a structural parameter. The extrinsic coal kinetics (High-sulfur bituminous coal, Illinois No. 6) used in the co-feeding simulation are tabulated in Table 2-11.

Table 2-11. Coal kinetics expressions and parameters. Source: Kajitani (2002), coal type: NL with correction factors

Conversion type	Expression with Parameters (Frequency factors 1/MPa^n/s, Activation energies MJ/kmol)
CO_2 Gasification	$k = .0710603 \exp(-130/RT) P_{CO2}^{.54}$
H_2O Gasification	$k = 302.06 \exp(-140/RT) P_{H2O}^{.64}$
O_2 Combustion	$k = 349.031 \exp(-163/RT) P_{O2}^{.68}$

Biomass char reactions can be modeled with the same approaches used for coal, including the shrinking core model for external surface area (Di Blasi 2004). However, since woody biomass has such a small fraction of ash, the ash layer diffusion can be ignored in the conversion rate equation. Only kinetics and film-diffusion are considered, as in Eq. 13 below.

Eq. 13 $$rate_i = \frac{P_i}{\frac{1}{k_{diff,i}} + \frac{1}{k_{reac,i}\left(\frac{r}{R}\right)^2}}$$

The conversion rates described above are good for being applicable over a wide range of conditions but require detailed information about the char particles. In most cases, biomass kinetic data is offered in a simpler, global form, as a chemical kinetic term accounting for temperature and reactant partial pressure, along with some structural term, a function of conversion:

Eq. 14 $$R = r_c(T, P_i) \times r_s(X)$$

An expression of the form in Eq. 14 above must be supplied along with a range of conditions of validity. This is because the structural profile is not completely invariant of temperature and pressure. Also, the char morphology, and thus reactivity, is greatly affected by the pyrolysis conditions under which the char is formed. This will be discussed further in Section 2.7, Effect of Pyrolysis on Char Conversion.

Di Blasi (2009) compiled gasification and combustion conversion rate expressions and parameters from dozens of experimental studies. They are presented in Tables 2-12 through **Error! Reference source not found.** below. It is important to note that the majority of the experiments were carried out at atmospheric pressure, and that reliable high pressure data could not be identified at the time of this literature review.

Table 2-12. Char gasification rates in CO2. (Di Blasi 2009)

Authors (Ref.)	$\frac{dX}{dt}$ [s^{-1}]; k [s^{-1}]	T_g [K]	P_{CO_2} [kPa]	Pyrolysis conditions
Groeneveld and van Swaaij [162]	$\frac{dX}{dt} = \frac{2.88\times(10^5+10^6)}{T^{0.7}}\exp(-\frac{217}{RT})(P_{CO_2}+P_{H_2O})^{0.7}[(1-X)]$	1073–1273	0.88–23; p_{H_2O} = 0.44–3.1 kPa	Wood char powder
De Groot and Shafizadeh [161]	$\frac{dX}{dt} = 2.59\times10^8\exp(-\frac{200}{RT})P_{CO_2}^{0.6}[-]$ (Douglas fir) $\frac{dX}{dt} = 4.85\times10^7\exp(-\frac{196}{RT})P_{CO_2}^{0.6}[-]$ (Cotton wood)	973–1173	0.05–0.5	Slow pyrolysis of wood (0.8 × 0.4 mm) at 1273 K
Van den Aarsen et al. [165]	$\frac{dX}{dt} = \frac{9.10\times10^5}{T^{0.3}}\exp(-\frac{166}{RT})P_{CO_2}^{0.8}[(1-X)^{2/3}]$	1023–1273	4.8–38.5	Fluidized-bed pyrolysis of beech wood (1–2 mm) at 1023–1273 K
Plante et al. [148]	$\frac{dX}{dt} = 83.18\times10^7\exp(-\frac{80.3}{RT})P_{CO_2}^{1.2}[(1-X)^aX^b]$: E = 82–126 kJ/mol, A = 78–1535 $MPa^{-n}s^{-1}$, n = 0.7–1.2 (pyrolysis and gasification pressure, pre-heating rate)[a]	998–1233	101–6000	Slow pyrolysis of poplar wood (0.4–0.8 mm) at 813 K (atmospheric pressure or under vacuum)
Bandyopadhyay et al. [133]	$K = A\exp(-\frac{250}{RT})$	1081–1280	80–20 ; p_{CO}/p_{CO_2} = 0.25–4	Coconut shell char (0.1 mm)
Rodriguez-Mirasol et al. [166]	$K = A\exp(-\frac{E}{RT})$: E = 202–245 kJ/mol (X, pyrolysis conditions)	1023–1223	101	Slow pyrolysis of eucalyptus Kraft lignin at 823–1673 K; (0.045–0.053) mm char
Kumar and Gupta [113]	$K = A\exp(-\frac{E}{RT})$: E = 151–218 kJ/mol acacia (slow pyrolysis temperature); E = 180–213 kJ/mol Eucalyptus (slow pyrolysis temperature); E = 138 kJ/mol (fast pyrolysis)	1023–1223	101	Slow pyrolysis of wood (7 mm) at 1073–1473 K; fast pyrolysis of wood at 1073 K
Moilanen and Saviharju [115]	$K = A\exp(-\frac{229}{RT})$	973–1173	101	Pyrolysis at 10 K/s of pine sawdust (0.1 mm)
Tancredi et al. [158]	$K = A\exp(-\frac{E}{RT})$: E = 236–261 kJ/mol (X, pyrolysis temperature)	1043–1123	101	Slow pyrolysis of eucalyptus wood (0.2 mm) at 673–1073 K
Cozzani [146]	$\frac{dX}{dt} = 4.2\times10^7\exp(-\frac{221}{RT})P_{CO_2}^{0.72}[(1-X)]$	10 K/min up to 1273	20–101	Slow pyrolysis of RDF at 723–1073 K
Bhat et al. [132]	$\frac{dX}{dt} = \frac{9.87\times10^{12}}{T}\exp(-\frac{197}{RT})p_{CO_2}[(1-X)]$	1023–1123	101	Slow pyrolysis of rice husk at 873–973 K; 0.001 mm char
Barrio and Hustad [116]	$\frac{dX}{dt} = 3.1\times10^6\exp(-\frac{215}{RT})P_{CO_2}^{0.38}[(F(X))]$	1023–1273	5–101; p_{CO}/p_{CO_2} = 0.1–1.25	Slow pyrolysis of birch wood at 873 K; (0.032–0.045) mm char
Risnes et al. [120]	$\frac{dX}{dt} = 5.81\times10^6\exp(-\frac{205.6}{RT})P_{CO_2}^{0.52}[(F(X))]$ (straw) $\frac{dX}{dt} = 2.11\times10^7\exp(-\frac{220}{RT})P_{CO_2}^{0.36}[(F(X))]$ (spruce)	973–1273	3–101	Pyrolysis in a pressurized entrained-flow reactor at 1173 K of straw (<0.15 mm) and spruce wood (<0.0006 mm)
Marquez-Montesinos et al. [157]	$K = A\exp(-\frac{E}{RT})$: E = 249–197 kJ/mol, $k_0 = 7.4\times10^8$–4.5×10^6 s^{-1} (X, untreated samples); E = 176–248 kJ/mol , $k_0 = 2.5\times10^7$–3.8×10^8 s^{-1}(X, water extracted samples)	998–1073	101	Slow pyrolysis of grapefruit peels (1–1.6 mm) at 973 K
Ollero et al. [112]	$\frac{dX}{dt} = 1.68\times10^5\exp(-\frac{133}{RT})P_{CO_2}^{0.43}[(F(X))]$	1072–1223	20–50; p_{CO}/p_{CO_2} = 0–0.57	Slow pyrolysis of olive residues at 1173 K; char (<0.15 mm)
Gomez-Barea et al. [129]	$\frac{dX}{dt} = 1.99\times10^3\exp(-\frac{142.6}{RT})P_{CO_2}^{0.4}[(F(X))]$	1073–1173	20–50	Slow pyrolysis of olive residue at 1173 K; char (<0.06 mm)

[a] Pyrolysis and gasification at atmospheric pressure, pre-heating rate 13 K/min.

Table 2-13. Char gasification rates in H2O. (Di Blasi 2009)

Authors (Ref.)	$\frac{dX}{dt}$ [s^{-1}]; k [s^{-1}]	T_g [K]	P_{H_2O} [kPa]	Pyrolysis conditions
Rensfeldt et al. [167]	$K = 2 \times 10^6 \exp(-\frac{182}{RT})$ (polar) $K = 9.8 \times 10^5 \exp(-\frac{182}{RT})$ (straw) $K = 1.5 \times 10^6 \exp(-\frac{178}{RT})$ (bark)	1043–1123	74	Slow pyrolysis
Hawley et al. [168]	$\frac{dX}{dt} = 6.57 \times 10^3 \exp(-\frac{156}{RT}) P_{H_2O}[-]$	1073–1273	0.88–23	Pyrolysis of poplar wood (1–2 mm) at 973 K
Nandi and Onischak [117]	$\frac{dX}{dt} = 5.55 \times 10^5 \exp(-\frac{177}{RT})[(1-X)]$ (maple, $p_{H_2O}/p_{N_2} = 1$), $\frac{dX}{dt} = 1.7 \times 10^5 \exp(-\frac{170}{RT})[(1-X)]$ (pine, $p_{H_2O}/p_{N_2} = 1$): $E = 170$–196 kJ/mol (feedstock, gas composition)	1000–1200	1085; $p_{H_2}/p_{H_2O} = 0$–0.1	Slow pyrolysis of wood (1–1.4 mm) at 1000–1200 K followed by gasification
Nandi and Onischak [117]	$\frac{dX}{dt} = 4.08 \times 10^5 \exp(-\frac{167}{RT})[(1-X)]$ (maple, $p_{H_2O}/p_{N_2} = 1$), $\frac{dX}{dt} = 2.14 \times 10^5 \exp(-\frac{164}{RT})[(1-X)]$ (pine; $p_{H_2O}/p_{N_2} = 1$): $E = 164$–266 kJ/mol (feedstock, gas composition)	977–1144	1085; $p_{H_2}/p_{H_2O} = 0$–0.5	"In situ" gasification of (1.4–1 mm) wood at 977–1144 K
Hemati and Laguerie [131]	$\frac{dX}{dt} = 1.23 \times 10^7 \exp(-\frac{198}{RT}) p_{H_2O}^{0.75}[(1-X)]$	923–1273	21–100	Slow pyrolysis of wood sawdust at 923–1273 K
Kojima et al. [169]	$\frac{dX}{dt} = 1773 \exp(-\frac{129}{RT}) P_{H_2O}^{0.41}[-]$	1123–1223	0–58	Sawdust pyrolysis in a fluidized bed at 1123–1223 K
Moilanen et al. [118]	$K = A\exp(-\frac{196}{RT})$	1050–1220	15	Slow pyrolysis of wood (2–4 mm) at 1223 K
Moilanen and Saviharju [115]	$K = A\exp(-\frac{217}{RT})$	973–1173	101	Pyrolysis at 10 K/s of pine wood sawdust (0.1 mm)
Barrio et al. [119]	$\frac{dX}{dt} = 2.62 \times 10^8 \exp(-\frac{237}{RT}) P_{H_2O}^{0.57}[(F(X))]$ (birch) $\frac{dX}{dt} = 1.71 \times 10^7 \exp(-\frac{211}{RT}) P_{H_2O}^{0.51}[(F(X))]$ (beech)	1023–1223	10–30; $p_{H_2} = 5$–50 kPa	Slow pyrolysis of wood at 873 K; (0.045–0.063) mm char
Marquez-Montesinos et al. [157]	$K = A\exp(-\frac{E}{RT}) P_{H_2O}^n$: $E = 143$–201 kJ/mol, $n = 0.57$–0.73 (p, X)	998–1173	1.7–47.4	Slow pyrolysis of grapefruit peels (1–1.6 mm) at 993 K
Bhat et al. [132]	$\frac{dX}{dt} = \frac{2.93 \times 10^{13}}{T} \exp(-\frac{200.3}{RT}) p_{H_2O}[(1-X)]$	1023–1173	101	Slow pyrolysis of rice husk grain at 873–1173 K

Table 2-14. Char oxidation rates with parameter values. (Di Blasi 2009)

Authors (Ref.)	$\frac{dX}{dt}$ [s^{-1}]; k [s^{-1}]	Heating rate [K/min]; final temperature [K]	% Vol O_2 (in N_2)	Pyrolysis conditions
Kashiwagi and Nambu [86]	$\frac{dX}{dt} = 1.73 \times 10^8 \exp(-\frac{160}{RT}) p_{O_2}^{0.78}[(1-X)]$	0.5–5; 823	0.28–21	Slow pyrolysis of cellulose powder
Luo and Stanmore [122]	$\frac{dX}{dt} = A\exp(-\frac{180}{RT}) p_{O_2}^{0.65}[(1-X)]$	15; 973	0–21	Slow pyrolysis of sugar cane bagasse
Magnaterra et al. [175]	$\frac{dX}{dt} = A\exp(-\frac{E}{RT}) P_{O_2}^n [S/S_0]$: $E = 85$–125 kJ/mol, $n = 0.75$–0.85 (hardwoods); $E = 81$ kJ/mol, $n = 0.8$ (lignin)	Isothermal oxidation at 623–753 K	2–18	Slow pyrolysis of hardwoods and lignin
Janse et al. [134]	$\frac{dX}{dt} = 5.3 \times 10^5 \exp(-\frac{125}{RT}) p_{O_2}^{0.53}[(1-X)^{0.49}]$	Isothermal oxidation at 573–773 K	2.25–36	Pine wood pyrolysis at 300 K/s up to 873 K
Di Blasi et al. [121]	$\frac{dX}{dt} = 1.51 \times 10^6 \exp(-\frac{109}{RT})[(1-X)^{1.2}]$ (pine): $E = 71$–109 kJ/mol (feedstock and oxidation conditions)	10; 673–873	21	Slow pyrolysis of pine wood and agricultural residues at 800 K
Adanez et al. [176]	$\frac{dX}{dt} = 3.8 \times 10^7 \exp(-\frac{140}{RT})[(1-X)^{0.4}]$ (pine): $E = 134$–142 kJ/mol (feedstock)	20; 823	21	Slow pyrolysis of wood and agricultural residues
Zolin et al. [147]	$\frac{dX}{dt} = 1.31 \times 10^8 \exp(-\frac{134}{RT})[-]$ (low temperature) $\frac{dX}{dt} = 4.54 \times 10^8 \exp(-\frac{208}{RT})[-]$ (high temperature)	1–20; 1273	10	Slow pyrolysis of straw at 973–1673 K
Cozzani [146]	$\frac{dX}{dt} = 1.89 \times 10^9 \exp(-\frac{162}{RT}) p_{O_2}^{0.64}[(1-X)]$	10; 973	6–21	Slow pyrolysis of RDF at 723–1073 K
Branca et al [104]	$\frac{dX}{dt} = 1.4 \times 10^{11} \exp(-\frac{182.6}{RT})[(1-X)^{0.9}]$ (beech, slow pyrolysis, $v_c = 0.84$) $\frac{dX}{dt} = 1.11 \times 10^6 \exp(-\frac{114}{RT})[(1-X)^{0.86}]$ (beech, slow pyrolysis, $v_c = 1$) $\frac{dX}{dt} = 4.85 \times 10^{14} \exp(-\frac{228.6}{RT})[(1-X)^{1.16}]$ (beech, fast pyrolysis, $v_c = 0.87$)	5–15; 873	21	Slow and fast pyrolysis of beech wood at 800 K; slow pyrolysis of hardwoods and softwoods at 800 K
Varhegyi et al. [105]	$\frac{dX}{dt} = 8.12 \times 10^8 \exp(-\frac{151}{RT}) P_{O_2}^{0.53}[F(X)]$: $E = 142$–151 kJ/mol, $n = 0.53$–0.59 (pyrolysis conditions)	5–25; 573–733	20–100	Corncob flash carbonization at 1.4 MPa
Branca et al. [107]	$\frac{dX}{dt} = 1.85 \times 10^{10} \exp(-\frac{167}{RT})[(1-X)^2]$ ($v_c = 0.75$) $\frac{dX}{dt} = 1.7 \times 10^7 \exp(-\frac{129}{RT})[(1-X)^{1.85}]$ ($v_c = 1$)	5–15; 873	21	Slow pyrolysis of oak bark at 800 K

For those expressions above without partial pressure terms, the effects of partial pressure have been incorporated into the pre-exponential term. Therefore, the data is only valid at the specified pressure condition.

The chemical reactivity data for CO_2 gasification from 2-12 above is compared at a given pressure in Figure 2-19 below. Likewise, chemical reactivity data for H_2O gasification from Table 2-13 above is compared in at a given pressure in Figure 2-20.

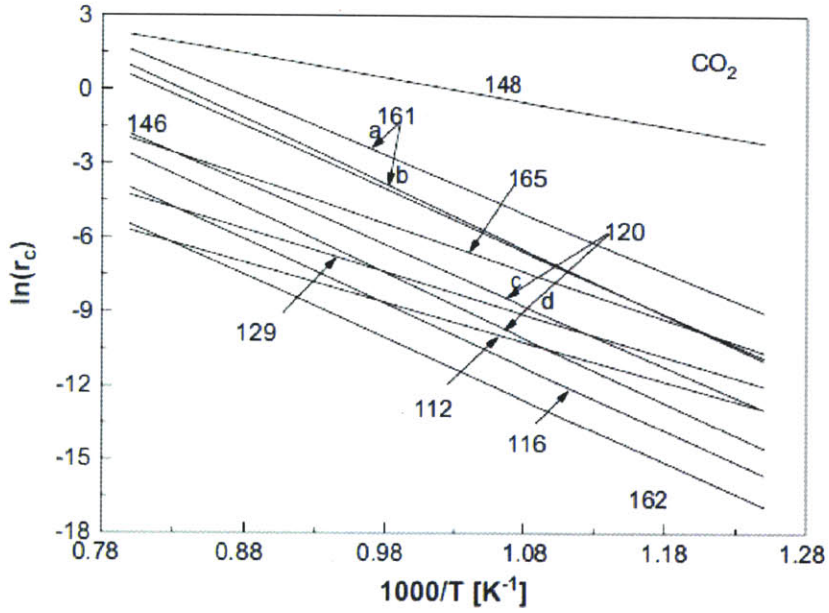

Figure 2-19. Arrhenius plot of the kinetic contribution, Rc, for CO2 gasification: (a) cotton wood, (b) Douglas fir, (c) straw, (d) spruce. Numbers refer to reference numbers in Table 2-12. (Di Blasi 2009)

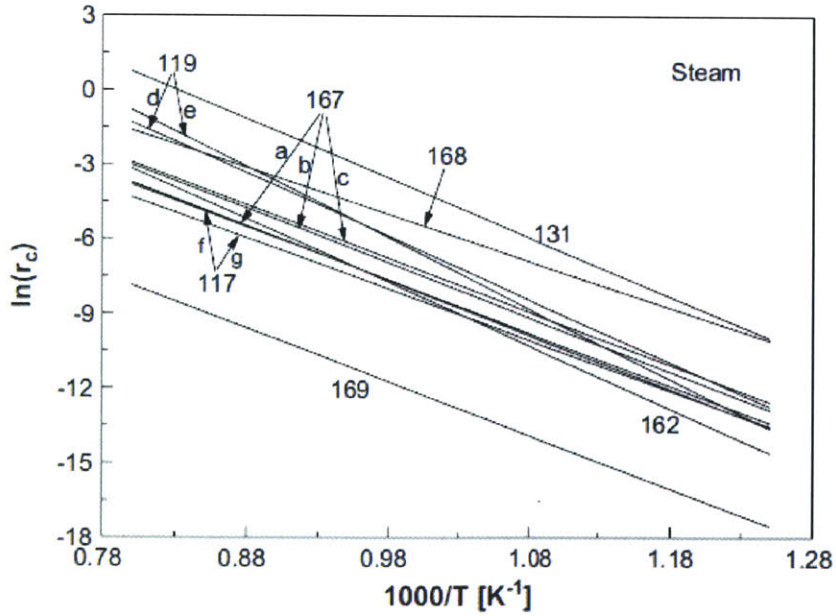

Figure 2-20. Arrhenius plot of the kinetic contribution, Rc, for H2O gasification: (a) straw, (b) poplar, (c) bark, (d) beech, (e) birch, (f) maple, and (g) pine. Numbers refer to reference numbers in Table 2-13. (Di Blasi 2009)

Another consideration for biomass is the low nitrogen and sulfur contents. Thus, while the heterogeneous reactions are mainly the same, these elements are often ignored in the char formula and reaction.

It is well documented that biomass char reactivity is higher than coal char reactivity due to the ash composition. Table 2-15 below gives a list of common ash elements and which reactions they catalyze, adapted from Di Blasi (2009). Such metals also influence the reactivity of coal char (Wen et al. 1979, p.98), but the respective contents are lower and less accessible due to the denser structure of coal char.

Table 2-15. Metals in biomass ash and the reactions they catalyze. (Di Blasi 2009)

Catalyst	For Process
Alkali metals (Na,K)	Oxidation
Oxides and Salts of Na, K	Steam Gasification
Oxides and Salts of Ca, Mg	Steam Gasification
K and Ca	CO_2 Gasification (linearly)
Alkali metals (Na,K)	Polymerization Reactions (char creation)

While the effects are known and the extent can be modeled as a scaling factor of the kinetic rate, such a factor is not easily determined, since even a trace amount of an impurity may significantly affect the measured kinetics. Also, catalysts affect not only the activation energy but also the pre-exponential factor of a reaction. Therefore, the catalytic effect is often not easily separated and simple kinetics (content-specific) must be considered (Wen et al. 1979, p.99).

2.7 Effect of Pyrolysis on Char Conversion

Char reactions depend on active carbon sites and the concentration of these sites depend on the morphology (e.g. porosity, effective surface area, etc.) of the char. The morphology is greatly affected by the conditions under which the char is formed. Thus, beyond ash content, char conversion reactivity is affected by pyrolysis conditions.

One factor is the pyrolysis heating rate. Slow pyrolysis allows volatiles to escape through natural porosity. During fast pyrolysis, on the other hand, there is substantial internal overpressure and coalescence of smaller pores, which lead to large internal cavities and a more open structure (Okumura et al. 2009). In a sense, the original cellular structure melts away. The more open structure results in a char that is more reactive. This can be seen in Figure 2-21 below, where consistent gasification conditions on char formed at different pyrolysis heating rate conditions exhibit different in reaction rates.

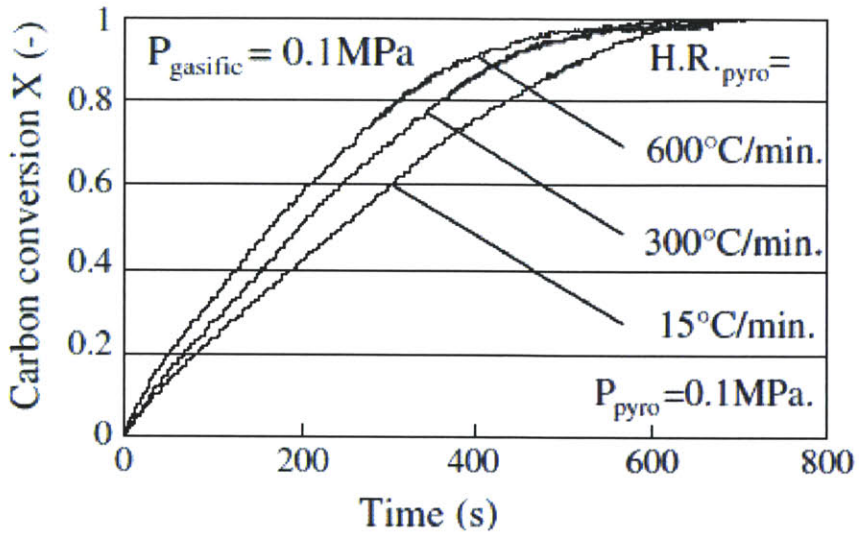

Figure 2-21. Carbon dioxide gasification at 900 °C of char produced under different heating rates. (Okumura et al. 2009)

Another factor affecting char reactivity is the final pyrolysis temperature. As the final temperature increases and approaches 800 °C, the specific surface area increases slightly due to swelling. Increased surface area improves reactivity. However, above 800 °C, reactivity is reduced as a result of structural ordering and micropore coalescence, which can be thought of as thermal deactivation and thermal annealing, respectively (Di Blasi 2009).

The strongest factor affecting char reactivity is pyrolysis pressure. High pressure reduces the effective surface area and increases graphitization resulting in greatly reduced reactivity, as seen in Figure 2-22 below. This observation is consistent with the effect of secondary char, which is of lower reactivity than primary char, and is promoted by high pyrolysis pressure.

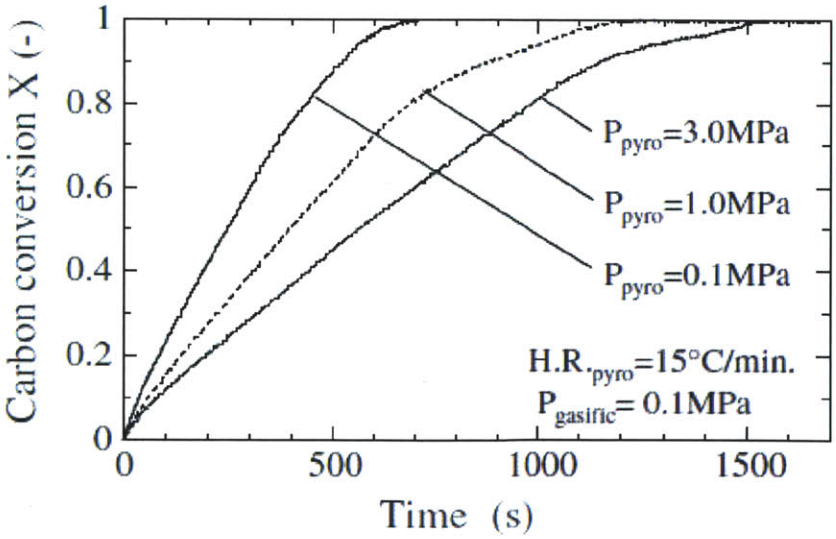

Figure 2-22. Carbon dioxide gasification at 900 °C on char produced under different pressures. (Okumura et al. 2009)

The SEM images in Figure 2-23 below demonstrate the effects of high pressure in case (a) and high heating rate in case (c), compared to the base case (b). Case (a) shows more ordered, tighter fibers in the cross section view and a smoother surface. Case (c) shows a more open cross section and surface.

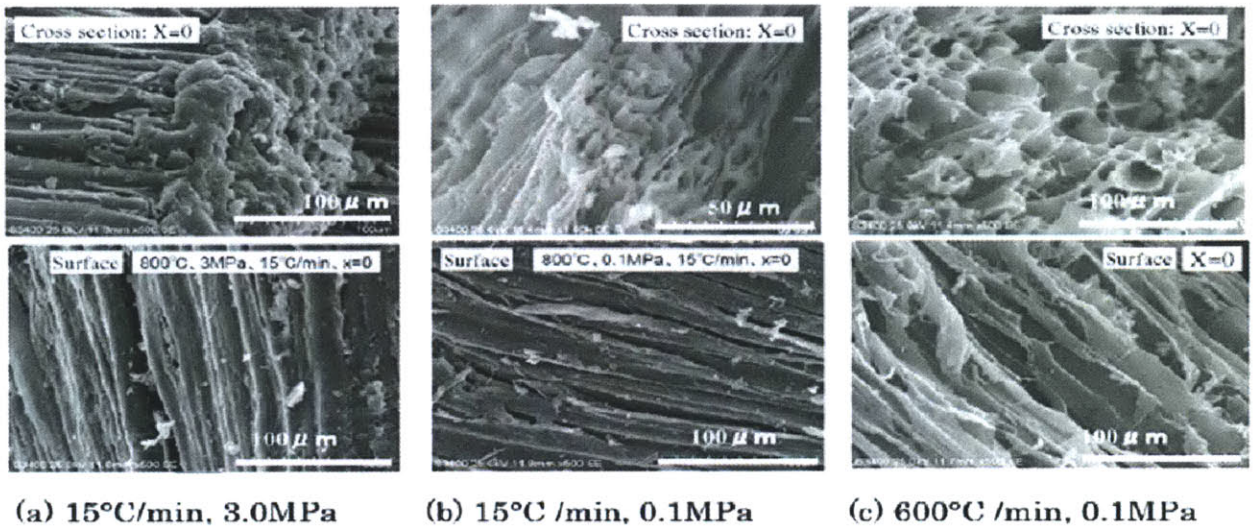

Figure 2-23. SEM images of pyrolysis effects on char, showing (a) High Pressure, (b) Base Case and (c) High Heating Rate. (Okumura et al. 2009)

Okumura et al. (2009) attempted to reflect the effect of pyrolysis pressure in gasification modeling. It was found that the structural parameter (ψ) used in the Random Pore Model (Eq. 15) is suppressed at high pyrolysis pressure as seen in Figure 2-24 below.

Eq. 15 $$\frac{dX}{dt} = K_p(1-X)\sqrt{1-\psi(1-X)}$$

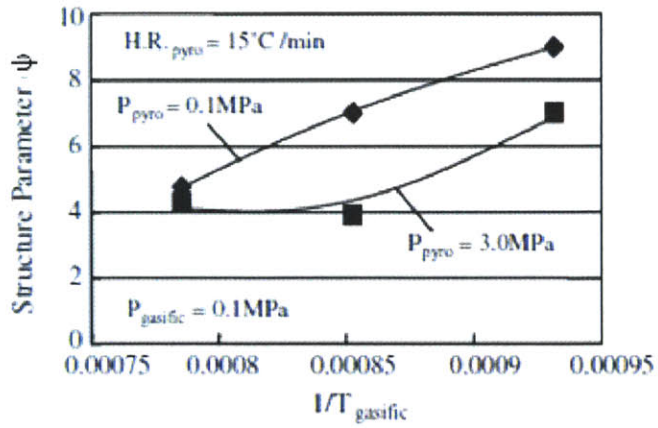

Figure 2-24. Demonstrating correlation between pyrolysis pressure and gasification structure parameter (ψ). (Okumura et al. 2009)

There is very little quantitative information available on the effect of pyrolysis on char reactivity. Even for the case of pyrolysis pressure, the plot in Figure 2-24 above could not be integrated into

available models. The lesson, however, is that detailed modeling should seek to apply heterogeneous kinetics data derived only from experiments with similar pyrolysis conditions.

However, in the case of a reduced order model, with a co-feed ratio of about 10% biomass and expected char yield around 10%, biomass char is expected to account for a very small mass in the reactor. Also, as diffusion becomes controlling at higher temperatures, the accuracy of kinetics will not be as important.

2.8 Ash Characteristics and Slag Modeling

There is limited published research into the ash slagging characteristics of woody biomass. This is probably because woody biomass is usually used in fixed bed and fluidized bed reactors, which are operated at temperatures below the melting temperature.

Ash viscosity is a complex function of the ash composition. For example, it is known that ashes high in silica content exhibit a high viscosity due to the network of –Si-O-Si bonds formed. However, network modifiers, like the cations Na^{+}, Mg^{++} and Ca^{++}, can break these bonds to produce smaller silicate network units, reducing viscosity. The effect of alumina depends on the majority composition; it acts as a network former in alkaline systems and a network modifier in silica system (Himes 2001).

Another way to look at this is the base-to-acid ratio (B/A), where metal oxides (Fe_2O3, CaO, MgO, Na_2O, K_2O) are considered bases and others (SiO_2, Al_2O_3, TiO_2) are considered acids (Himes 2001). The B/A ratio, as a function of ash composition in weight fractions, is defined in Eq. 16. The minimum fusion temperature is reached near a B/A ratio of 1:1, as seen in Figure 2-25.

Eq. 16 $$B/A\ ratio\ = \sum Fe_2O_3 + CaO + MgO + Na_2O + K_2O : \sum SiO_2 + Al_2O_3 + TiO_2$$

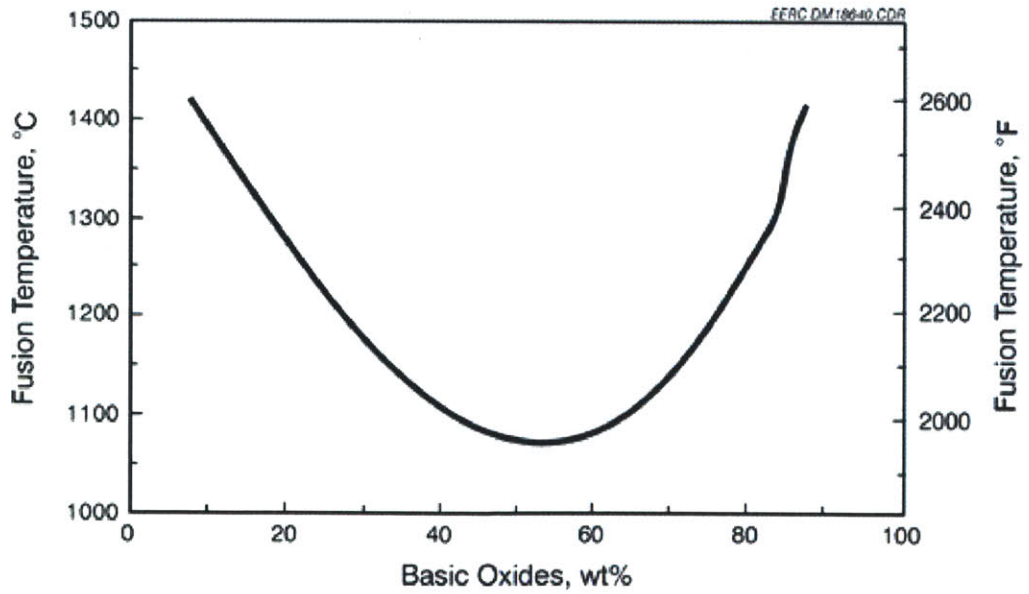

Figure 2-25. Ash Fusion temperature as a function of Base-to-Acid fraction.

Coda et al. (2007) found that woody biomass ash is mostly solid at temperatures between 1300 and 1500 °C due to its high calcium oxide content. They analyzed ash samples from experiments between 800 and 2000 °C. By looking at the mineral analyses from melted and unmelted area of ash samples (see Figure 2-26 below), they determined that silicon and calcium formed low-melting calcium silicate compounds. In certain experiments with willow wood, it appeared that higher phosphorous content enhanced the melting behavior. It was also found that where there was silicon present in the sample-collecting plates, high-melting wood ash particles were homogeneously incorporated upon impact.

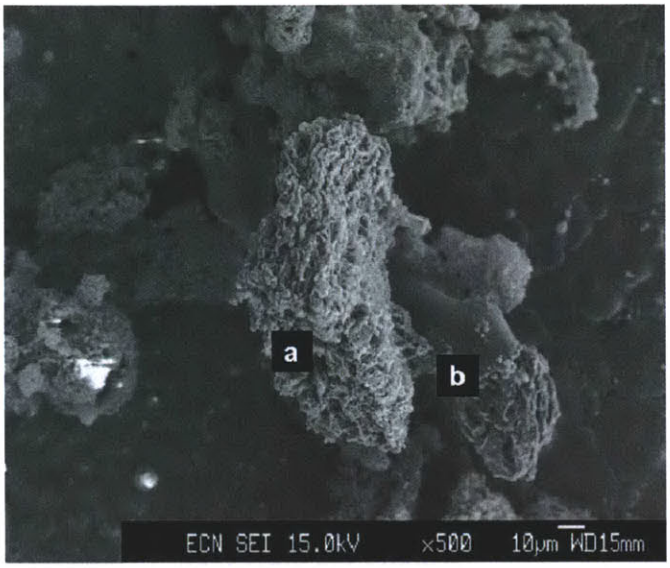

Figure 2-26. SEM image of willow ash deposit exhibiting (a) original particle structure and (b) melted area. (Coda et al. 2007)

Coda et al. (2007) also studied the ash phase composition by using a thermodynamic equilibrium model in FACTSAGE12 utilizing a model that best fit the chemical composition of wood ash. The results for beech wood ash are given in Figure 2-27 below. It is apparent that calcium oxide composes most of the solid phase and that liquid is a minority component through most of the temperature range. Other considerations are the potential for fouling by gaseous alkali compounds (K, KCl, and KOH in the temperature range of 900 to 2400 °C). In the case of willow ash, however, a higher weight fraction (45%wt) is predicted to form liquid slag at 1400 °C compared to beech (about 20%wt).

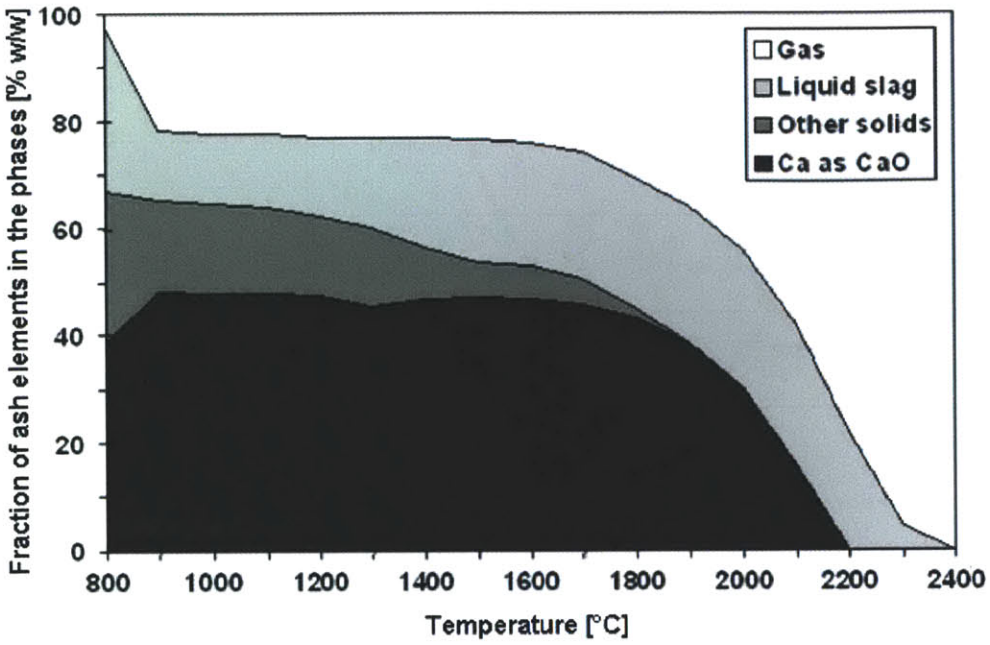

Figure 2-27. Calculated equilibrium phase distribution of beech ash under atmospheric pressure. (Coda et al. 2007)

One solution to the high solids fraction is to lower the melting temperature by adding a fluxant such as quartz (silica) or clay (silica and alumina). Coda et al. (2007) performed experiments and analyzed model calculations to find that adding silica in a molar ratio additive Si : fuel-bound Ca = 1:1 – 2:1, corresponding to 464-928 gram of quartz additive per kilogram fuel ash, is sufficient to decrease the melting point of the ash to typical operating temperature of 1400 °C. Figure 2-28 below shows the thermodynamic equilibrium predictions for ash liquid fraction with additives. The effect of quartz and clay additives is to encapsulate calcium into the Si-based and Al/Si-based matrices, respectively (Coda et al. 2007).

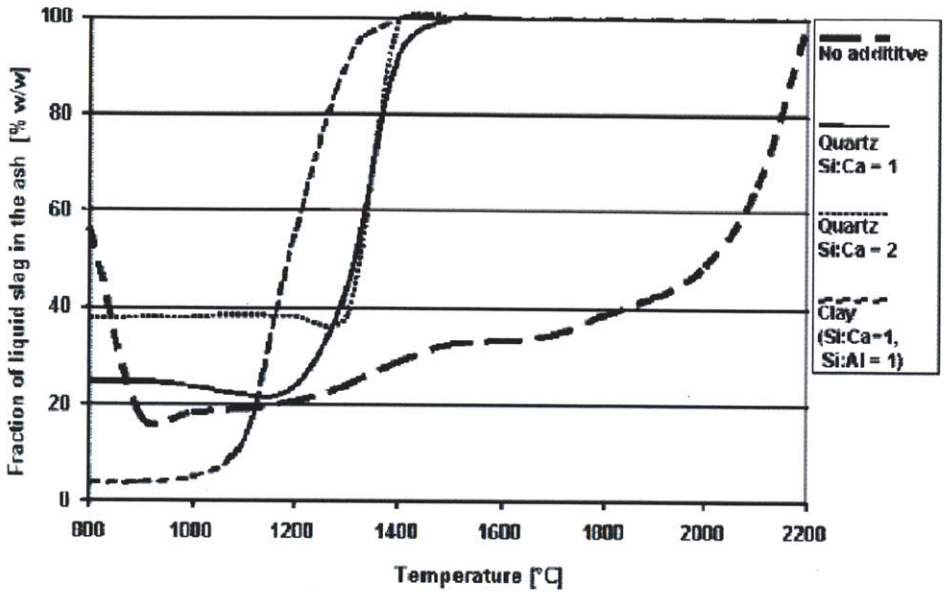

Figure 2-28. Influence of flux additives on liquid fraction for beech wood ash. (Coda et al. 2007)

Beyond determining the ash phase, the viscosity of the liquid ash is important. It is generally reported that slag viscosity should be less than 15 to 25 Pa·s, and often is typically between 8 and 15 Pa·s (J.D. Watt & F Fereday 1969). At values lower than these the flow rate is too high and a slag layer cannot build up. There are many coal ash slag viscosity correlations available but differences in the composition of biomass ash must be considered. For example, the Watt-Fereday correlation (1969) includes oxides of calcium, silicon, and aluminum but not alkali oxides. Coda et al. (2007) found that the most applicable coal model is the Urbain-Kalmanovitch model, also known as the Urbain model. It includes factors for iron, magnesium, sodium, potassium and titanium, though it does not consider phosphorus. For the beech ash composition in the study, the Urbain model predicted 0.3 Pa·s for raw wood ash and 4.3 Pa·s for wood ash with a clay fluxant at the total ratio of 2:2:1 silicon:aluminum:calcium. Both of these results indicate the liquid fraction of wood ash would flow too fast to coat the walls of a reactor.

While there is an unknown degree of error from applying a coal ash correlation to biomass ash, using the Urbain model to predict the viscosity of slag from a co-fed gasifier with coal as dominant feed would likely exhibit only a fraction of this error.

3 MODELING

3.1 EXPANSION OF ROM FOR CO-FEEDING

To simulate coal gasification, the ROM simultaneously solves a system of about 180,000 equations. They are comprised of conservation equations, correlations, kinetics mechanisms and internal variable handling. When considering modifying the ROM to handle other feedstocks like biomass, most of the original ROM equations will still apply, such as conservation equations and kinetics calculations. Many of the parameters can even be used in the same form, for example, ultimate analyses and Arrhenius kinetic parameters. However, the feedstock-specific parameters, such as activation energies and particle radii, are used in non-linear equations so they cannot be simply mass-averaged. Also, each coal-based correlation must be assessed to determine whether they are valid for biomass.

In order to expand the ROM to properly handle multiple feedstocks, all quantities representing the solid phase must be duplicated and specified or solved for each unique feedstock. These quantities are found in the input streams, the reactor blocks, connecting ports and streams, and submodels. The same applies to equations that represent the interactions between these solid phases, the gaseous phase and boundaries. The schematic below (Figure 3-1) shows some of the feedstock-specific properties that are found in both Reactors and Streams (left box) and those found only in Reactors (right box). The schematic uses coal, straw and wood as example feeds.

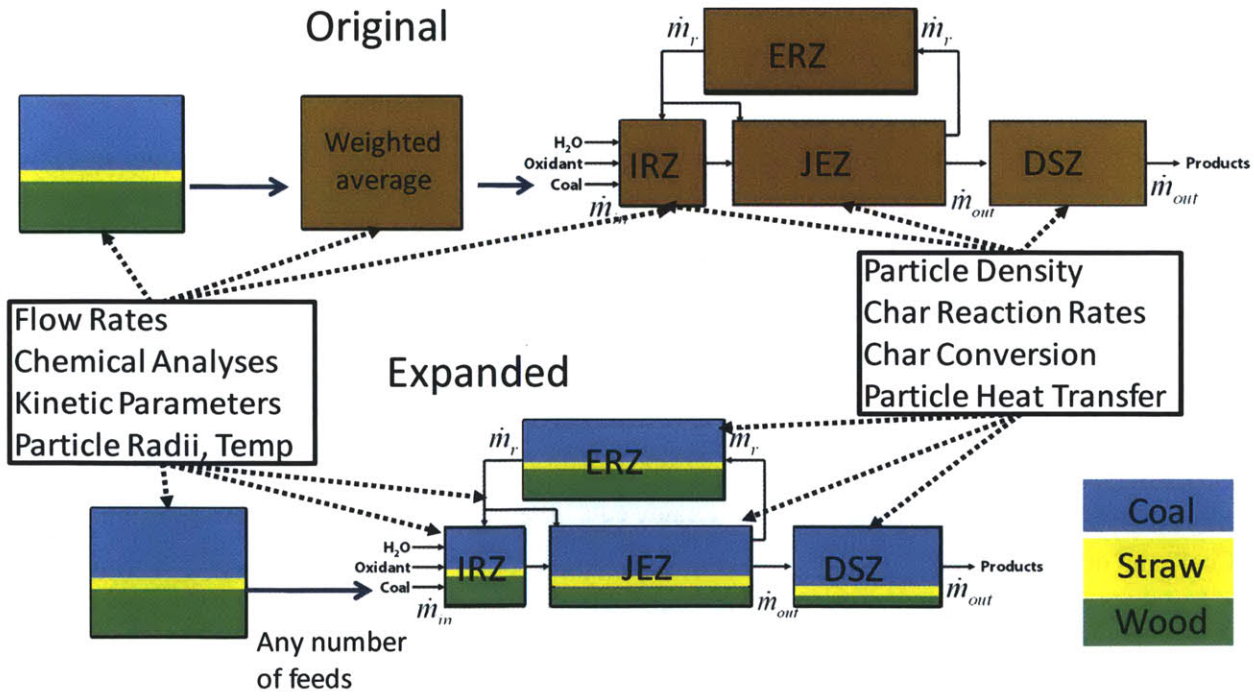

Figure 3-1. Schematic of original and expanded ROM, showing locations of feed-specific variables.

To provide maximum flexibility, this task was accomplished by turning the appropriate variables into "variable arrays" with Aspen Custom Modeler Component Sets as indices. Aspen automatically compiles equations for each Component index of an array when the array is used in a coded equation. A Component Set array can be centrally modified to add or subtract Components. This way, as the number of feeds change, variables and equations will automatically be created or deleted across the whole simulation. Also, equations and properties can be applied differently for each feedstock by looping through the index of a Component Set and implementing conditionals.

Use of Component Sets is illustrated below in Figure 3-2. In the illustration, the variable FlowRate of the CoalFeed stream is an array of type FeedList and includes values for Coal and Wood components. If a third feedstock is added, such as Straw or second type of wood, Aspen would make a third value for the FlowRate variable and every other variable that is an array of FeedList.

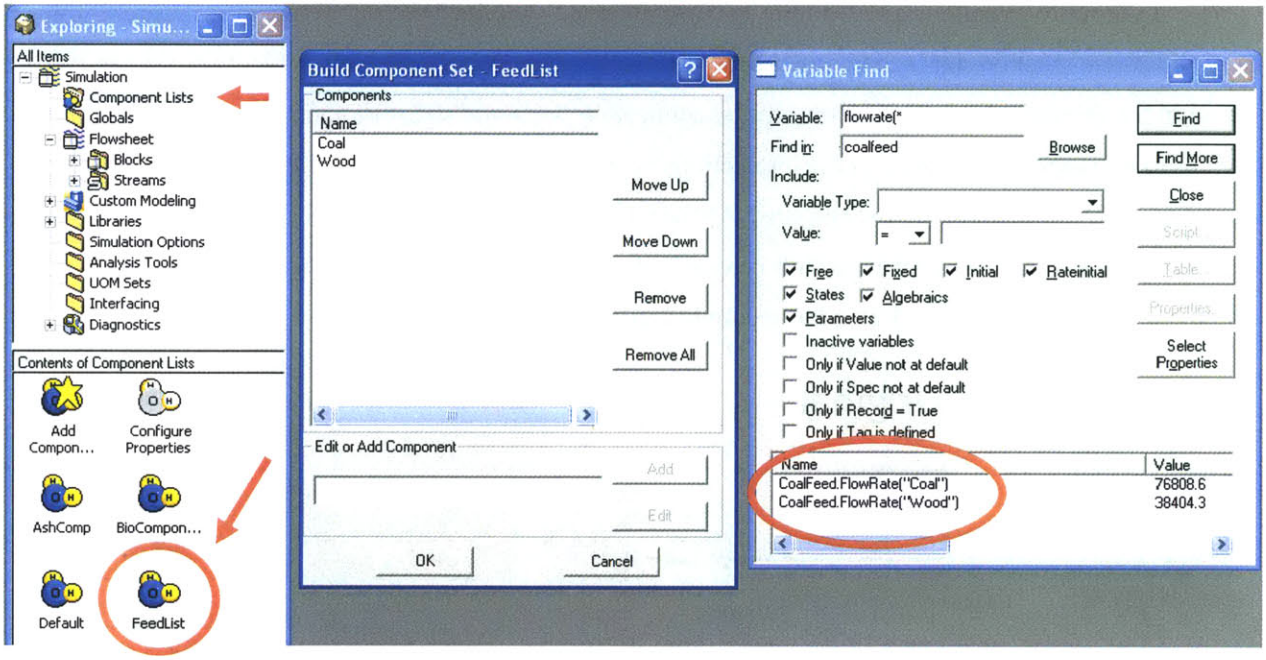

Figure 3-2. "FeedList" Component List

This idea also applies to model equations that reference variable arrays. For example, there was originally one equation that calculated the volume of a coal particle based on the given particle radius, as in Eq. 17. The expanded ROM code now shows one equation that contains variable arrays, as in Eq. 18. In compiling the code, the software creates as many equations as there are feeds (for example, one for "Coal" and one for "Wood").

Eq. 17 $$Vchar = \frac{4}{3}\pi * ParticleRadius^3$$

Eq. 18 $$Vchar(FeedList) = \frac{4}{3}\pi * ParticleRadius(FeedList)^3$$

3.2 CONTINUITY EQUATIONS

The continuity equations, which represent interactions between phases, were also modified during the expansion. All equations that are used to find particle-specific quantities, such as control-volume energy balance between gas and particles that is used to solve for particle temperature (Eq. 19) will be expanded the way particle volume equation was expanded in the example above. Note that there is an index for the particle, k, because the creation of multiple equations was done explicitly by nesting the equation in a For loop. On the other hand, equations that are used to find the gas phase properties, such as temperature (Eq. 20), will sum the particle contributions, such as convection (shown) and radiation.

Eq. 19

$$H_{Particle(k),Out} - H_{Particle(k),In} = -h_{particlegas}(k) * (Tp(k) - T) + Other\ Contributions$$

Eq. 20

$$H_{Gas,Out} - H_{Gas,In} = \sum_{k}^{FeedList} h_{particlegas}(k) * (Tp(k) - T) + Other\ Contributions$$

In the equations above, H represents volumetric enthalpy and h is the convection heat transfer coefficient between particles (computed for each feedstock) and gas. Other contributions to the particle energy balance include drying, devolatilization, heterogeneous reactions, radiation between particle and wall, radiation between particles (assumed only between particles of the same feedstock), and enthalpy lost to slag deposition. Other contributions to the gas balance include drying, devolatilization, heterogeneous reactions, and convection between wall and gas. Note that homogenous reaction contributions are accounted for in the enthalpy in/out terms.

Mass and momentum equations for particles and gas phase are likewise expanded.

3.3 COAL DEVOLATILIZATION IN ROM

The Reduced Order Model represents the devolatilization of coal using Merrick's model (1983) to predict the yields. Coal has a relatively small amount of volatile matter and the process is extremely fast compared to char conversion time. Because of convergence issues in the ROM when Arrhenius devolatilization rates were used, the model assumes the process occurs at a rate determined by the residence time of the particles in the Internal Recirculation Zone (IRZ).

Merrick's model for devolatilization prescribes that raw coal, coal char, and a lumped tar are each molecules in the form of $C_\alpha H_\beta O_\gamma N_\delta S_\varepsilon$. Merrick also suggests values for the subscripts. Besides char and tar, the devolatilization products include CO_2, CO, H_2, H_2O, CH_4, C_2H_6, NH_3 and SO_2. The yield of each product is determined through a combination of elemental balances (one for each element) and five correlations. This is presented in matrix form in Figure 3-3 below.

$$\begin{bmatrix} 0.98 & 0.75 & 0.8 & 0.4286 & 0.2727 & 0.85 & 0 & 0 & 0 & 0 \\ 0.002 & 0.25 & 0.2 & 0 & 0 & 0.082 & 1 & 0.1111 & 0.1765 & 0.0588 \\ 0.002 & 0 & 0 & 0.5714 & 0.7273 & 0.049 & 0 & 0.8889 & 0 & 0 \\ 0.01 & 0 & 0 & 0 & 0 & 0.009 & 0 & 0 & 0.8235 & 0 \\ 0.006 & 0 & 0 & 0 & 0 & 0.01 & 0 & 0 & 0 & 0.9412 \\ 1 & 0 & 0 & 0 & 0 & 0 & 0 & 0 & 0 & 0 \\ 0 & 1 & 0 & 0 & 0 & 0 & 0 & 0 & 0 & 0 \\ 0 & 0 & 1 & 0 & 0 & 0 & 0 & 0 & 0 & 0 \\ 0 & 0 & 0 & 1 & 0 & 0 & 0 & 0 & 0 & 0 \\ 0 & 0 & 0 & 0 & 1 & 0 & 0 & 0 & 0 & 0 \end{bmatrix} \cdot \begin{bmatrix} X_{dev,Char} \\ X_{dev,CH_4} \\ X_{dev,C_2H_6} \\ X_{dev,CO} \\ X_{dev,CO_2} \\ X_{dev,Tar} \\ X_{dev,H_2} \\ X_{dev,H_2O} \\ X_{dev,NH_3} \\ X_{dev,H_2S} \end{bmatrix} = \begin{bmatrix} X_{daf,C,0} \\ X_{daf,H,0} \\ X_{daf,O,0} \\ X_{daf,N,0} \\ X_{daf,S,0} \\ 1-Y_{VM,daf,act} \\ 1.31X_{daf,H,0} \\ 0.22X_{daf,H,0} \\ 0.32X_{daf,O,0} \\ 0.15X_{daf,O,0} \end{bmatrix}$$

Figure 3-3. Coal Devolatilization yield prediction matrix

The right hand side is populated with the feed's dry, ash-free ultimate analysis and one other quantity, the "actual volatile yield." The actual volatile yield is a non-linear calculation based on the proximate analysis. The expression is $Y_{daf,VM,act} = X_{daf,VM,0} - 0.36X_{daf,VM,0}^2$.

The ROM assumes coal tar is similar in nature to benzene (C6H6), and thus it computes the tar thermodynamic properties (density, heat of formation and specific heat) by scaling the respective properties of benzene by the ratio of molecular weights. Unfortunately, since the composition of tar is given only in mass fractions, the molecular weight cannot be found. The equivalent atomic weight is therefore used (roughly equal to 6.4 kg/kmol). The effect of this is large in terms of property values but the effect on the system outputs has not been investigated.

When considering applying Merrick's model to biomass, the elemental balance is still valid but the correlations are not. This is quickly found as using typical ultimate analyses results in negative yield quantities. Negative quantities are found even after changing the char and/or tar composition. No analogous set of correlations exist for biomass devolatilization. Therefore, it is necessary to consider a whole new method of predicting volatile yields for biomass.

3.4 Representing Biomass Volatile Yields in ROM

Several methods of predicting volatile yield rate and composition were presented in the literature review. Based on the need for detailed gas, tar and char composition predictions, the method published by Ranzi et al. (2008) was selected for use in the ROM. This method provides yield predictions of the three components of biomass (cellulose, hemicellulose and tar) so that a variety of biomass types can be represented by changing the component composition. A new Component Set, BioComponents, and a variable array using it, BioComposition(BioComponents,FeedList), have been added to the ROM.

Like many multi-step biomass devolatilization models, the reactions and reaction rates presented in Ranzi can be arranged as a system of Differential Algebraic Equations (DAE's). It can then be solved numerically using Matlab if a temperature profile is supplied. This a priori solution is then plugged into the ROM. A simple, linear temperature profile (heating rate of 1000 K/s) has been proposed based on the conditions of coal EFG. The temperature starts at 100 °C and reaches 900 °C, which is close to the maximum temperature experienced in the IRZ, the reactor node in which devolatilization is assumed to start and reach completion. Based on the Ranzi model all devolatilization reactions are complete well before 900 °C. The simulated output for the devolatilization of cellulose is presented in Figure 3-4 below. There are similar output plots for hemicellulose and lignin. Note that Char is represented as pure carbon in this model. In the ROM, wood char is represented as this pure carbon and the original ash content. HAA is hydroxyl-acetaldehyde ($C_2H_4O_2$), HMFU is 5-hydroxymethyl-furfural ($C_6H_6O_3$) and LVG is levoglucosan ($C_6H_{10}O_5$).

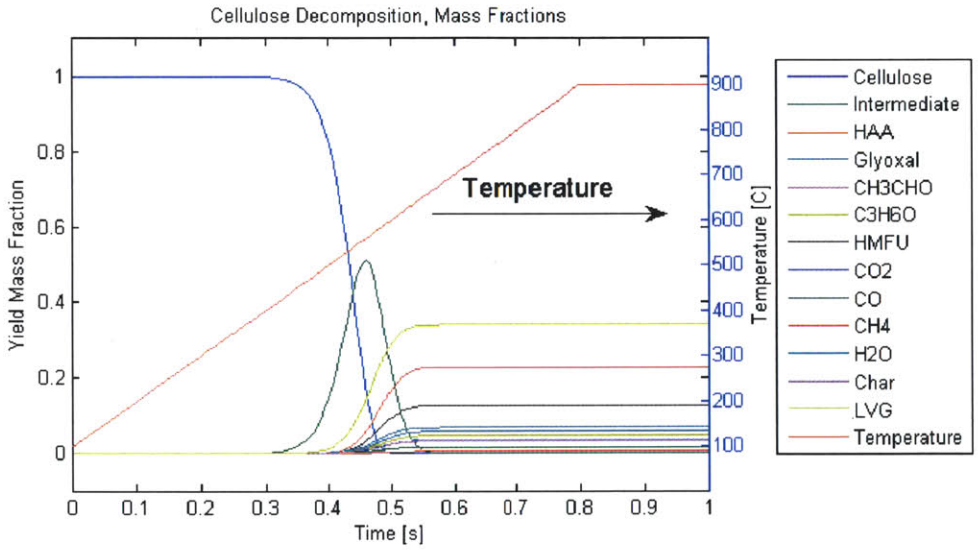

Figure 3-4. Cellulose Decomposition output.

At the hypothesized heating rate and temperatures, the reactions are complete within a fraction of a second. Since the residence time of particles in the Internal Recirculation Zone (IRZ) is about one second, the assumption that the devolatilization process starts and ends in the IRZ is valid.

As mentioned earlier, the primary decomposition model has 42 species and 18 equations. The mechanism provides more detail than the ROM can reasonably use but it is easier to simplify details than to do the reverse. This simplification is done by lumping the predicted hydrocarbons not already present in the ROM, into pseudo tar compounds for each bio component. In other words, each of the three proposed tar components is a mole-weighted average of predicted tars. Sample calculations for cellulose tar ($C_{3.39}H_{5.49}O_{2.60}$) are presented below in Table 3-1. The composition of tars from hemicellulose and lignin are $C_{1.16}H_{3.05}O_{1.03}$ and $C_{2.98}H_{5.45}O_{1.19}$, respectively.

Table 3-1. Sample calculation for lumping of cellulose tars. Gas, water and char products not shown.

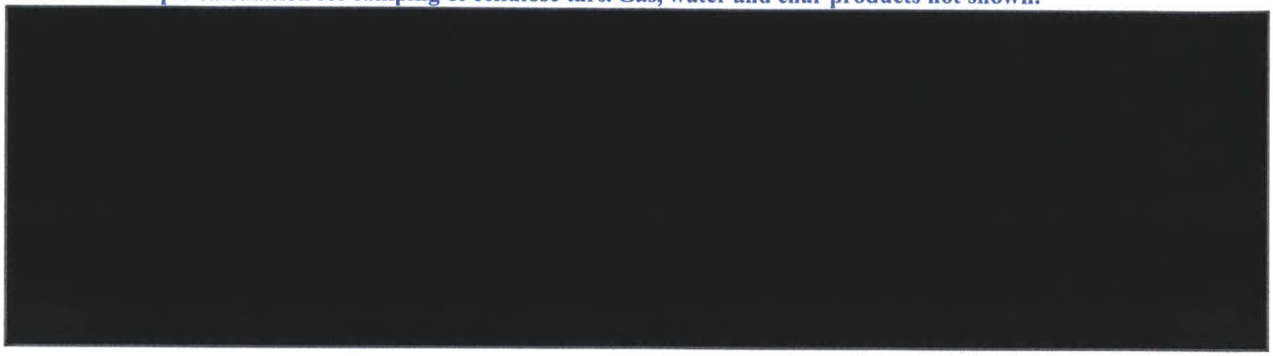

As mentioned, the ROM computes the thermodynamic properties of coal tar by scaling the respective properties of benzene by the ratio of molecular weights. This approach was replicated for each biomass tar.

3.5 Ultimate and Proximate Analysis

The wood ash fraction used in the ROM model is an average of values from the literature, including rule-of-thumb figures. The ash breakdown was taken from the wood chip ash analysis in Senneca et al. (2007). This is given in Table 3-4. Two values of free moisture content were used in the modeling. First, a field-dried value of 10% was taken from rule-of-thumb. Second, a raw-wood value of 35% was taken from Senneca et al. (2007).

Because of the nature of the devolatilization mechanism, the original feedstock composition must be a linear combination of the 3 bio-components. An arbitrary ultimate and proximate analysis cannot be used. The assumed chemical compositions of the cellulose and hemicellulose bio-components are described in Ranzi et al. Lignin is further broken down into three types, each with explicit chemical compositions (see Appendix A.1 Determining Lignin Composition). It is possible to compute the composition in terms of bio-components if given the ultimate composition, if the ultimate composition is within the right bounds. While the paper gave typical overall chemical composition and bio-component breakdowns for softwood and hardwood, the paper did not provide the relative amounts of the three lignin types. Also, there is no positive linear combination of the three lignin types that would fit the given bio-component breakdowns and overall compositions. This is shown in Appendix A.1. For the purpose of this modeling study, a lignin breakdown was assumed (80% Lig-H, 20% Lig-C), the softwood bio-component composition was borrowed from Ranzi, and the ultimate analysis was then calculated. In this way, an atom balance is ensured. The volatile matter and fixed carbon parts of the proximate analysis come from the predicted volatile and char yields.

3.6 Biomass Char Kinetics Data Selection

As discussed in the literature review, the rate of conversion of biomass char via combustion and gasification can be given on an intrinsic or extrinsic basis, though extrinsic reactivity data is much easier to find. Di Blasi (2009) provides a compilation of reactivity data expressions and parameters for steam gasification, carbon dioxide gasification and combustion. Kinetics data was selected for use in the ROM from these compilations based on how closely the pyrolysis conditions and gasification conditions matched the expected conditions of EFG. These conditions include small diameter particles, high-temperature flash pyrolysis, and then high temperature, high pressure gasification. The selections and the respective conditions are given below in Table 3-2. The conditions do not fully match the specifications, primarily due to low pressure reactants. Several other sources were considered but were discounted due to lack of validation or because they were not better at matching condition specifications.

Table 3-2. Biomass char reactivity data selection

Conversion type	Source [Di Blasi Ref #]	Feedstock	Pyrolysis Conditions	Gasification Conditions
CO_2 Gasification	(Risnes et al. 2008) [120]	Spruce, 60 μm char	Pressurized Drop Tube Furnace (DTF)	700-1000 °C, P_{CO2}=3-101kPa
H_2O Gasification	(Hemmati & Laguerie 1988) [131]	Sawdust	Slow, 650-1000 °C	350-1000 °C, P_{H2O}=21-100kPa
O_2 Combustion	(Janse et al. 1998) [134]	Pine	Fast, 300K/s to 600 °C	300-500 °C, in 2.25-36%vol O2 in N2

3.7 Overall Modeling Picture

The modeling structure of the ROM is illustrated in Figure 3-5. The blue callouts show where there are now parallel models to handle parallel feed streams.

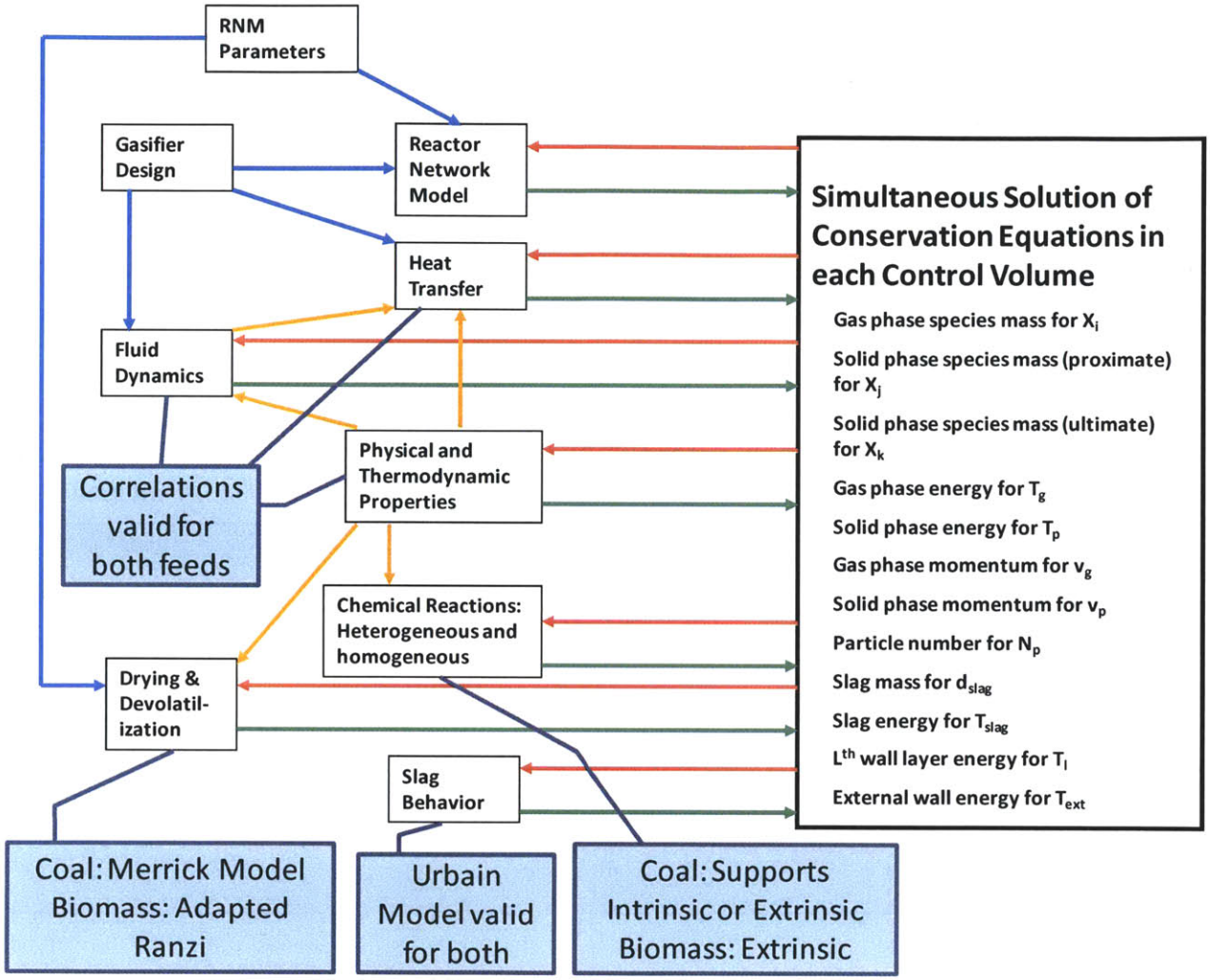

Figure 3-5. Model flow diagram with description of co-feeding expansion.

3.8 Results

The primary goal of the co-feeding EFG ROM simulation is to evaluate the qualitative and quantitative effects of partially displacing coal feed with woody biomass. This section looks at several outputs of the expanded GE 2700tpd gasifier simulation as functions of wood input mass fraction, while keeping the total feed mass constant. In the first several sub-sections, the oxygen input is also held constant. In the final two sub-sections, oxygen is reduced to account for less total fixed carbon input.

The output data and plots were generated in ACM using the Dynamic mode along with the Task feature. A Task is a script that runs during dynamic simulations and can initiate a Ramp function. The Ramp function takes a single fixed variable and linearly ramps it to some explicit or computed value over

an explicit or computed simulation-time duration (.01%-33% wood fraction over 2 simulation hours). Many Ramp functions can be defined in a Task and can be made to run simultaneously if specified within Parallel/Endparallel statements. In this way, important outputs can be captured while the input of wood is ramped up and coal is ramped down.

After a task is created, Plot/Table forms are created before running in Dynamic mode to record specific variables. These forms can be set to display the data against any other variable. For example, a free variable "BioInputFraction" was created to continuously keep track of the mass fraction of wood input. This variable is then used as the x-axis of many plot forms.

3.8.1 *Implemented Biomass Devolatilization Model and Chemical Composition*

The following are the results of introducing a wood fraction with wood devolatilization yield prediction and Ultimate, Proximate and Ash compositions. To analyze the effect of each biomass model, all other parameters (kinetics) and models were initially kept the same as those for coal. Coal and Wood composition values are given below in Table 3-3 and 7, respectively.

Table 3-3. Coal Analysis – High-sulfur bituminous coal, Illinois No. 6.

Ultimate	Ash	Moisture	C	H	O	N	S
	.0971167	.100991	.569182	.0467886	.156406	.0099866	.0175285
Proximate	Ash	Moisture	Fixed C	Volatiles			
	.0971167	.100991	.341864	.460028			
Ash	Al2O3	CaO	Fe2O3	K2O	MgO	MnO	Na2O
	.153758	.251248	.147339	.066064	.016676	1.91e-4	.001148
	P2O5	SiO2	SO3	TiO2			
	.011362	.409452	.0543598	.008376			

Table 3-4. Low-moisture Wood Analysis.

Ultimate	Ash	Moisture	C	H	O	N	S
	.03	.10	.440962	.053978	.375076	-	-
Proximate	Ash	Moisture	Fixed C	Volatiles			
	.03	.10	.137666	.732334			
Ash	Al2O3	CaO	Fe2O3	K2O	MgO	MnO	Na2O
	.091	.153	.035	.128	.034	-	.019
	P2O5	SiO2	SO3	TiO2			
	-	.45	-	-			

Figure 3-6 below shows the rate of generation of syngas, H_2O and CO_2 from devolatilization and drying processes, only. Because such a large fraction of wood leaves as volatiles during heating, the contribution of syngas and CO_2 from volatile creation increases as wood input increases. Since the moisture content of wood was kept low, approximating dried wood, and because coal creates a significant fraction of water during devolatilization, the H_2O yield decreases as wood input increases. Figure 3-6

shows that the IRZ exit temperature is brought down by the slightly endothermic devolatilization reaction. It is believed to be endothermic because of the high chemical value of gases leaving the low-valued feed.

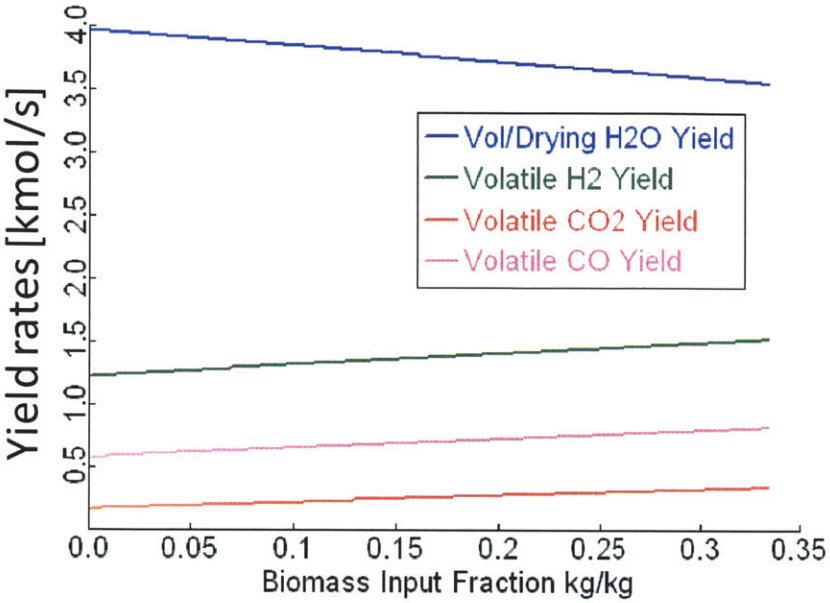

Figure 3-6. Global Volatile yield rates [kmol/s] as functions of Wood Input.

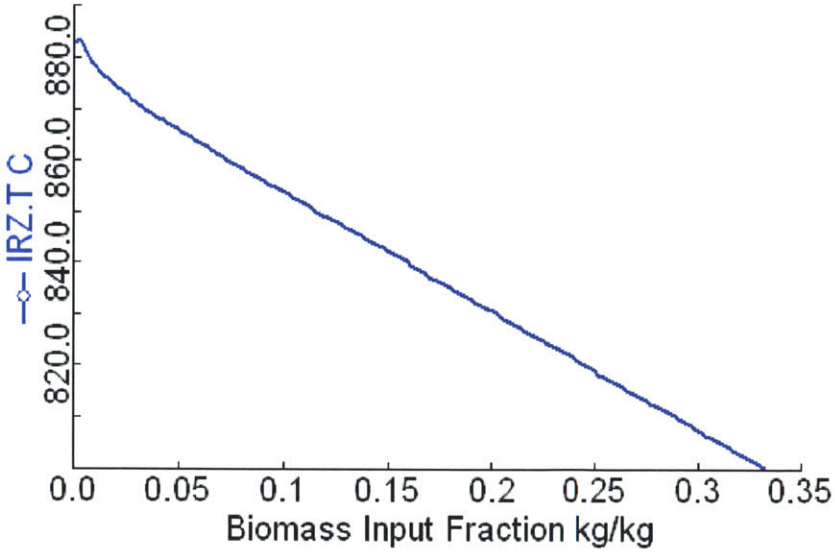

Figure 3-7. Exit gas temperature of IRZ Reactor as function of Wood Fraction.

As the ratio of wood input increases, the amount of oxygen in the feed increases. Since the oxygen feed stream remains constant in early simulations, the oxygen-fuel ratio increases and more char is combusted as opposed to gasified. This increases the overall temperature, as shown in the JEZ temperature profile plot in Figure 3-8 below. This figure also shows that the peak temperature decreases

with increasing wood, and this point is further illustrated in Figure 3-9 below. This decrease in maximum temperature is the result of lower upstream temperature (IRZ exit temperature).

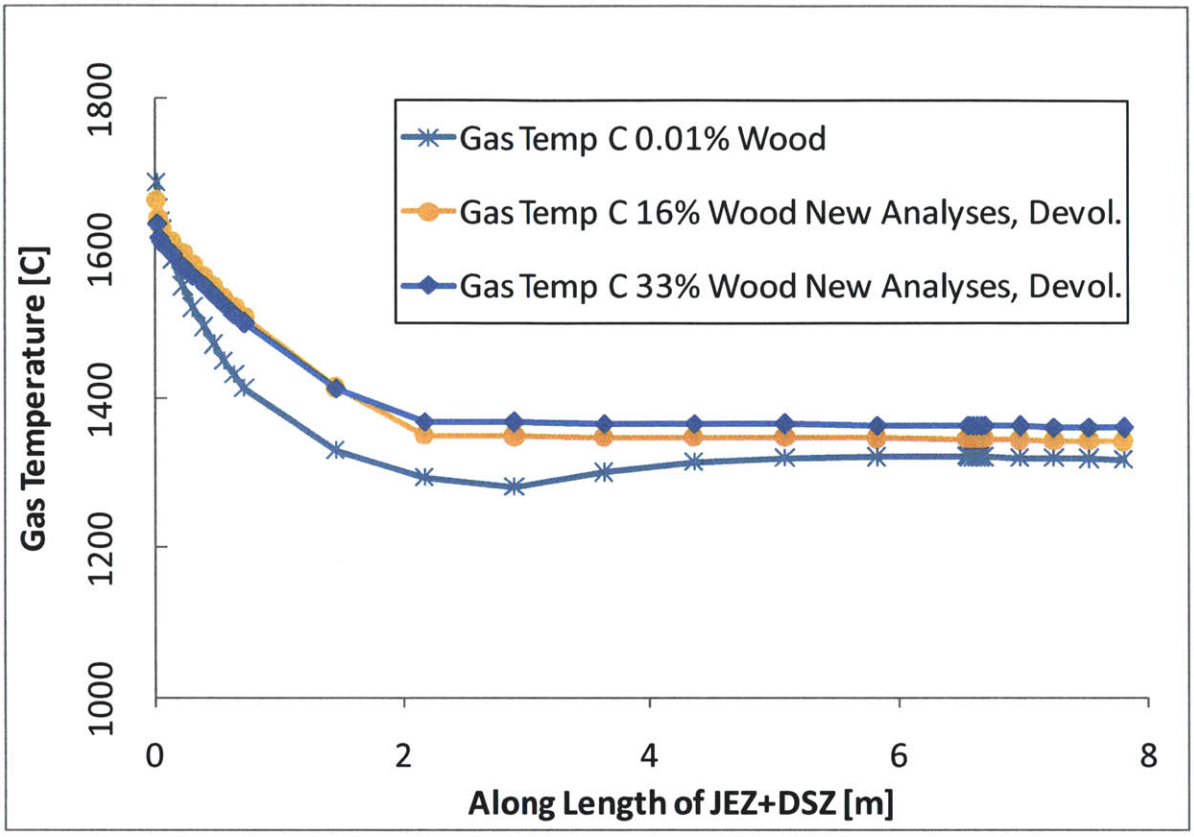

Figure 3-8. Temperature profiles along JEZ at different percentages of Wood Input.

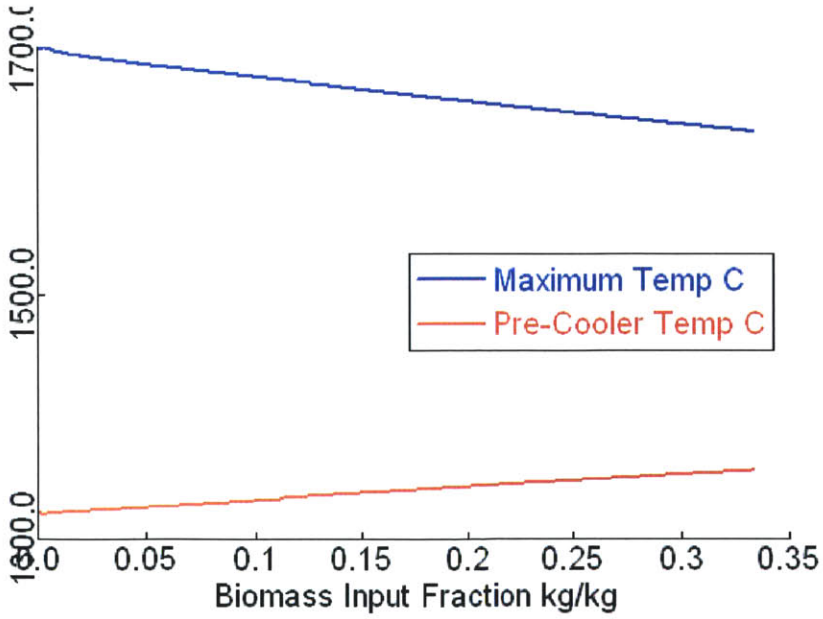

Figure 3-9. Gas Temperatures: Maximum and before entering cooler.

The rate of conversion of char to CO, CO_2 and H_2O is greater with increasing wood fraction as a direct result of the increase in temperature. This trend is clear in the plot of carbon conversion profiles along the JEZ, in Figure 3-10. The equation that computes carbon conversion in control volume "*i*" is given below in Eq. 21.

Eq. 21 $$(Conversion)_i = 1 - \frac{m_{particle,i} \times prox_{FixedCarbon,i}}{m_{particle,0} \times prox_{FixedCarbon,0}}$$

In the equation above, m is the mass of a char particle and $prox_{FixedCarbon}$ is the fraction of a particle that is able to be converted.

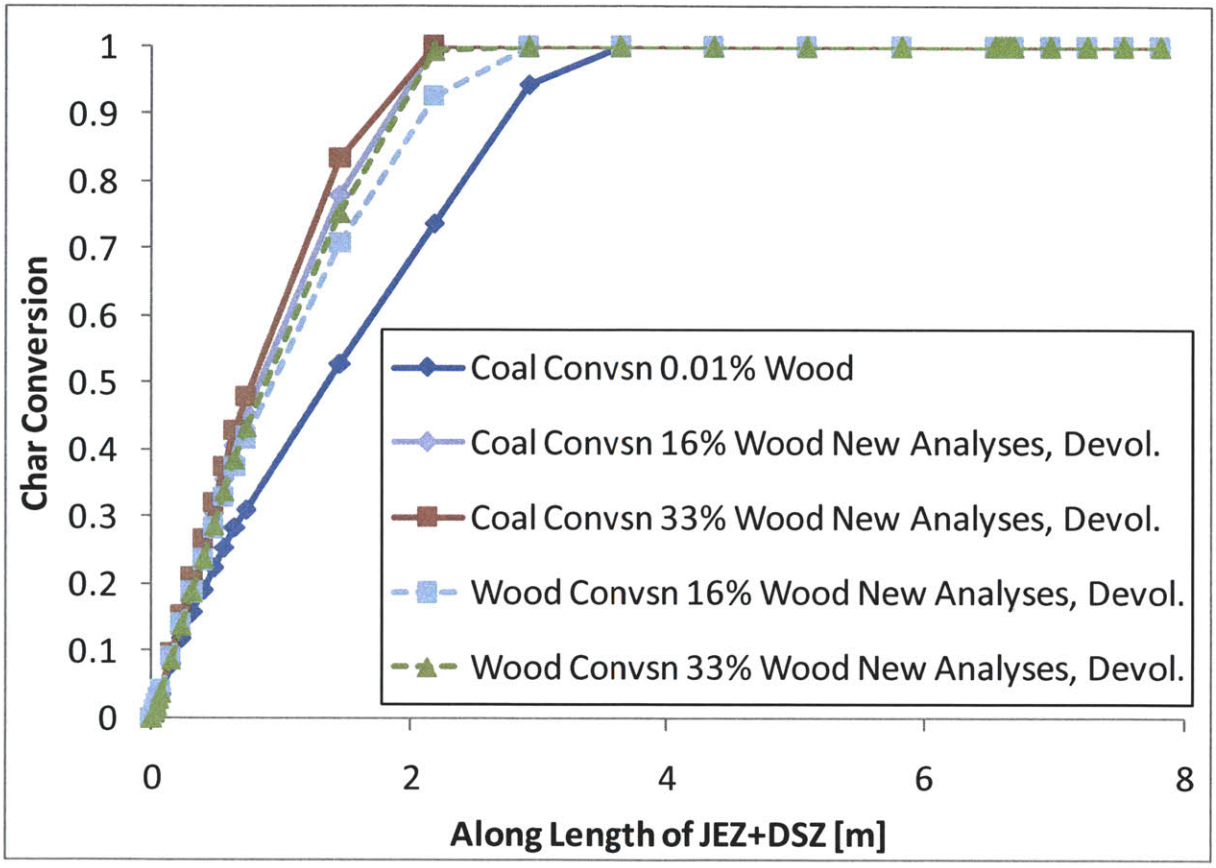

Figure 3-10. Conversion profiles along JEZ at different percentages of Wood Input.

Figure 3-11 shows the state of the ash slag at the end of the wall of the Down Stream Zone (DSZ), the last reactor before the cooler. As the gas temperature in the JEZ and DSZ increases, the slag temperature increases. This increase in temperature alone is responsible for a 26% decrease in viscosity. The change in ash composition (Figure 3-12) brings the change up by 2 percentage points (total drop is only 24%). The overall decrease in slag viscosity and the decrease in total ash content both contribute to a decrease in slag thickness of about 13.5%.

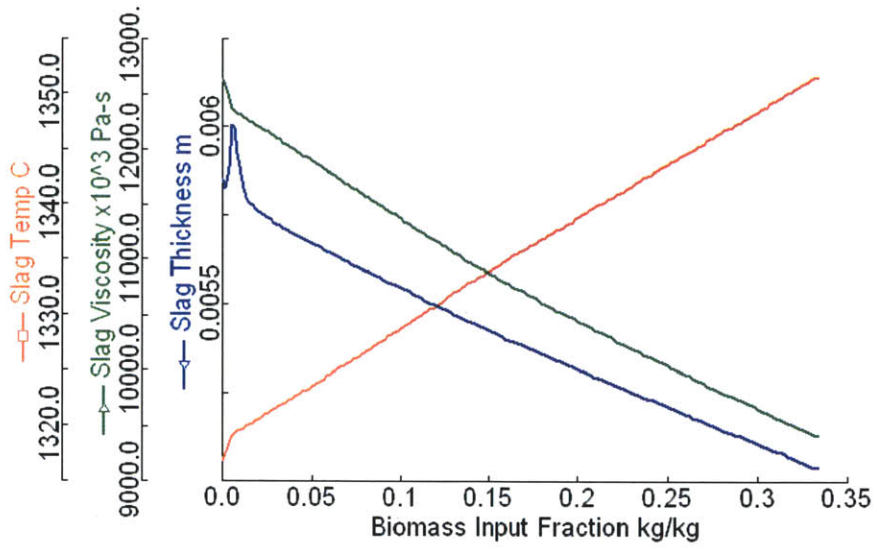

Figure 3-11. Slag State as function of Wood Input.

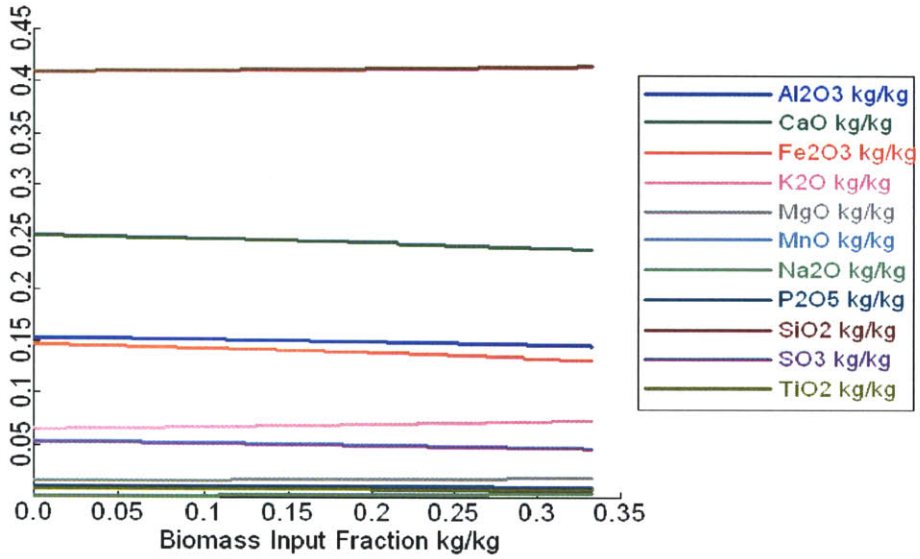

Figure 3-12. Weighted Ash composition (kg Mineral/kg Ash) as function of Wood Input.

Figure 3-13 shows that as the fraction of wood input increases, both the heating value of the syngas and the Cold Gas Efficiency (CGE, on HHV basis) decrease monotonically. The syngas heating value decreases 18% because the total input heating value decreases (due to increased oxygen content and less carbon), and CGE decreases 13% because there is an increase in the amount of char that is combusted rather than gasified. In other words, while Syngas heating value is expected to fall with decreased input heating value, CGE will not fall, since it is a ratio of syngas value to input value. Instead, it falls because, as mentioned earlier, the high oxygen content of the feed causes the oxygen-fuel ratio to rise and combustion to increase, resulting in a more-than-proportional increase in CO_2 and H_2O. This is exhibited in Figure 3-14 below.

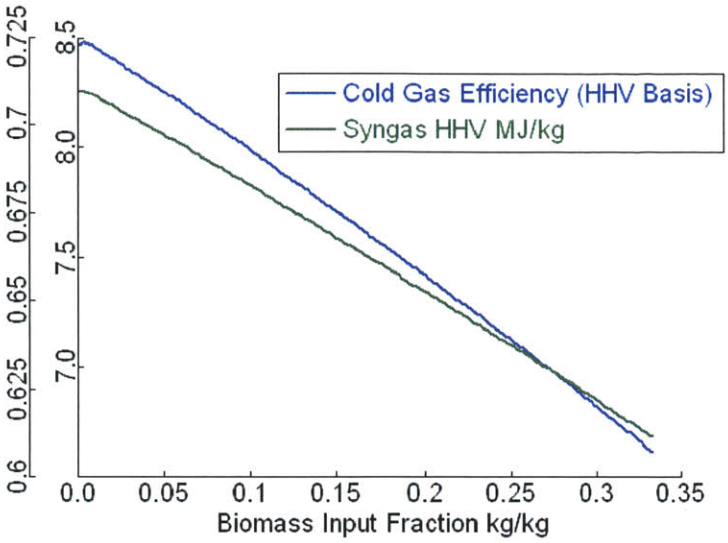

Figure 3-13. CGE and Syngas HHV as functions of Wood Input.

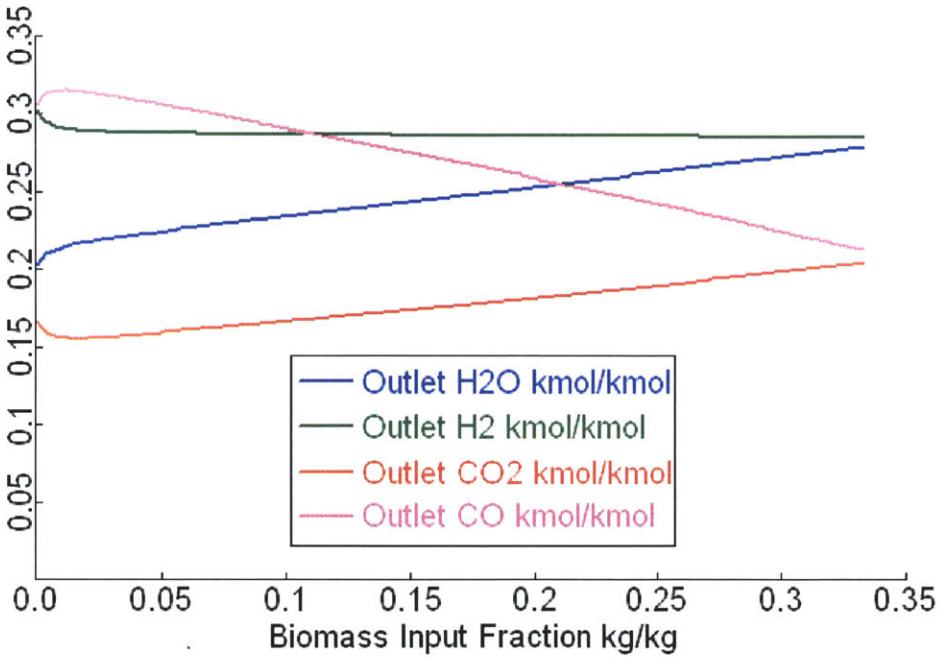

Figure 3-14. Syngas Composition after Cooler as function of Wood Input.

The curves at the lower end of the syngas composition curves (Figure 3-14) require further explanation. They appear in the composition only in the Cooler reactor (which applies both radiant and quench cooling), i.e. the composition curves in all previous reactors are completely linear. The difference arises because the Cooler implements a different Water Gas Shift (WGS) reaction mechanism and kinetics. The Cooler uses the kinetic expression and parameters developed by Bustamante et al. (2005). The rest of the Reactor Network uses the WGS from the hydrocarbon oxidation scheme of Westbrook (1981) and Jones (1988).

3.8.2 *Implemented Biomass Char Kinetics*

The selection of wood-specific char reactivity expressions was discussed in section 3.6, Biomass Char Kinetics Data Selection. The selections include chemical kinetic terms (functions of temperature and pressure) and empirical structural terms (functions of conversion) and reflect the higher reactivity of wood char. The results presented up to this point were obtained with the coal kinetics expressions and parameters. The following results show the impact of implementing the wood reactivity expressions and parameters. There were significant changes to the conversion profiles, only slight changes to the temperature profiles and no numerical change in CGE.

The wood particle conversion profile is considerably faster with the new kinetics (Figure 3-16, comparing this case to the previous case and the base case). However, since wood produces a small fraction of char and it is a small fraction of the total input, the quicker-reacting wood char does not have much effect on the temperature profile (Figure 3-15, again comparing this case to the previous case and the base case). Thus, the conversion profile of coal is very close to what it was before the biomass char kinetics implementation. For the same reason, the syngas composition and CGE do not change much either (Figure 3-17) – both cases result in values of 60.9% CGE and 6.70 MJ/kg HHV with 33% wood input. The CGE and Syngas HHV are compared for all cases in the Analysis section in Figures 3-33 through 3-35.

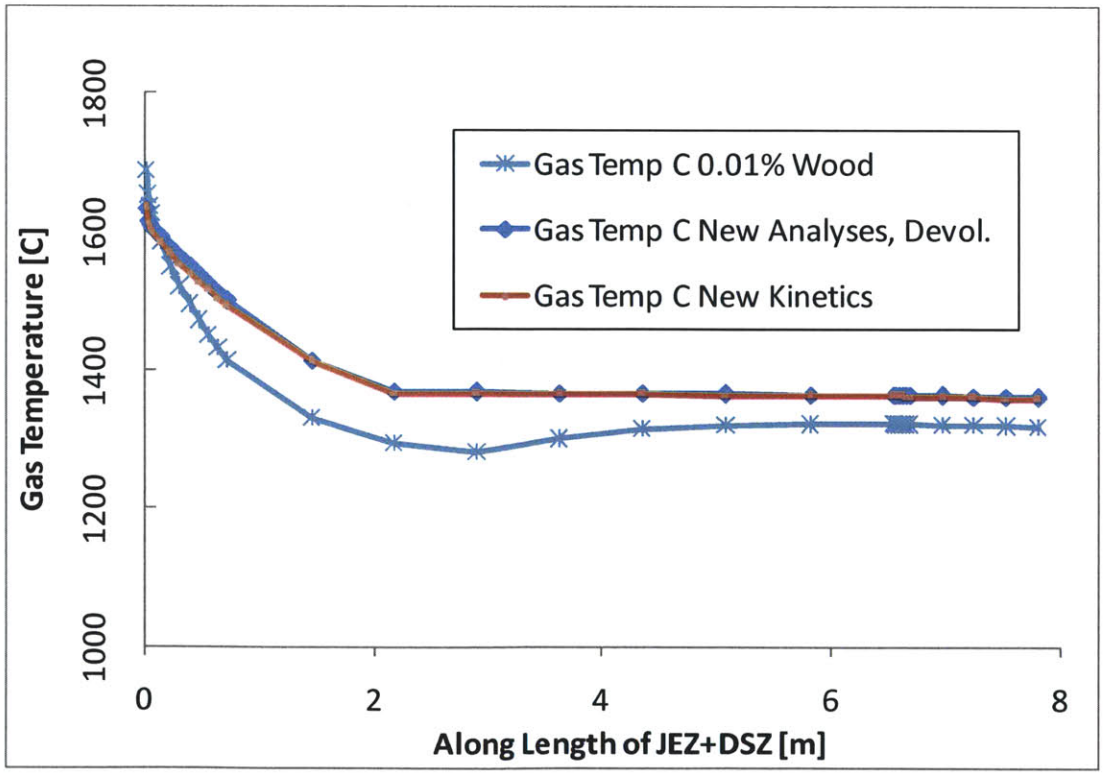

Figure 3-15. Temperature profiles along JEZ and DSZ reactors: Reference (coal only), new analyses/devolatilization, and biomass char kinetics (33% wood).

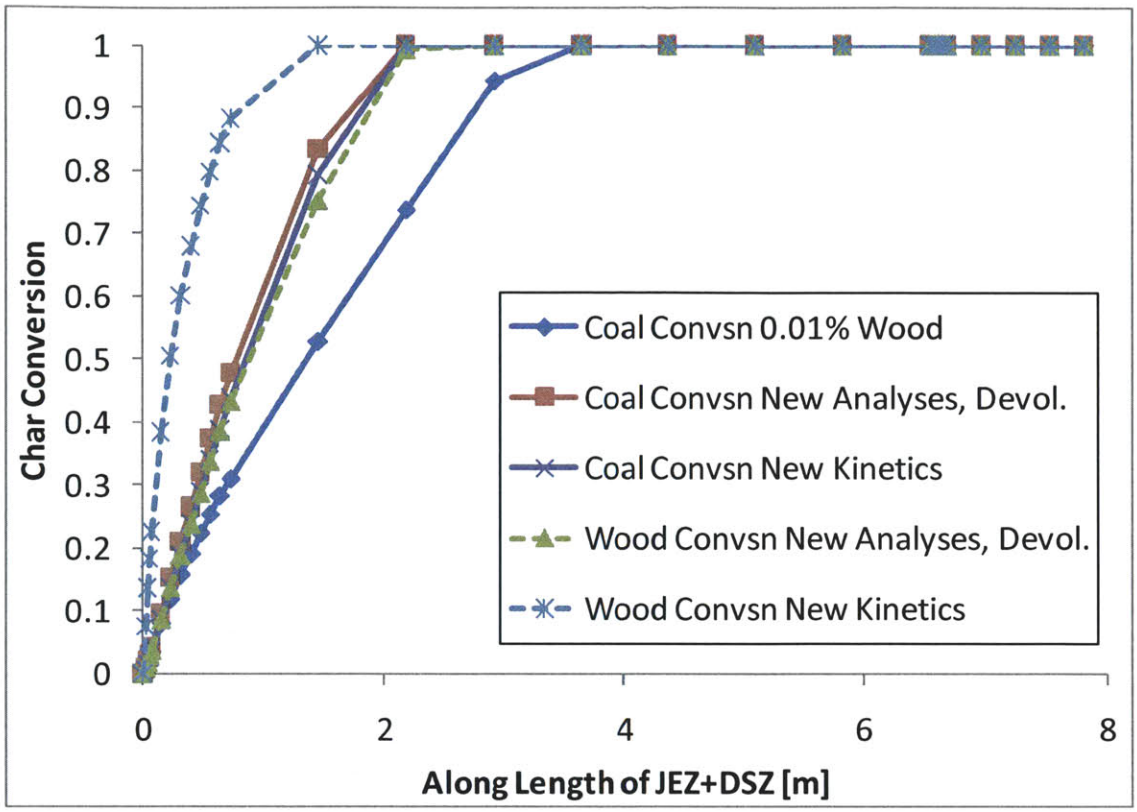

Figure 3-16. Conversion profiles along JEZ and DSZ reactors: Reference (coal only), new analyses/devolatilization, and biomass char kinetics (33% wood).

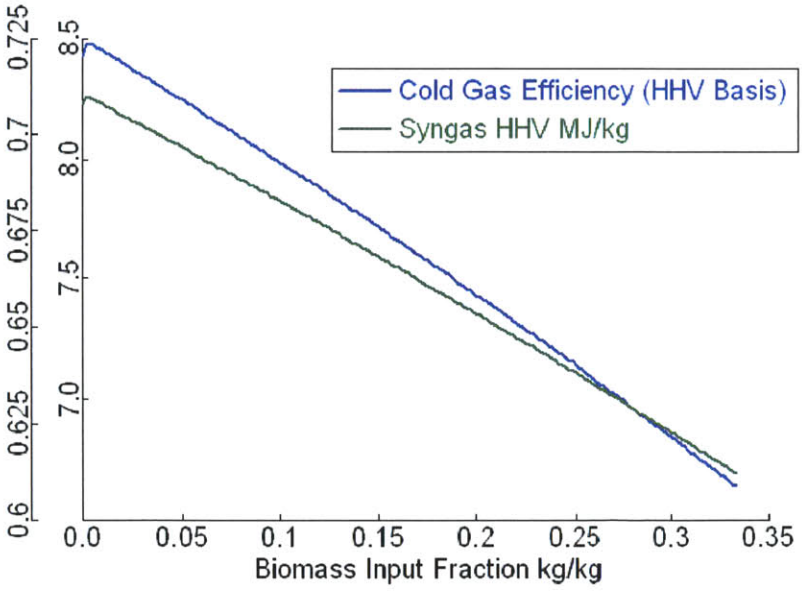

Figure 3-17. CGE and Syngas HHV as functions of Wood Fraction with Biomass Char Kinetics.

3.8.3 *Increased Moisture Content to Raw Wood Level*

In order to understand the effect of co-feeding raw, high-moisture raw wood, the moisture content of the wood input was increased from 10 to 35%. Ash content was held constant at 3%, while the respective balances of Ultimate and Proximate analyses were scaled down linearly (Table 3-5).

Table 3-5. High-moisture Wood Analysis.

Ultimate	Ash	Moisture	C	H	O	N	S
	.03	.35	.314243	.038466	.267291	-	-
Proximate	Ash	Moisture	Fixed C	Volatiles			
	.03	.35	.0981072	.5218929			

As expected, the yield of H_2O from drying and devolatilization now increases with wood fraction, as seen in Figure 3-18 below. Also, since the moisture fraction of the biomass displaces the volatile matter fraction, there is a less strong increase of the other volatile yields. Since devolatilization resulted in a temperature drop, this change smoothes out the drop in IRZ Exit temperature as a function of wood input fraction (Figure 3-19), so the value at 1/3 wood input fraction is 860 °C instead of 800 °C. This higher IRZ Exit temperature affects the JEZ Temperature Profile plots (Figure 3-20) across the range of input fractions, causing an unexpected rise in overall temperature. Conversion rates are likewise increased (Figure 3-21).

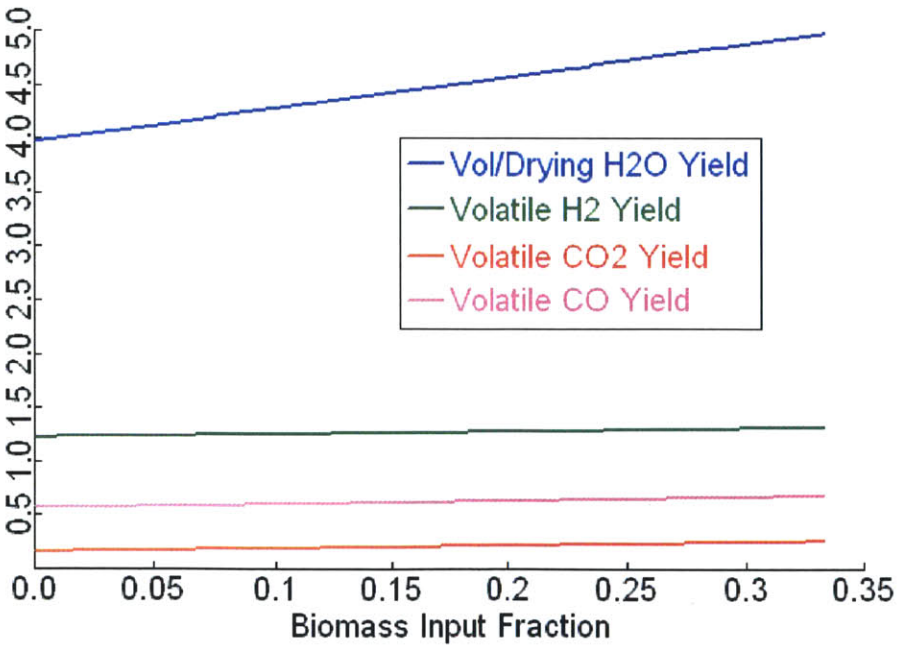

Figure 3-18. Global Volatile yield rates [kmol/s] as functions of Wood Input with Biomass Kinetics and increased Moisture Content.

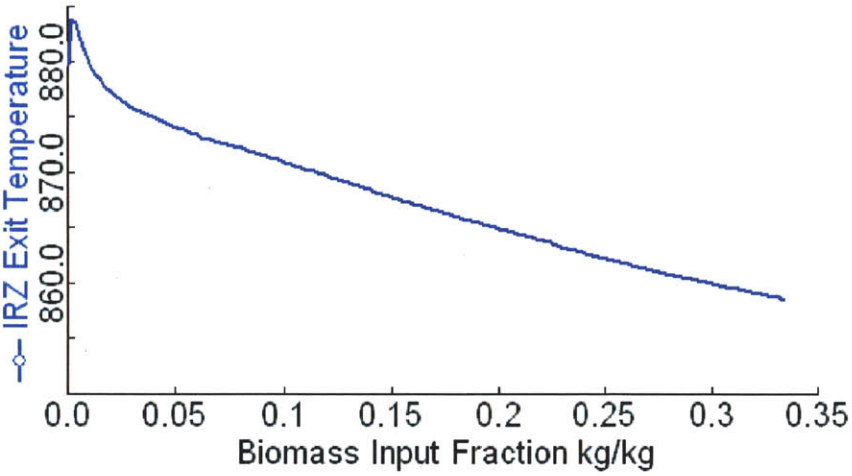

Figure 3-19. Exit gas temperature of IRZ Reactor as function of Wood Fraction with Biomass Kinetics and increased Moisture Content.

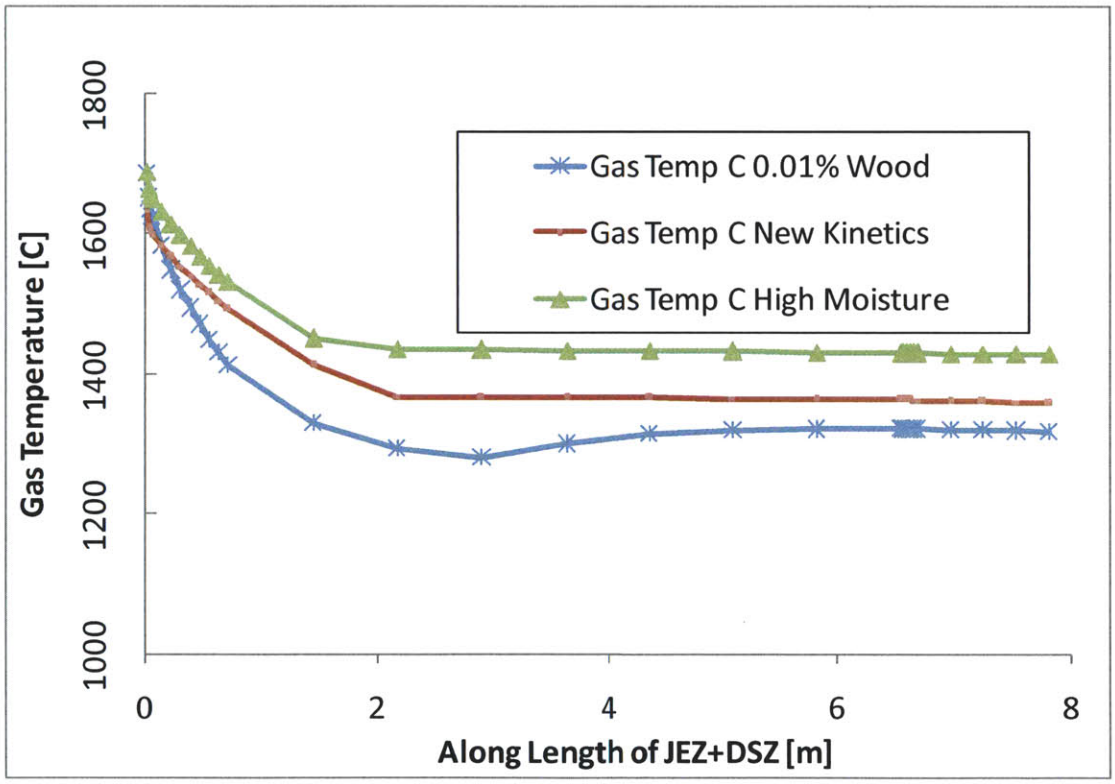

Figure 3-20. Temperature profiles along JEZ and DSZ reactors: Reference (coal only), biomass char kinetics (33% wood), and high moisture (33% wood).

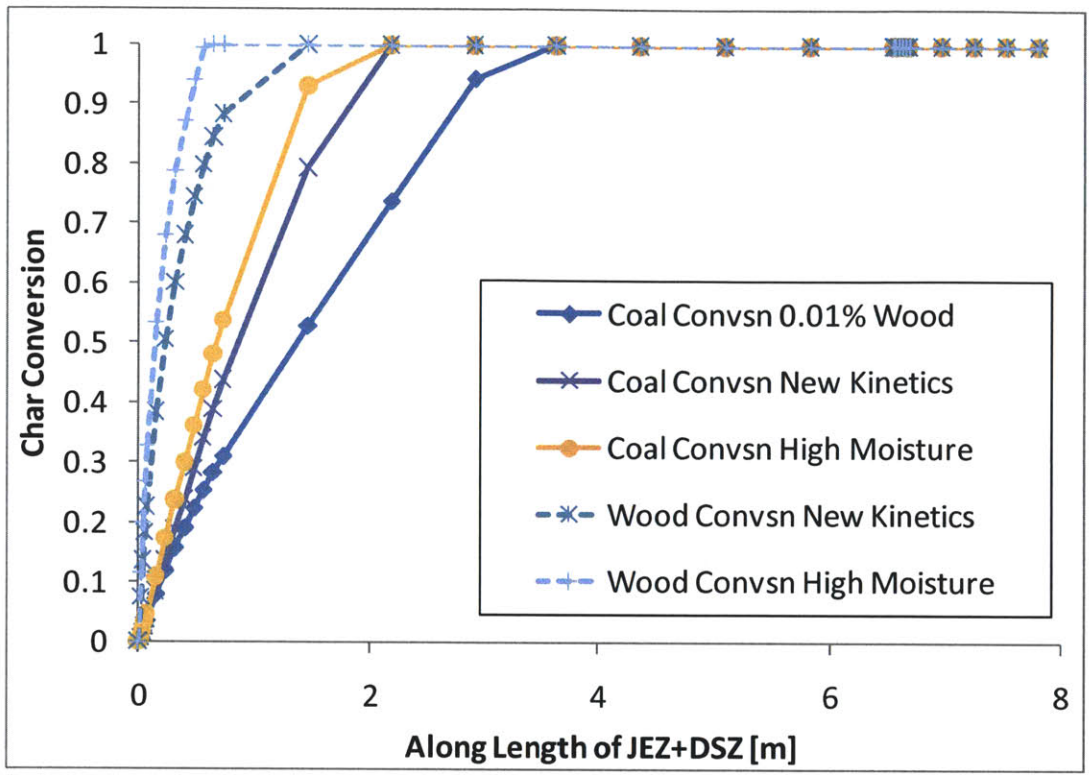

Figure 3-21. Conversion profiles along JEZ and DSZ reactors: Reference (coal only), biomass char kinetics (33% wood), and high moisture (33% wood).

With increased moisture content, both CGE and Syngas HHV decreased dramatically, as expected. As wood fraction goes from .01% and 33%, CGE drops 19.2% and Syngas HHV drops 29.4%. Before changing the moisture content, the same changes were 16.0% and 19.0%, respectively. CGE and Syngas for the High Moisture simulation are plotted in Figure 3-22. As previously mentioned, results for all the simulations are compared in Figures 3-33 to 3-35.

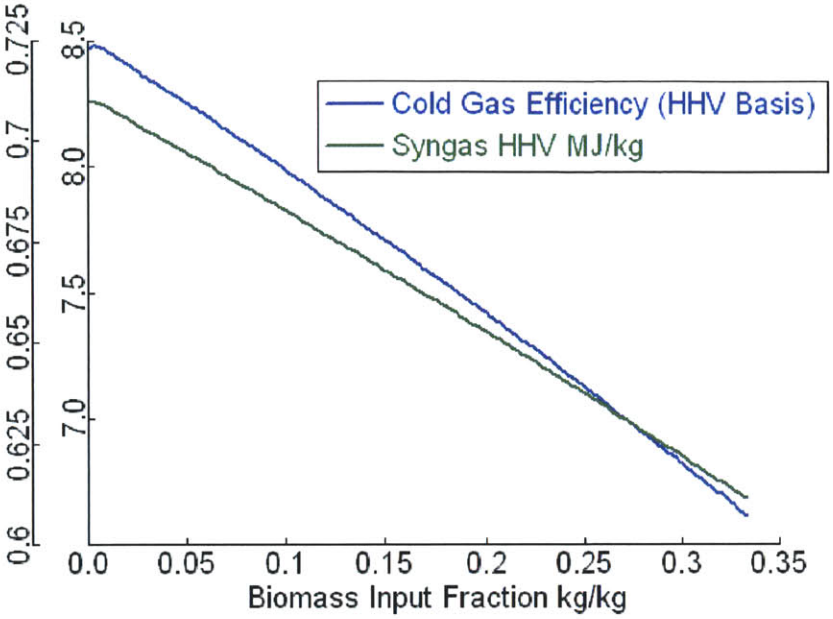

Figure 3-22. CGE and Syngas HHV as functions of Wood Input with Biomass Kinetics and increased Moisture Content

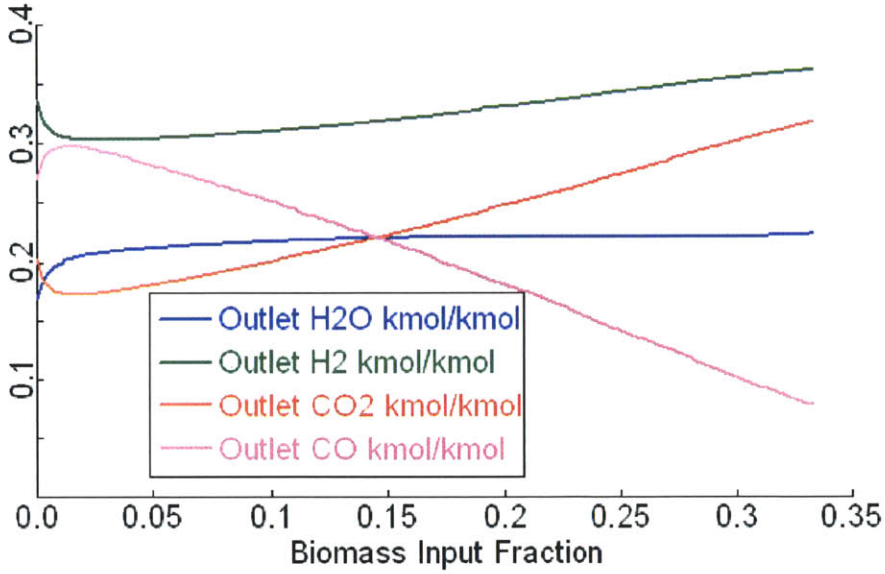

Figure 3-23. Syngas Composition after Cooler as function of Wood Input with Biomass Kinetics and increased Moisture Content.

3.8.4 *Fixed Oxygen-fuel Ratio*

To compensate for the increased oxygen content, and likewise decreased carbon and hydrogen content, a simulation Task was written to ramp up wood and ramp down oxygen. The target oxygen was computed by holding constant the oxygen-fuel ratio (stoichiometric oxygen-to-fuel coefficient over the supplied oxygen-to-fuel coefficient). The calculations are in Appendix A.2.

During the dynamic simulation of this case, Aspen Custom Modeler ran into an integrator issue multiple times at the same simulation time of .66 hours, or about 10% wood input fraction. It was also a particularly slow simulation. For this reason, data was collected at discrete points, and these points were reached using the Homotopy tool (continuation). This is only noticeable in results given as functions of biomass input fraction such as CGE and syngas composition.

The temperature and conversion profiles at 33% wood, compared to the previous case and the base case, are given in Figures 3-24 and 3-25 below. As expected, decreasing the oxygen feed to maintain a constant equivalent ratio leads to a decrease in gas temperature. This is because of the higher moisture content (heat capacity) of biomass. With lower temperatures, conversion is dramatically slowed for both feed particles.

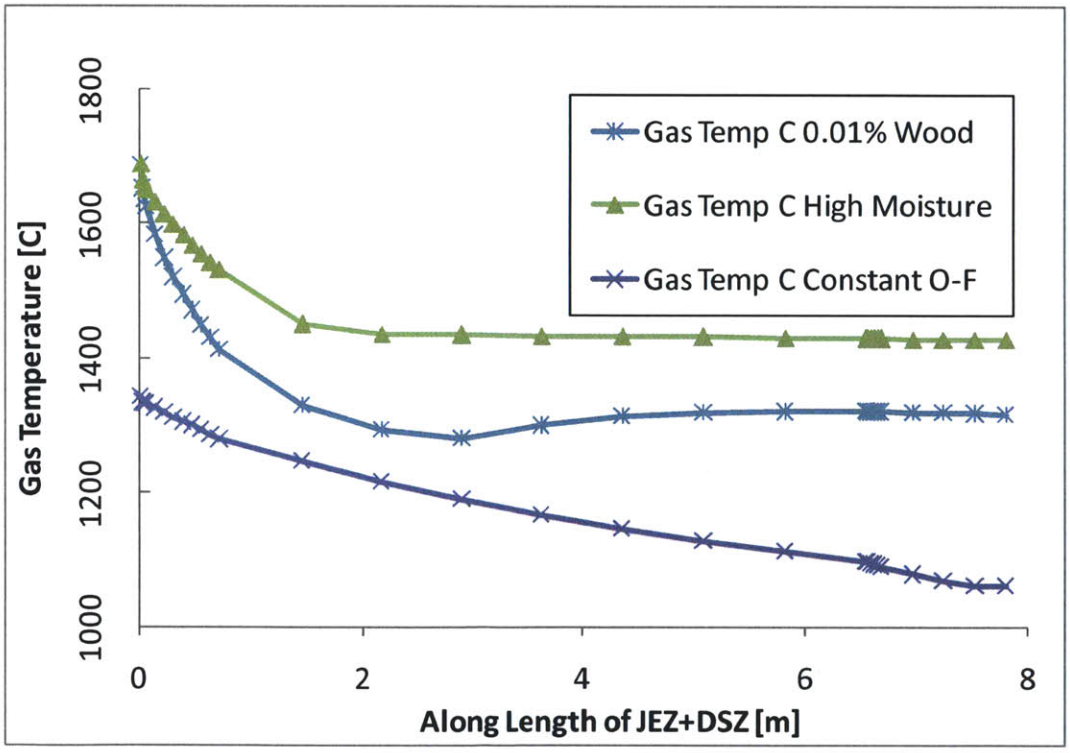

Figure 3-24. Temperature profiles along JEZ and DSZ reactors: Reference (coal only), high moisture (33% wood), and fixed oxygen-fuel ratio (33% wood).

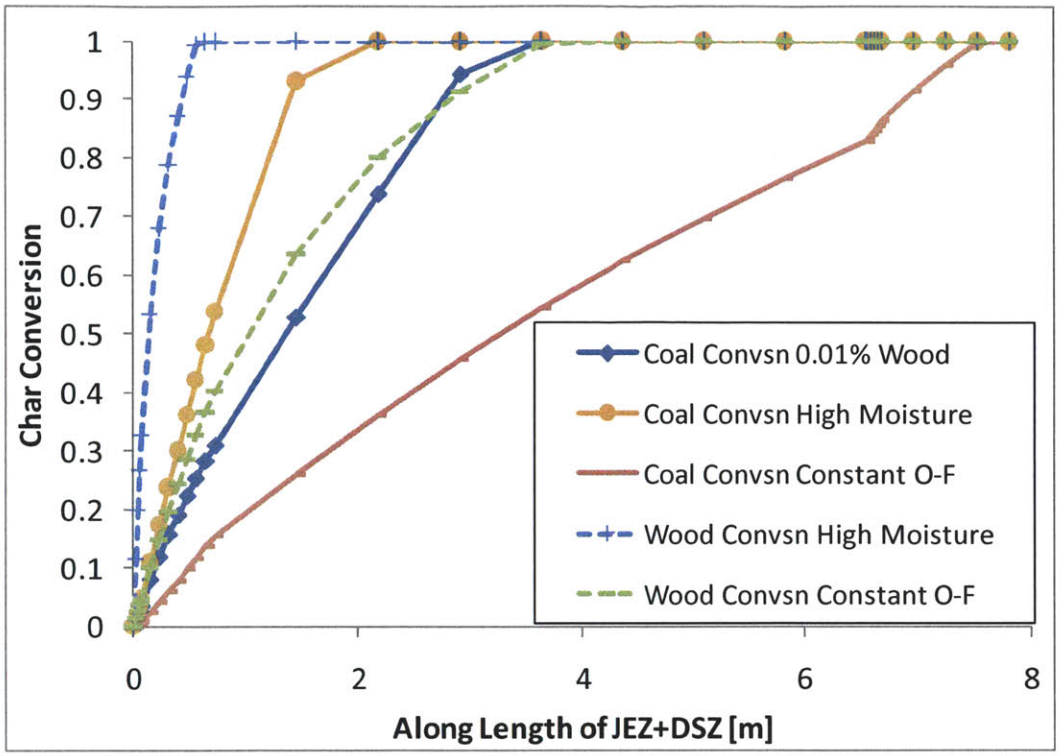

Figure 3-25. Conversion profiles along JEZ and DSZ reactors: Reference (coal only), high moisture (33% wood), and fixed oxygen-fuel ratio (33% wood).

While CGE and Syngas HHV still decrease with increasing wood fraction (Figure 3-26), they decrease less so than if oxygen stream input was constant (increasing total oxygen input). This is directly related to the change in syngas composition (Figure 3-27), which is also less dramatic than previous cases.

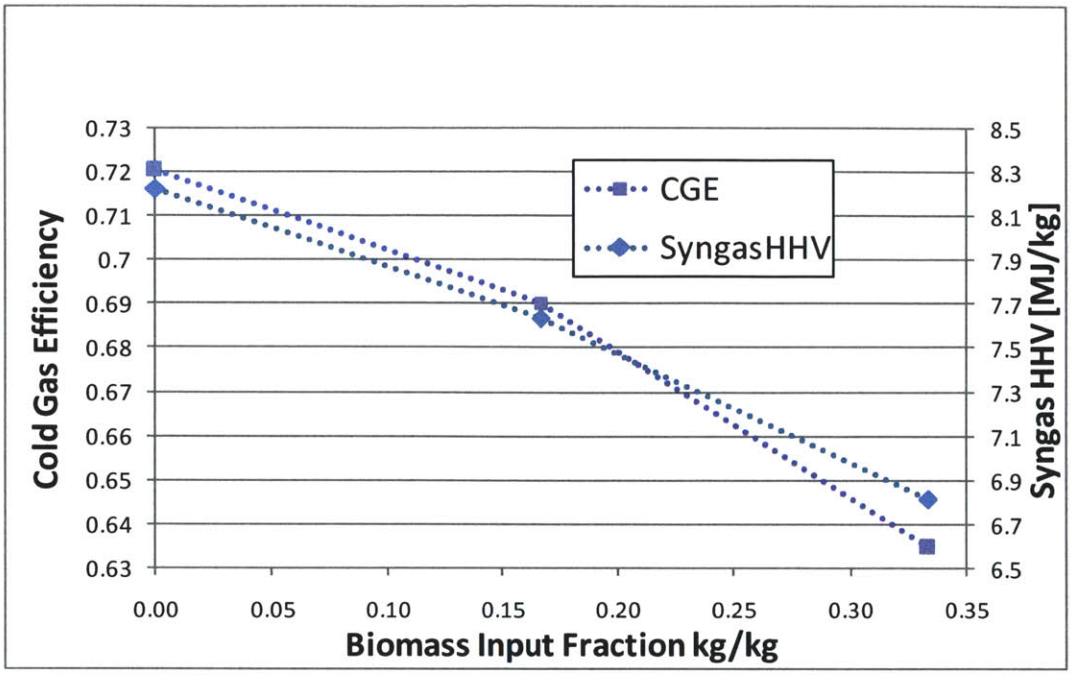

Figure 3-26. CGE and Syngas HHV as functions of Wood Input fraction for constant Oxygen-fuel Ratio.

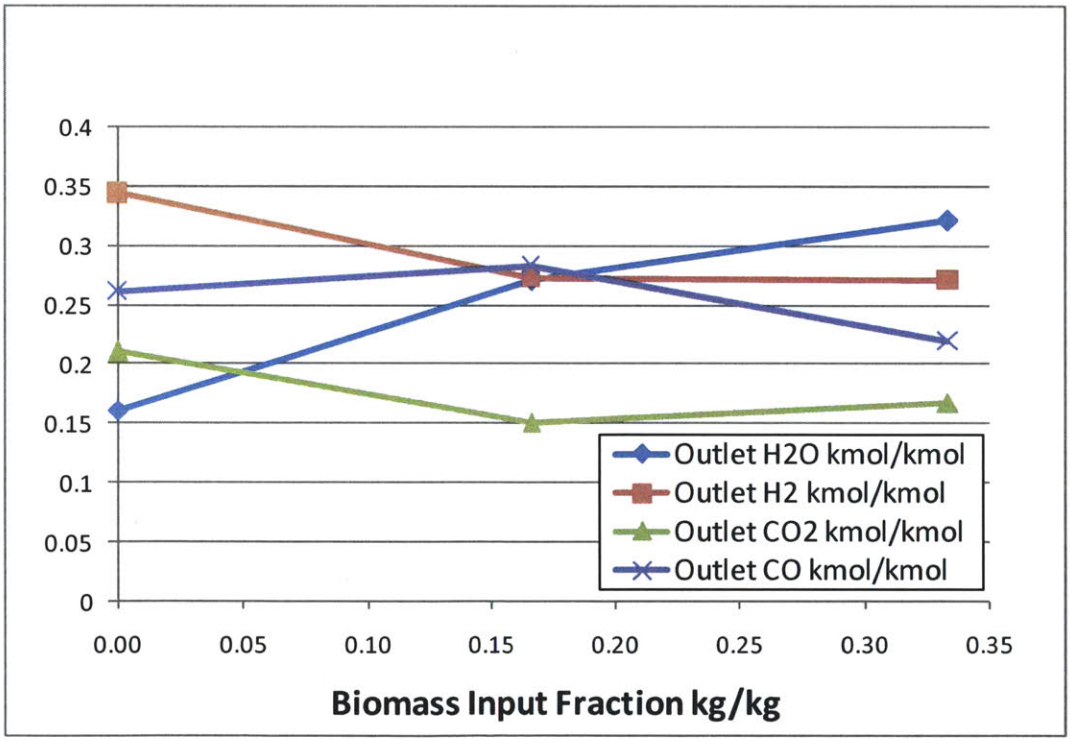

Figure 3-27. Syngas composition as function of Wood Input fraction for constant Oxygen-fuel Ratio.

3.8.5 *Fixed Gasifier Temperature*

The alternative to adjusting oxygen input to maintain a constant oxygen-to-fuel ratio is to adjust it to maintain a constant temperature at the exit from the gasifier. This was done by setting fixing one

temperature variable and freeing the oxygen input variable, starting with the High Moisture case. The exit temperature was chosen because the slag temperature is most important at this point. Conversion speed was not a concern because the simulation started with enough oxygen to completely convert all the feedstock early in the gasifier.

As in the constant A-F ratio case, there was difficulty in using the Dynamic mode to ramp up wood input fraction. However, it was at one value of wood input, about 3.5%. This was overcome by using homotopy (continuation) to increase the wood fraction beyond this point, and then the dynamic simulation was started again. This created a small discontinuity in some of the data presented below.

At 33% wood fraction, the oxygen feed decreased to 84.8 tons per hour from 89.0. Again, the temperature and conversion profiles at 33% wood, compared to the High Moisture case and the base case, are given in Figures 3-28 and 3-29. The cooling effect of drying/devolatilization can be seen in the lower peak temperature. It also is smoother than the curve of the coal case (less carbon to gasify) and meets the same final temperature (fixed). As expected, conversion speeds up compared to pure coal but is slower than the constant oxygen input case (High Moisture).

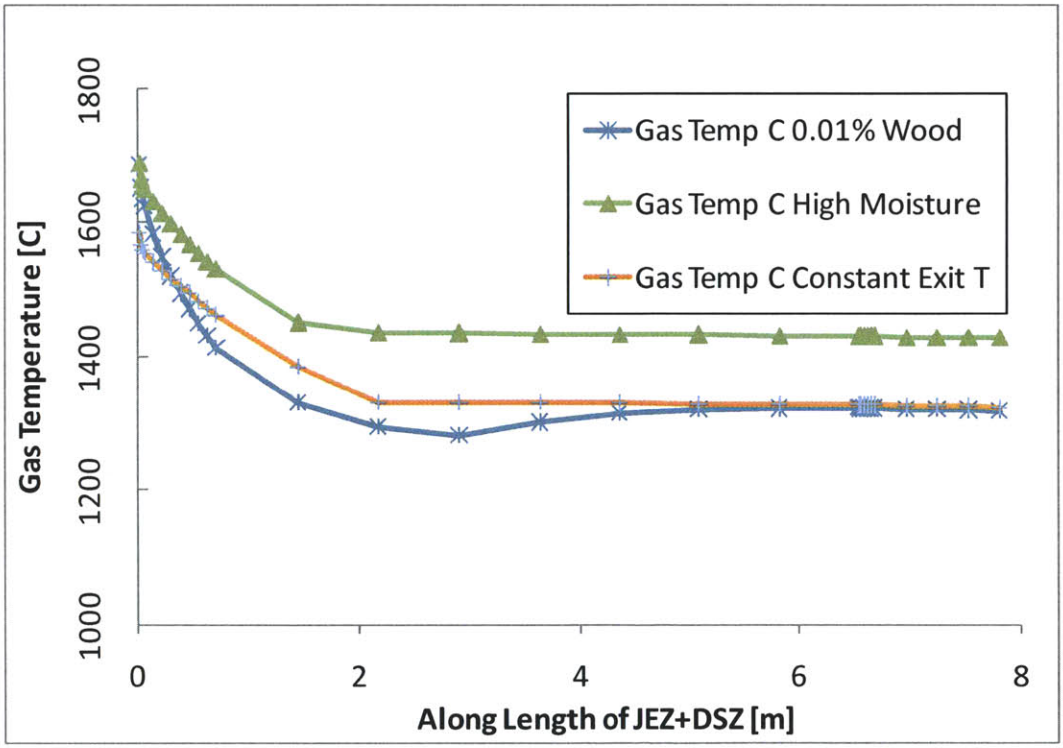

Figure 3-28. Temperature profiles along JEZ and DSZ reactors: Reference (coal only), high moisture (33% wood) and fixed temperature (33% wood).

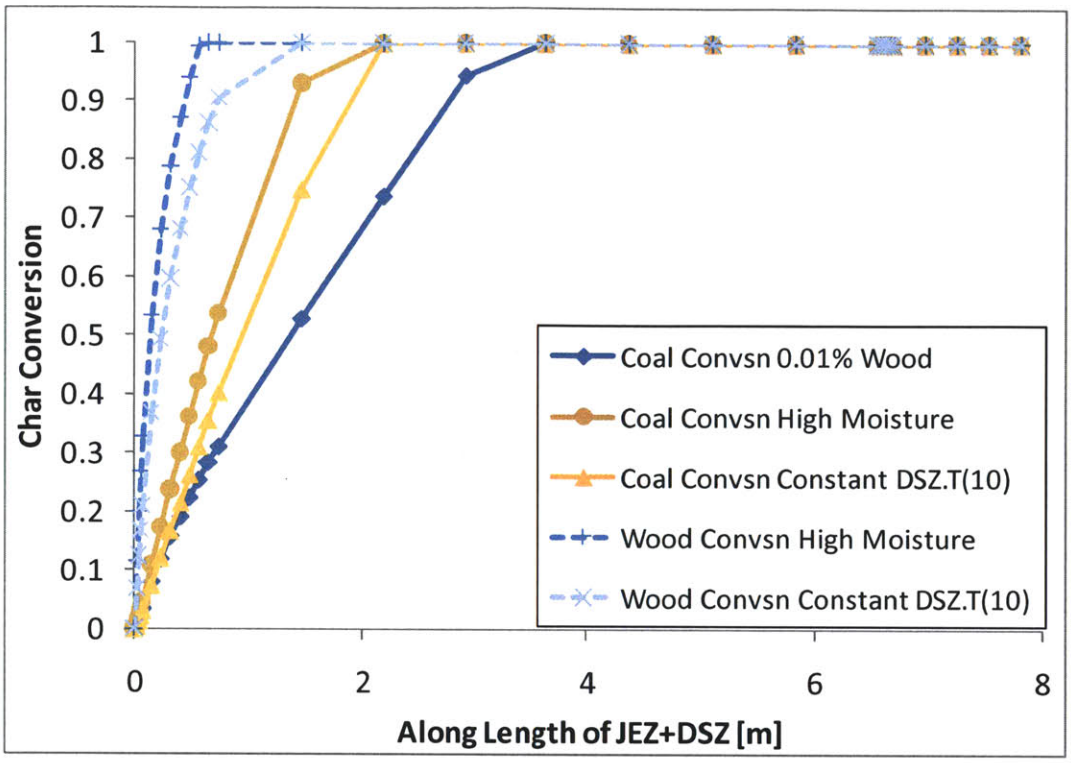

Figure 3-29. Conversion Profiles along JEZ and DSZ reactors: Reference (coal only), high moisture (33% wood) and fixed temperature (33% wood).

As mentioned above, the oxygen feed required to maintain the final control volume gas temperature decreased to 84.8 tons per hour from 89.0 tons per hour. As seen in Figure 3-30 below, this is a linear reduction. (The discontinuity is due to difficulty in convergence during the dynamic run, as described above.) The oxygen savings as a percentage is also provided, in Figure 3-31.

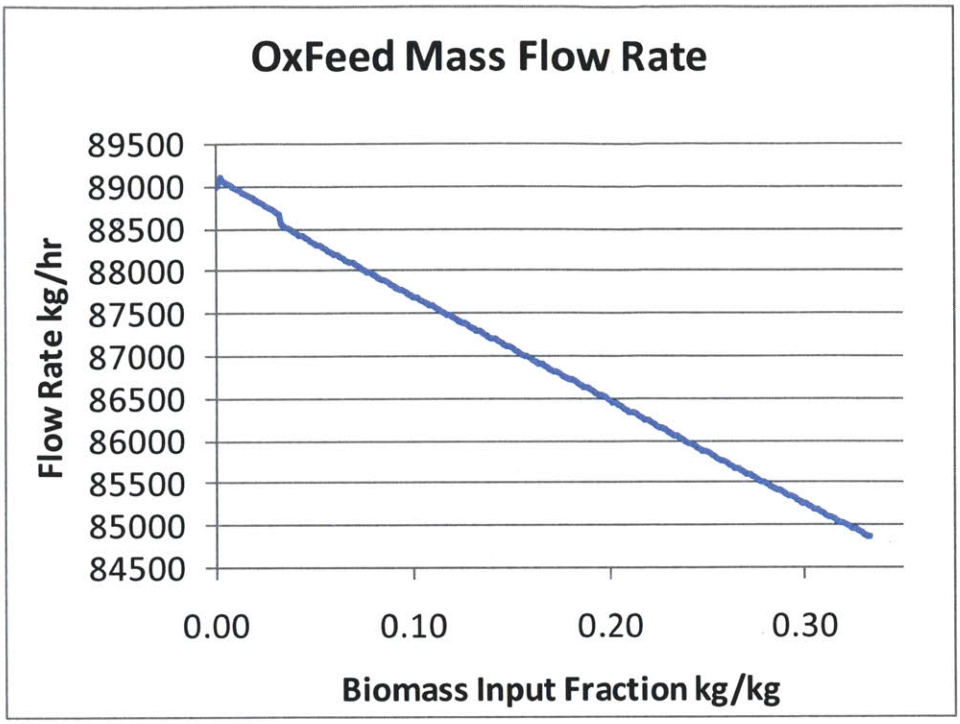

Figure 3-30. Oxygen Feed required to maintain constant temperature in the last section of the gasifier.

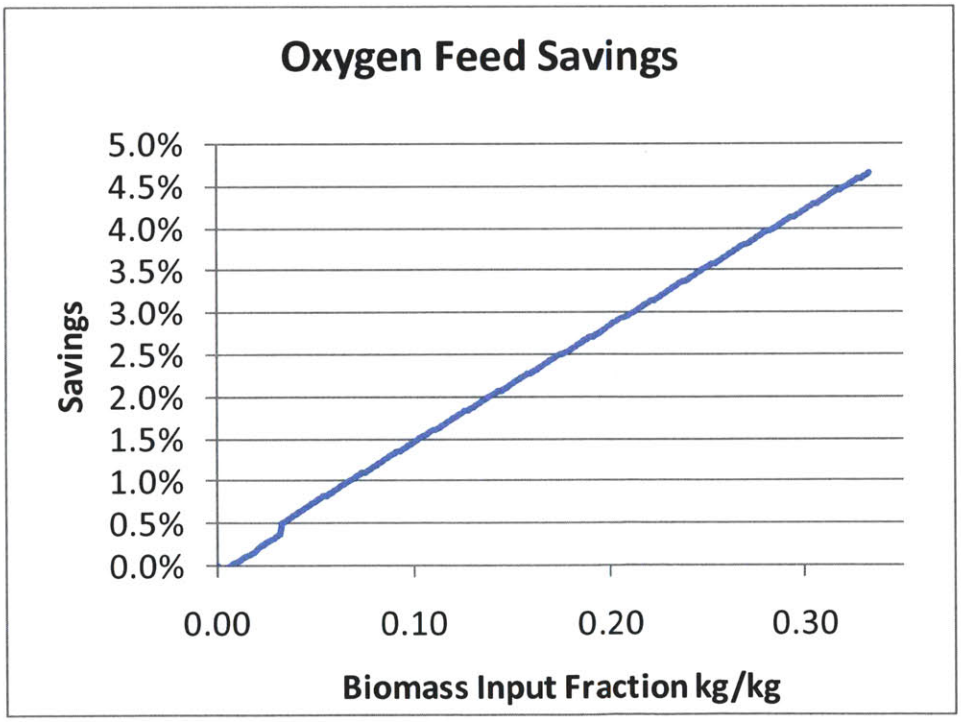

Figure 3-31. Oxygen Feed savings as a percentage, as a result of maintaining constant temperature.

CGE now decreases by 16.2%, compared to 19.0% in the High Moisture case. This is expected since there is less char combustion and more gasification. However, this does not fully reflect the

advantage of decreasing oxygen. Not only does the CGE improve, but the overall plant efficiency improves as a result of oxygen feed savings.

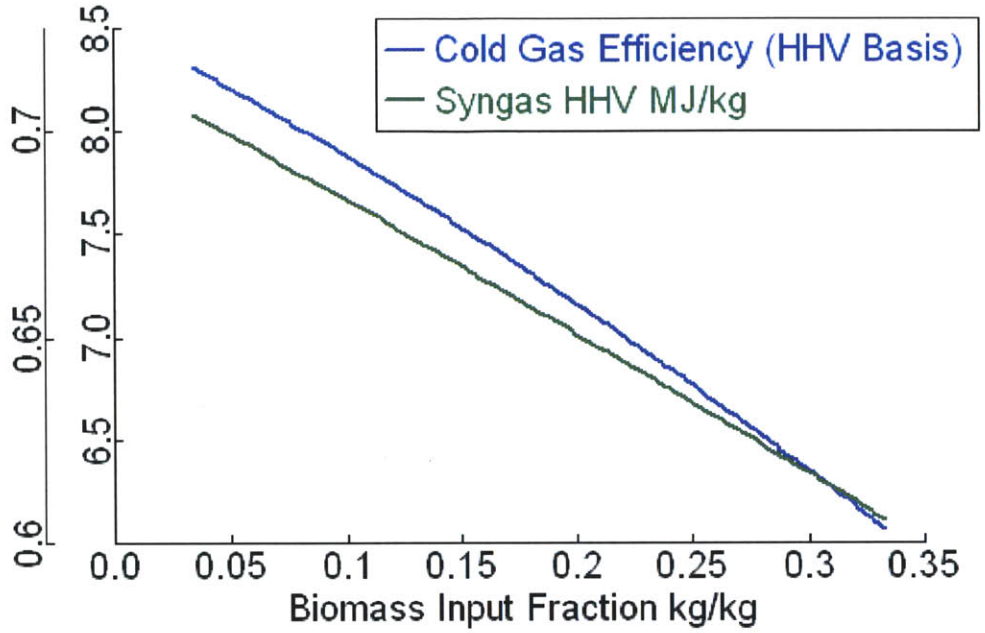

Figure 3-32. CGE and Syngas HHV as functions of Wood Input for Constant Temperature case.

3.9 ANALYSIS

Several characteristics of biomass have been incorporated into a model. From the results, the most important factors can be determined. As in the previous section, the outputs considered are Cold Gas Efficiency (CGE), maximum temperature, and slag viscosity and thickness.

3.9.1 COLD GAS EFFICIENCY

To understand the relative impact of each ROM modification, the CGE and Syngas HHV at different modeling stages as a function of wood input fraction are given in Figures 3-33 and 3-34. Both plots show that the largest impact comes from the first model changes: the devolatilization model and the ultimate/proximate analysis change. After this, moisture content is the biggest detriment. Reducing the oxygen input to maintain a constant oxygen-fuel ratio improves the output, while results above show that conversion time suffers. Reducing the oxygen to maintain constant downstream temperature completely removes the negative impact of high moisture on CGE and also significantly improves Syngas HHV.

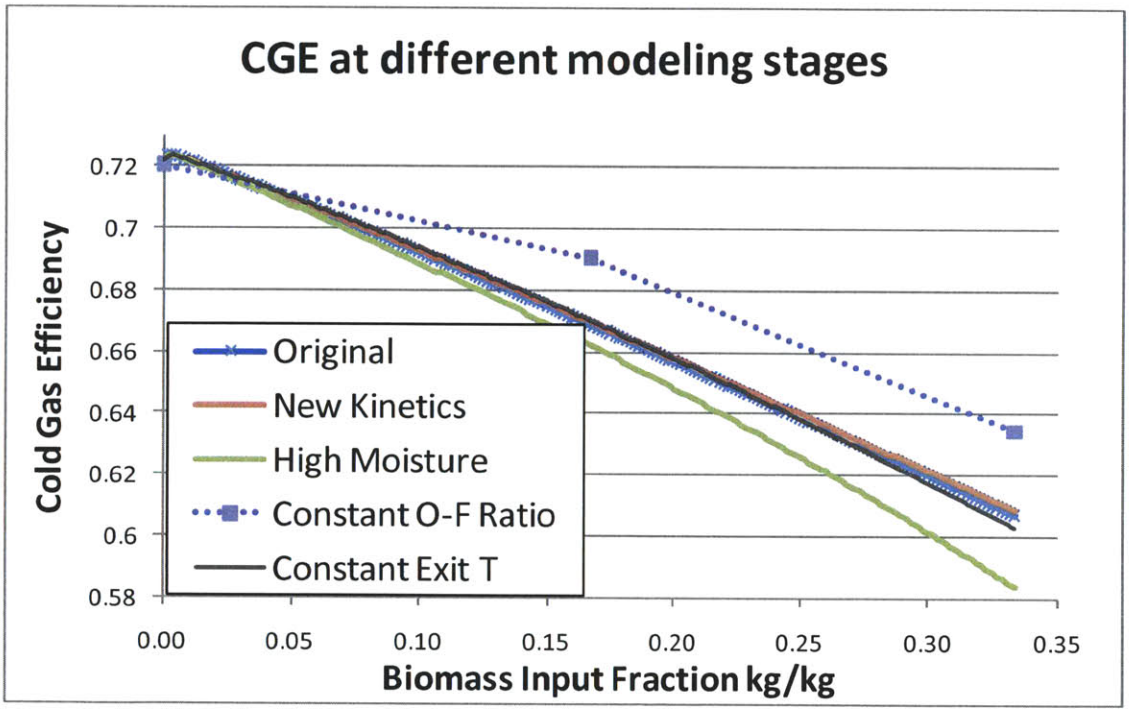

Figure 3-33. CGE at different modeling stages.

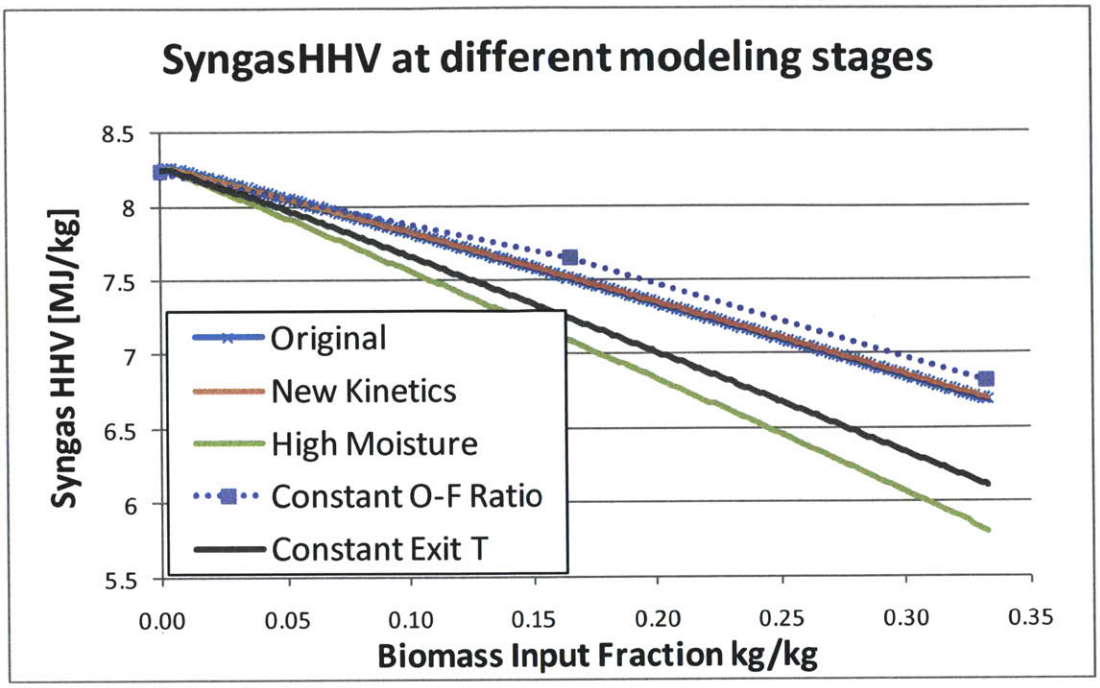

Figure 3-34. Syngas Higher Heating Value at different modeling stages.

Both plots are given to show that each change impacts the outputs differently, as the two quantities are different measures of output. In fact, they are not proportional. This is best shown in Figure 3-35 below, which compares CGE and Syngas HHV. The plot shows that Syngas HHV falls faster than CGE does because part of the reason Syngas HHV falls is decreased input value, which is reflected positively in CGE.

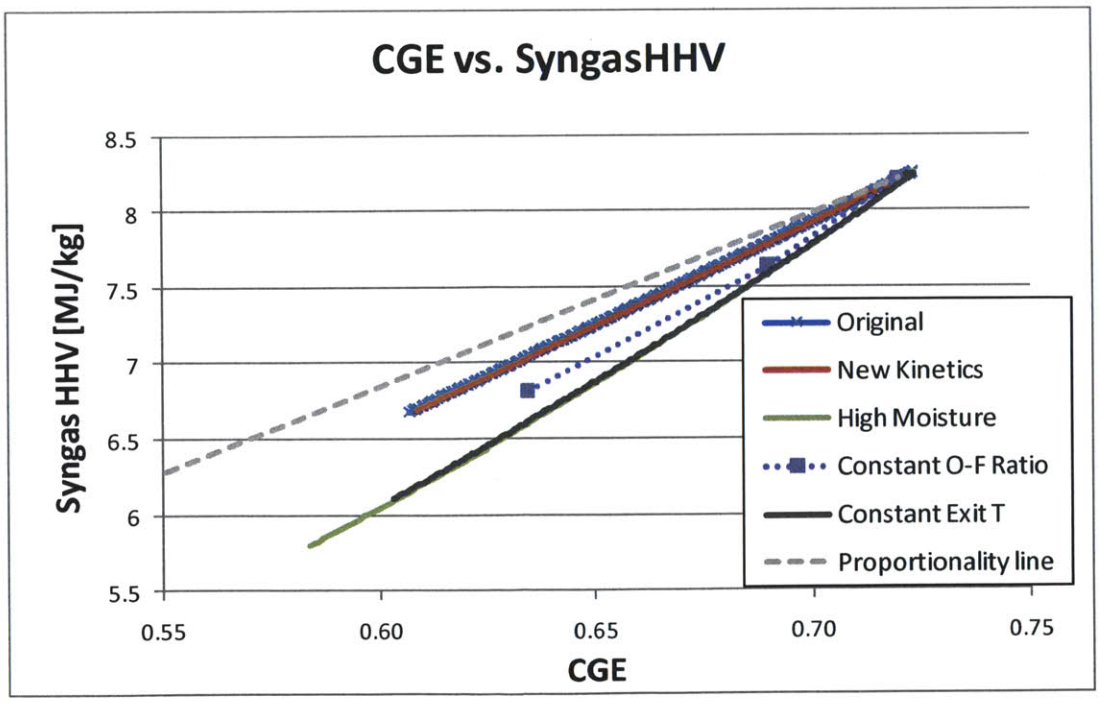

Figure 3-35. Comparison of CGE and Syngas HHV at different modeling stages.

Based on the strong effect of Moisture content on CGE, biomass feedstocks should be dried as much as possible. Also, it is important to adjust the oxygen input to account for the high oxygen in biomass, to keep the temperature down and the syngas value high. However, simply keeping the oxygen-fuel ratio constant does not keep the temperature content constant, due to extra heat capacity and drying heat. The temperature actually decreases too much, so some other method of calculating the constant temperature oxygen requirement must be sought. This can be done algebraically (iteratively) or by adjusting which variables are fixed in the ROM.

3.9.2 OXYGEN FEED SAVINGS/ FACTORS LIMITING OPERATION

When the Oxygen feed is reduced as in the Constant Oxygen-fuel Ratio case, there is a substantial energy savings for the plant. The oxygen savings as a fraction for this case is given in Figure 3-36 below. However, it is not possible to raise the wood fraction high enough to realize these savings because the temperature drops too low.

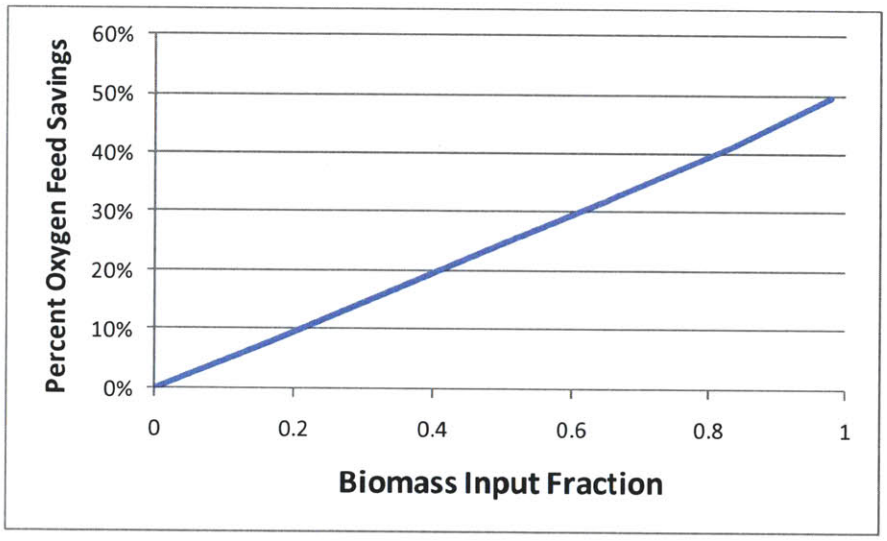

Figure 3-36. Oxygen Savings for constant Oxygen-fuel ratio case.

Entrained Flow Gasifiers must operate above about 1400 °C minimum gas temperature. Part of the reason is keeping the ash in a liquid state, second is to keep the conversion efficiency high in a short residence-time reactor. This is not-withstanding the fact that the model assumes high temperature for the devolatilization reactions. Therefore, as the wood fraction increases and the oxygen feed is decreased, there is a point at which the temperature falls too low. This point depends on the expected final char conversion. With constant oxygen-fuel ratio, for complete conversion of all feeds, the maximum wood input is just above 33%. However, if the ROM is used to find the oxygen input required to maintain constant temperature, the wood ratio could be increased until the model assumptions break down. For example, at about 70% wood, the devolatilization temperature (IRZ temperature) is 670 °C, which is too

low to completely devolatilization the wood in less than one second. The oxygen savings for the constant temperature case is given in Figure 3-37.

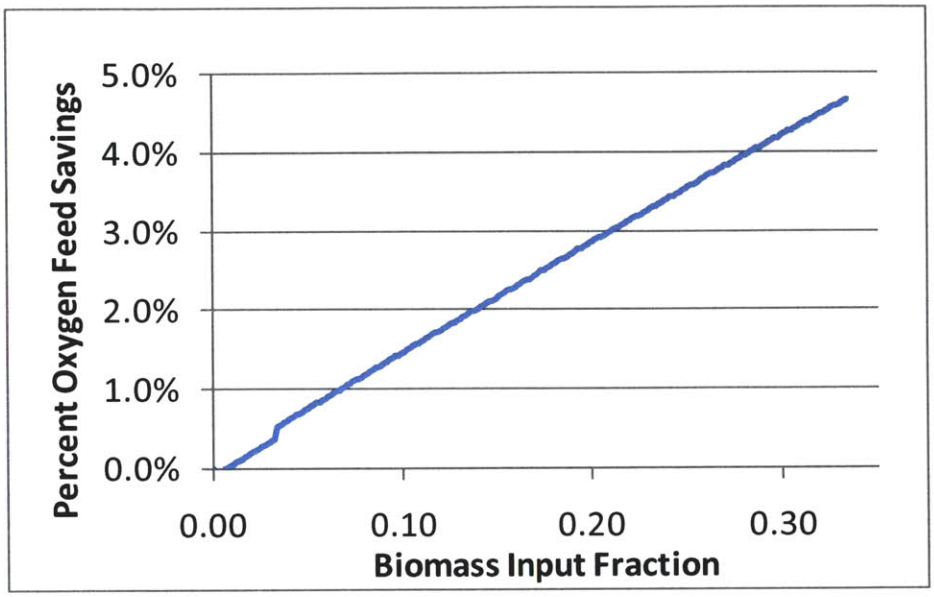

Figure 3-37. Oxygen Feed savings as a percentage in Constant Temperature case.

3.9.3 *Slag Behavior*

As discussed early in the results, the change in slag viscosity has two contributions, temperature and composition. To separate the effects of composition and temperature, the slag state is compared under various conditions in Table 3-6. The table shows the state for all coal (0.01% wood), with 33% wood where wood ash composition is set to that of coal, then set to wood ash, and finally under the constant temperature constraint. The data is given for two different points in the reactor - the end of the JEZ and the end of the DSZ (end of gasifier).

Table 3-6. Slag state as result of changing wood ash composition (old kinetics, 10% moisture)

Wood Fraction	All Coal	33% Wood	33% Wood	33% Wood
Wood's Ash Comp	n/a	Coal	Wood	Wood
Other conditions	Original ROM	Coal Kinetics, 10% moisture	Coal Kinetics, 10% moisture	Constant DSZ Temperature
End Slag Temp	1320 °C	1625 °C	1625 °C	1320 °C
JEZ / Slag Viscosity	11.882Pa-s	8.812 Pa-s	9.049 Pa-s	12.029 Pa-s
JEZ / Slag Thickness	5.412 mm	4.706 mm	4.747 mm	5.19 mm
DSZ / Slag Viscosity	12.210Pa-s	9.160 Pa-s	9.408 Pa-s	12.421 Pa-s
DSZ / Slag Thickness	5.781 mm	4.992 mm	5.036 mm	5.495 mm

First, the values show that viscosity and therefore thickness decreased with the higher temperature (the result of increasing wood fraction and holding oxygen input constant) and increased with

the new ash composition. The latter fact is expected because wood ash increases the silica and decreases network modifiers such as calcium, sodium and iron oxides, pushing the already acidic ash even more towards the acid side. Also as expected, the viscosity change due to changing composition is very small because ash is a small compositional fraction of a small input fraction. Second, the effects of wood composition are further illustrated by examining the slag state in the constant reactor temperature case. Again, the viscosity increased from higher silica content, but the thickness decreased from the lower ash fraction.

3.9.4 Regarding Kinetics Data

While changing the char conversion kinetics had an impact on the conversion time in the simulation, it seems that the outputs are weakly affected. As discussed in the results section, this is partly because of the small amount of wood char in the system and partly because the conversion profile lasts only a short distance through the length of the JEZ. It is unclear why the original feedstock and kinetics leads to such a quick and complete conversion, though it may be due to the atmospheric pressure condition of the source data. However, while the kinetics did not have a major impact on the outputs of the model, it does help make the following case for operation: since wood char converts relatively quickly, it may work well in a multi-stage gasifier as the last feedstock input.

4 CONCLUSION

4.1.1 SUMMARY OF WORK

Biomass is renewable source of fixed carbon. Relative to coal, it is high in volatiles and low in ash; moisture content varies by processing condition and pretreatment. Pretreatment options include pyrolysis to char and pumpable bio-oil, and torrefication – light thermal conversion which yields a hydrophobic, brittle solid that is higher in energy density.

The devolatilization process is an important conversion step whose rate and yield can be found through a system of parallel and series reactions. The most detailed mechanism to date is put forth in Ranzi et al. (2008), which includes 42 species and 18 equations.

After devolatilization, an amorphous char is left that combusts or gasifies in much the same way as coal. These surface reactions have been modeled with Random Pore Model and Shrinking Core models, though the most common kinetic data is available in the form of reactivity expressions. Experiments have shown that reactivity is dependent on ash content and devolatilization conditions, making it difficult if not impossible to represent a wide range of conditions in a reactivity expression.

Ash slag characterization is important for high temperature processes such as Entrained Flow Gasification. While the ash content of biomass differs from that of coal, some of the tools used to analyze coal ash are capable of representing biomass ash.

4.1.2 SUMMARY OF RESULTS

The expansion of the GE 2700tpd ROM enabled the effects of co-feeding coal and woody biomass on operation and output to be studied. It confirmed the detrimental effects of increased oxygen and moisture content on Cold Gas Efficiency. The effort revealed that oxygen feed must be controlled to maintain reactor temperature, though it is not a simple function of the oxygen content of the feedstock. The model's outputs are not sensitive to biomass char kinetics as long as conditions are such that the feed converts completely.

4.1.3 FUTURE WORK

There is room for development of the co-feeding ROM in the following areas. Slurry properties will vary with feed stock, particularly because biomass has a low maximum solids loading. Due to the hydrophilic nature of biomass, solid loading is as low as 13-15% compared to coal at 65-68%, though torrefication can increase this fraction to 40% (He et al. 2009). The lower loading value should be reflected in the slurry water feed rate. Further, a dry-fed gasifier should be considered, since high-moisture feedstocks are often associated with this type.

Torrefied wood as a feedstock is a likely candidate for entrained flow gasification due to its increased heating value and storability. Its hydrophobicity makes it especially beneficial for in slurry-fed gasifiers, because as mentioned above, as this feature gives it a higher maximum slurry loading. Torrified wood could be implemented using the expanded ROM framework, with some modification to the devolatilization yield mechanisms and char reactivity parameters.

The original particle-level model assumed that the particles are small enough that there is no internal temperature gradient. Raw wood is not likely to be pulverized to sizes in this domain in commercial applications. The particle-level model should be augmented to better reflect the larger particle size and cylindrical shape of biomass, perhaps through effectiveness factors.

The kinetics data used for both coal and biomass are for atmospheric conditions or less than atmospheric. The fact that the ROM reports full conversion very early in the gasifier suggests that the kinetics expressions may be over-predicting the rate of conversion, which is likely due to the high pressure value (56 bar). The conversion prediction of the ROM could be improved by finding and implementing "at-pressure" kinetic data.

APPENDIX

Appendix A. SAMPLE CALCULATIONS

Appendix A-1. DETERMINING LIGNIN COMPOSITION

Ranzi et al. (2008) provided the following compositions for soft wood:

C/H/O by mass: 53.2/6.0/40.4

In terms of biocomponents:

Cellulose	40.1%wt	C6H10O5
Hemicellulose	26.7%wt	C5H8O4
Lignins	33.2%wt	Varies

Using the above information, the fraction of lignin must have a C/H/O mass ratio of: 70.0/5.7/23.1

The study considers three simplified lignin types, each named for its dominate element. Their structure and compositions are given in Figure A-1 below.

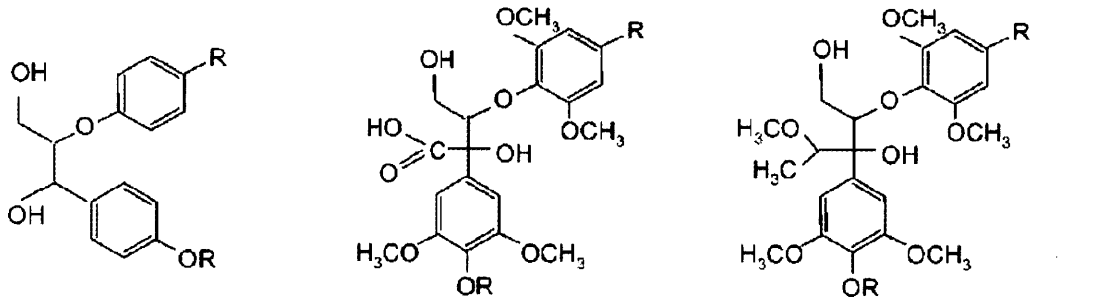

LIG-C $C_{15}H_{14}O_4$ (69.8%C 5.4%H 24.8%O)

LIG-O $C_{16}H_{10}O_6(OCH_3)_4$ (56.9%C 5.2%H 37.9%O)

LIG-H $C_{17}H_{13}O_4(OCH_3)_5$ (60.6%C 6.4%H 33.0%O)

Figure A-1. Lignin structures. (Ranzi et al. 2008)

Using the above information, the lignin composition should be solvable. However, the given C/H/O composition is outside of the domain of the lignin chemical compositions, and results include negative numbers:

Lig-C	25%
Lig-H	80%
Lig-O	-5%

While trying to stay close to this result, a suitable combination of lignins was assumed: 20% Lig-C, 80% Lig-H.

Appendix A-2. CONSTANT OXYGEN-FUEL RATIO

First, the original Oxygen-fuel ratio (λ) used in the ROM with Coal must be found. This involves determining the molecular composition of coal, the amount of oxygen required for complete combustion, and the amount of oxygen supplied also on a molecular basis.

Coal mass composition (balance is moisture and ash, which cancel out of the subsequent calculations)

Carbon	Hydrogen	Oxygen	Nitrogen	Sulfur
.569182	.0467886	.156406	.00998669	.0175285

Divide each elemental mass fraction by the respective elemental atomic weight.

Coal molecular composition (kilomoles per kilogram coal)

Carbon (a)	Hydrogen (b)	Oxygen (c)	Nitrogen (d)	Sulfur (e)
.047392	.046325	.0097753	.000712825	.000546570

Complete combustion is $C_aH_bO_cN_dS_e + \alpha\ O2 \rightarrow aCO2 + bH2O + dNO2 + eSO2$. From this,

$$\alpha_{coal} = a + \frac{1}{4}b + d + e - \frac{1}{2}c = .0553450\ \frac{\text{kmol O2}}{\text{kgram coal}}$$

The oxygen being supplied is found from the mass flowrate of Oxygen Feed (OF) and the O_2 mass fraction of the OF (95%). Then the supplied oxygen is converted to a mole per mass coal basis.

$$\beta_{coal} = \frac{\dot{m}_{OF} \times .95 \frac{\text{kg O2}}{\text{kg OF}}}{\dot{m}_{Coal}} \times \frac{\text{kmol O2}}{32\ \text{kg O2}} = .02293309 \frac{\text{kmol O2}}{\text{kgram coal}}$$

The oxygen-fuel ratio is the ratio of the actual oxygen supplied to the stoichiometric oxygen required.

$$\lambda = \frac{\beta_{coal}}{\alpha_{coal}} = .41436$$

Now, the Oxygen-fuel ratio (λ) is used to figure out the proper oxygen to supply with a new fuel molecular composition.

Biomass mass composition (balance is moisture and ash, which cancel out of the subsequent calculations)

Carbon	Hydrogen	Oxygen	Nitrogen	Sulfur
.314243	.0384664	.267296	-	-

Divide each elemental mass fraction by the respective elemental atomic weight.

Wood molecular composition (kilomoles per kilogram wood)

Carbon (a)	Hydrogen (b)	Oxygen (c)	Nitrogen (d)	Sulfur (e)
.0261651	.0380855	.016706	-	-

Again for complete combustion,

$$\alpha_{wood} = a + \frac{1}{4}b + d + e - \frac{1}{2}c = .0273334 \frac{\text{kmol O2}}{\text{kgram wood}}$$

Finally, the total oxygen supply is found from flowrate-weighting the oxygen supplies for the two feedstocks.

$$\alpha_{combined} = \frac{2}{3}\alpha_{coal} + \frac{1}{3}\alpha_{wood} = .0460077 \frac{\text{kmol O2}}{\text{kg feed}}$$

$$\beta_{combined} = \lambda \times \alpha_{combined} = .01906376 \frac{\text{kmol O2}}{\text{kg feed}}$$

$$\dot{m}_{OF} = \beta_{combined} \times \dot{m}_{Feed} \times \frac{1}{.95 \frac{\text{kg O2}}{\text{kg OF}}} \times 32 \frac{\text{kg O2}}{\text{kmol O2}} = 73983 \frac{\text{kg}}{\text{hr}}$$

WORKS CITED

Biagini, E., Barontini, F. & Tognotti, L., 2006. Devolatilization of Biomass Fuels and Biomass Components Studied by TG/FTIR Technique. *Industrial & Engineering Chemistry Research*, 45(13), pp.4486-4493.

Boateng, A.A. et al., 2007. Bench-Scale Fluidized-Bed Pyrolysis of Switchgrass for Bio-Oil Production†. *Industrial & Engineering Chemistry Research*, 46(7), pp.1891-1897.

Boroson, M.L., Howard, J.B., Longwell, J.P. & Peters, W.A., 1989a. Heterogeneous cracking of wood pyrolysis tars over fresh wood char surfaces. *Energy & Fuels*, 3(6), pp.735-740.

Boroson, M.L., Howard, J.B., Longwell, J.P. & Peters, W.A., 1989b. Product yields and kinetics from the vapor phase cracking of wood pyrolysis tars. *AIChE Journal*, 35(1), pp.120-128.

Bradbury, A.G.V., Sakai, Y. & Shafizadeh, F., 1979. *J. Appl. Polym. Sci.*, 23, p.3271.

Branca, C., Albano, A. & Di Blasi, C., 2005. Critical evaluation of global mechanisms of wood devolatilization.

Branca, C., Di Blasi, C. & Russo, C., 2005. Devolatilization in the temperature range 300-600 K of liquids derived from wood pyrolysis and gasification. *Fuel*, 84(1), pp.37-45.

Bustamante, F. et al., 2005. Uncatalyzed and wall-catalyzed forward water–gas shift reaction kinetics. *AIChE Journal*, 51(5), pp.1440-1454.

Coda, B. et al., 2007. Slagging Behavior of Wood Ash under Entrained-Flow Gasification Conditions. *Energy & Fuels*, 21(6), pp.3644-3652.

Dayton, D.C. et al., 1999. Release of Inorganic Constituents from Leached Biomass during Thermal Conversion. *Energy & Fuels*, 13(4), pp.860-870.

Di Blasi, C., 2009. Combustion and gasification rates of lignocellulosic chars. *Progress in Energy and Combustion Science*, 35(2), pp.121-140.

Di Blasi, C., 1993. Modeling and simulation of combustion processes of charring and non-charring solid fuels. *Progress in Energy and Combustion Science*, 19(1), pp.71-104.

Di Blasi, C., 2004. Modeling wood gasification in a countercurrent fixed-bed reactor. *AIChE Journal*, 50(9), pp.2306-2319.

Dupont, C. et al., 2008. Biomass pyrolysis: Kinetic modelling and experimental validation under high temperature and flash heating rate conditions. *Journal of Analytical and Applied Pyrolysis*, 85, pp.260-267.

Gera, D. et al., 2002. Effect of Large Aspect Ratio of Biomass Particles on Carbon Burnout in a Utility Boiler. *Energy & Fuels*, 16(6), pp.1523-1532.

He, W., Park, C.S. & Norbeck, J.M., 2009. Rheological Study of Comingled Biomass and Coal Slurries with Hydrothermal Pretreatment†. *Energy & Fuels*, 23(10), pp.4763-4767.

Hemmati, M. & Laguerie, C., 1988. Determination of the kinetics of the wood sawdust steam gasification of charcoal in a thermobalance. *Entropie*, (142), pp.29-40.

Higman, C. & van der Burgt, M., 2008. Gasification (2nd Edition). Available at: http://www.knovel.com/web/portal/browse/display?_EXT_KNOVEL_DISPLAY_bookid=2322 [Accessed December 16, 2009].

Himes, R., 2001. *Slag Viscosity Measurements*, Palo Alto, CA: EPRI.

J.D. Watt & F Fereday, 1969. Flow properties of slags formed from ashes of british coals. *Journal of the Institute of Fuel*, 42(338), p.99.

Janse, A.M.C. et al., 1998. Combustion Kinetics of Char Obtained by Flash Pyrolysis of Pine Wood. *Industrial & Engineering Chemistry Research*, 37(10), pp.3909-3918.

Jones, W.P. & Lindstedt, R.P., 1988. Global reaction schemes for hydrocarbon combustion. *Combustion and Flame*, 73(3), pp.233-249.

Koufopanos, C.A., Lucchesi, A. & Maschio, G., 1989. Kinetic modelling of the pyrolysis of biomass and biomass components. *The Canadian Journal of Chemical Engineering*, 67(1), pp.75-84.

Koufopanos, C.A. et al., 1991. Modelling of the pyrolysis of biomass particles. Studies on kinetics, thermal and heat transfer effects. *Canadian Journal of Chemical Engineering*, 69(4), pp.907-915.

Liden, A., Berruti, F. & Scott, D.S., 1988. A kinetic model for the production of liquids from the flash pyrolysis of biomass. *Chemical Engineering Communications*, 65(1), pp.207 - 221.

Lu, H. et al., 2008. Comprehensive Study of Biomass Particle Combustion. *Energy & Fuels*, 22(4), pp.2826-2839.

Manomet Center for Conservation Sciences, 2010. Biomass Sustainability and Carbon Policy Study. Available at: http://www.mass.gov/?pageID=eoeeaterminal&L=4&L0=Home&L1=Energy%2C+Utilities+%26+Clean+Technologies&L2=Renewable+Energy&L3=Biomass&sid=Eoeea&b=terminalcontent&f=doer_arra_bscps&csid=Eoeea [Accessed April 25, 2011].

Merrick, D., 1983. Mathematical models of the thermal decomposition of coal: 1. The evolution of volatile matter. *Fuel*, 62(5), pp.534-539.

Miller, R.S. & Bellan, J., 1997. A Generalized Biomass Pyrolysis Model Based on Superimposed Cellulose, Hemicelluloseand Liqnin Kinetics. *Combustion Science and Technology*, 126(1), pp.97 - 137.

Monaghan, R.F.D., 2009. Presentation on Reduced Order Modeling of Entrained Flow Gasification.

Monaghan, R.F.D., 2010. *Dynamic Reduced Order Modeling of Entrained Flow Gasifiers*. PhD. Cambridge, MA: Massachusetts Institute of Technology.

Okumura, Y., Hanaoka, T. & Sakanishi, K., 2009. Effect of pyrolysis conditions on gasification reactivity of woody biomass-derived char. *Proceedings of the Combustion Institute*, 32(2), pp.2013-2020.

Pan, W.P. & Serageldin, M.A., 1987. Structural characterization of lignite coal and char with CaCl2. *Fuel Processing Technology*, 15, pp.397-409.

Pyle, D.L. & Zaror, C.A., 1984. Models For The Low Temperature Pyrolysis Of Wood Particles. In *Thermochemical Processing of Biomass.* Birmingham, Engl, pp. 201-216.

Ranzi, E. et al., 2008. Chemical Kinetics of Biomass Pyrolysis. *Energy & Fuels*, 22(6), pp.4292-4300.

Risnes, H., Sørensen, L.H. & Hustad, J.E., 2008. *CO2 Reactivity of Chars from Wheat, Spruce and Coal*, Blackwell Science Ltd. Available at: http://dx.doi.org/10.1002/9780470694954.ch4.

Ryu, C., Nasserzadeh, V. & Swithenbank, J., 2004. Gasification of wood char by ultra-superheated steam in an entrained flow reactor. *Journal of the Energy Institute*, 77(512), pp.46-52.

Senneca, O., 2007. Kinetics of pyrolysis, combustion and gasification of three biomass fuels. *Fuel Processing Technology*, 88(1), pp.87-97.

Shafizadeh, Fred & Chin, P., 1977. Thermal Deterioration of Wood. In *Wood Technology: Chemical Aspects*. ACS Symposium Series. AMERICAN CHEMICAL SOCIETY, pp. 57-81. Available at: http://dx.doi.org/10.1021/bk-1977-0043.ch005.

Sjöström, E., 1993. *Wood Chemistry: Fundamentals and Applications*, San Diego, California: Academic Press.

Svoboda, K. et al., 2009. Pretreatment and feeding of biomass for pressurized entrained flow gasification. *Fuel Processing Technology*, 90(5), pp.629-635.

Thurner, F. & Mann, U., 1981. Kinetic investigation of wood pyrolysis. *Industrial & Engineering Chemistry Process Design and Development*, 20(3), pp.482-488.

Tye, R., 1969. Thermal Conductivity. In *Thermal Conductivity*. London: Academic Press.

Varhegyi, G., Jakab, E. & Antal, M.J., 1994. Is the Broido-Shafizadeh Model for Cellulose Pyrolysis True? *Energy & Fuels*, 8(6), pp.1345-1352.

Vreugdenhil, B.J., 2009. Co gasification of biomass and lignite. Available at: http://www.ecn.nl/docs/library/report/2009/l09124.pdf.

Wagenaar, B.M., Prins, W. & van Swaaij, W.P.M., 1993. Flash pyrolysis kinetics of pine wood. *Fuel Processing Technology*, 36(1-3), pp.291-298.

Wee, H.L. et al., 2005. The effect of combustion conditions on mineral matter transformation and ash deposition in a utility boiler fired with a sub-bituminous coal. *Proceedings of the Combustion Institute*, 30(2), pp.2981-2989.

Wen, C., Lee, S. & Dutta, S., 1979. *Coal conversion technology*, Reading, Massachusetts: Addison-Wesley Publishing Co., Inc.

Westbrook, C.K. & Dryer, F.L., 1981. Simplified Reaction Mechanisms for the Oxidation of Hydrocarbon Fuels in Flames. *Combustion Science and Technology*, 27(1), pp.31 - 43.